Development of an Infrared Direct Viewer Based on a MEMS Focal Plane Array

A Thesis
submitted to the faculty of the

Worcester Polytechnic Institute

as a partial fulfillment of the requirements for the
Degree of Master of Science
in
Mechanical Engineering

By

Garth M. Blocher

27 June 2014

Approved:

Prof. Cosme Furlong, Advisor

Prof. John Sullivan, Member, Thesis Committee

Prof. Brian Savilonis, Member, Thesis Committee

Prof. Pilar Arroyo, University of Zaragoza, Spain, Member, Thesis Committee

Prof. Raghvendra Cowlagi, Graduate Committee Representative

Abstract

Thermal infrared (IR) imaging systems are widely used in medical, industrial, and defense applications. IR imaging systems utilize a lens to focus IR radiation onto a focal plane array (FPA) of IR detectors, which transduce the IR radiation from the scene into signals that can be further processed. In conventional IR imaging systems, electronic readout integrated circuitry (ROIC) is used to read out the information from the FPA, and computer signal processing allows for an IR image to be displayed on an electronic screen. However, the ROIC decreases the thermal isolation and sensitivity of the IR detectors in the FPA, and the computer processing and electronic display increase the cost, weight, and complexity of the IR imaging system. This thesis focuses on the development of an IR direct viewing system that does not require any ROIC, computer signal processing, or electronic display. This is accomplished through the use of microelectromechanical systems (MEMS) uncooled IR imaging detectors, which consist of arrays of bimaterial thermomechanical cantilever structures that tilt as a function of IR radiation from a scene. Other members of the WPI-ME/CHSLT group have previously shown that an interferometric optical readout mechanism based on digital holography and computer processing can eliminate the need for ROIC and be used to measure the nanometer scale tilt of the structures in a MEMS-based IR imaging system that was found to have a responsivity of 1.5 nm/K. However, these previously demonstrated results required significant computer processing and an electronic display. The hypothesis of the current work is that an optomechanical readout mechanism can be used to realize an IR direct viewer *without* the use of ROIC, computer signal processing, or an electronic display. Three optical readout mechanisms were

identified for transducing the nanometer scale deformations of the MEMS structures in the FPA into a directly observable visible light image. Two of these, one using live holography and the other using Nomarski differential interference contrast (DIC), were based on interferometry, while the third, using reflectometry, was based on geometrical optics. The identified optical readout mechanisms were analytically evaluated based on the performance and perception of the human vision system (HVS), and preliminary experimental results were obtained using optical setups constructed for all three readout mechanisms. Based on the analytical and experimental investigations, reflectometry was selected as the most suitable readout mechanism for a direct viewer. A visible light camera was used with custom software to determine a temperature sensitivity of 137 mK for the reflectometry readout, and thermal images of scenes at human body temperature were demonstrated using limited computer processing. A false color, direct view, live IR imaging system was then demonstrated based on a two color reflectometry readout and the output was characterized with respect to the color differentiation sensitivity of the HVS. The system temperature sensitivity, based on the theoretical color differentiation sensitivity of a human observer, was found to be on the order of 10 K across a measuring range of roughly 400 °C, and objects with a temperature as low as approximately 150 °C were distinguishable. The advantages and limitations of the developed IR imaging system are identified and recommendations for further developments and future work are provided.

Acknowledgements

I would like to thank my advisor Professor Cosme Furlong for giving me the opportunity to do this work and for the guidance he has provided along the way. Additionally, the project would never have progressed as far as it did without the help of all the members of the Center for Holographic Studies and Laser micro-Mechatronics. I would like to particularly thank both Ivo Dobrev and Morteza Khaleghi for their constant support and encouragement, Ellery Harrington for his software development that has proven invaluable for the success of this project, and Peter Hefti for his assistance with the optical systems. I would also like to thank Jack Salerno and Frank Pantuso of Agiltron Inc., in Woburn, MA for providing the MEMS arrays used for this work. Finally, special thanks to Prof. J. M. Sullivan & the James Nichols Heald Research Award to the CHSLT and to the ME Department for their support.

Table of Contents

List of Figures

List of Tables

Nomenclature

Au	Gold
C	Spectral light
CIE	Commission Internationale de l'Eclairage
CIE76, ΔE^*_{ab}, de76, ΔE*	CIELAB color difference based on 1976 formulas
CIE94, de94	Color difference based on CIE formulas from 1994
CIEDE2000, de00	Color difference based on CIE formulas from 2000
CIELAB	Color space based on the CIE L*, a*, b* components
CMC(l:c)	Color measurement committee color difference
CMF	Color Matching Function
c_o	Speed of light in a vacuum
c_r, c_g, c_b	Amount of red, green, and blue primaries, respectively
d	Deflection of cantilever element
$\boldsymbol{D}$	Displacement vector
da	Surface area from which radiation is emitted
d_i	Excursion of reflected light
D_x, D_y, D_z	Magnitudes of displacement
dΩ	Solid Angle
f	Focal length of lens
FPA	Focal Plane Array
h	Universal Planck constant

HVAC	Heating Ventilation and Air Conditioning
HVS	Human Vision System
I	Light intensity
$I(T,\lambda)$	Light intensity as a function of temperature and wavelength
$\boldsymbol{i}, \boldsymbol{j}, \boldsymbol{k}$	Unit vectors
I_o	Intensity of object wave
IR	Infrared
I_r	Intensity of reference wave
$\boldsymbol{K}$	Sensitivity vector
$\boldsymbol{K_1}$	Illumination vector
$\boldsymbol{K_2}$	Observation vector
K	Universal Boltzmann constant
K	Wavenumber
k_o	Constant
k_λ	Photometric constant
L	Length of MEMS element
L^*, a^*, b^*	Components of CIELAB color space
L_1	Distance from lens to beam splitter
L_2	Distance from MEMS array to beam splitter
L_3	Distance from MEMS array to filter plane
L_e	Radiance

LMS	Long-, middle-, and short-wavelength-sensitive
L_v	Measured luminance
L_λ	Light transmittance
M	Color space transformation matrix
M	Ratio of material thicknesses
MEMS	Microelectromechanical Systems
N	Number of greyscale levels
m_1, m_2	Refractive indices of transmissive mediums
N	Ratio of moduli of elasticity
NEDT	Noise Equivalent Differential Temperature
Nomarski DIC	Nomarski Differential Interference Contrast
$f(\lambda)$	Receptor sensitivity as a function of wavelength
$P(\lambda)$	Spectral power distribution as a function of wavelength
ROIC	Readout Integrated Circuitry
RGB	RGB color space
$\bar{r}, \bar{g}, \bar{b}$	r, g, and b components of a color matching function
S	Perceived brightness
s	Shear distance
$S(\lambda)$	Relative spectral power distribution
S_1	Distance from lens to object
S_2	Distance from lens to image plane
SiNx	Silicon nitride

SPD	Spectral Power Distribution
sRGB	Standard RGB color space
T	Temperature
t	Thickness of bimaterial strip
U_h	Holographically reconstructed wavefront
U_o	Wavefront of light reflected from an object
U_r	Reference light wavefront
V	Signal output
X, Y, Z	CIE XYZ primaries
X_n, Y_n, Z_n	Primary components of reference white
x, y, z	Relative CIEXYZ primaries
$\bar{x}, \bar{y}, \bar{z}$	x, y, and z components of a color matching function
α	Apex angle
α_1, α_1	Coefficients of thermal expansion
β	Prism optical axis angle
γ	Gamma correction value
Γ	Path difference
Δd_f	Half width of zero-order spectra
Δd	Half width of focused light spot
ε	Shear angle
θ	Angle
θ_1	Angle of incidence

θ_2	Angle of refraction
θ_{max}	Angular measurement range
θ_{min}	Angular resolution
Λ	Wavelength of radiation
P	Radius of curvature
T	Angle between polarizer and closest privileged direction
Φ	Radiant Flux
$\phi(T,\lambda)$	Relative spectral color stimulus function
ϕ_F	Diameter of illumination at the filter plane
ϕ_{FPA}	Diameter of illumination at the FPA
ϕ_o	Phase of object wave
ϕ_r	Phase of reference wave
φ	Angle between polarizer and analyzer
Ω	Fringe locus

Objective

The goal of the current work is to investigate the use of a purely optomechanical readout mechanism for a thermomechanical MEMS infrared detector array in order to create an infrared direct viewer without the use of electronic readout circuitry, computer signal processing, or an electronic display. Specific objectives are as follows:

1. A human eye or standard visible light camera should easily detect changes in readout output corresponding to changes in the temperature of a scene.

2. The readout mechanism should require no power other than for illuminating light.

3. The system should not require computer processing to display a thermal image.

4. The readout should operate in real time.

5. The readout must be compatible with the currently available MEMS infrared detector.

1. Introduction

All physical matter with a temperature above absolute zero emits infrared (IR) radiation as a function of its temperature. IR imaging refers to methods of capturing the IR radiation emitted from a scene, similarly to how regular cameras use visible light to capture an image of a scene. This allows for imaging without the need for an external source of illumination as well as for full-field, non-contact temperature measurements. This has led to many and wide ranging applications for IR imaging including night vision, military imaging, security, medical diagnosis, and astronomy [**1**]. Representative IR images similar to those used for specific applications are shown in Figure 1-1.

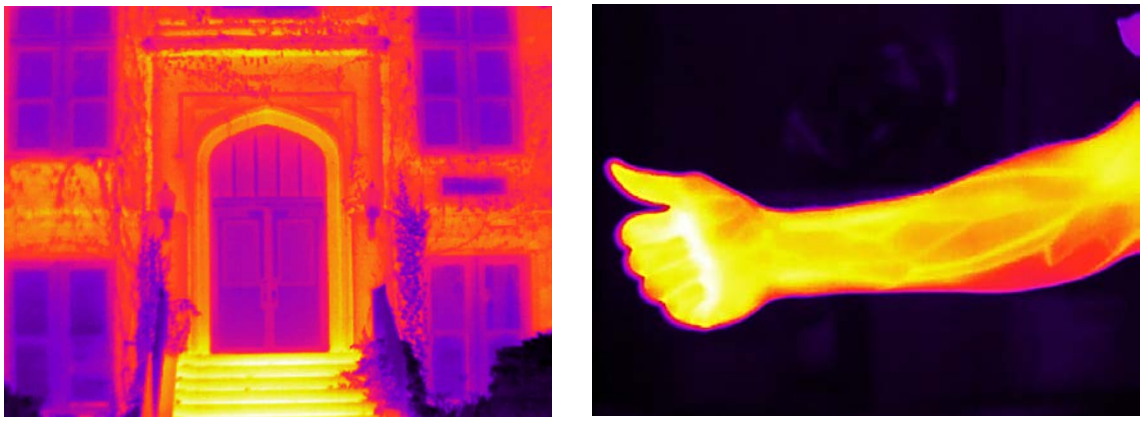

Figure 1-1. Representative thermal images similar to those used for the investigation of heat transfer in buildings and for medical diagnosis. The temperature difference between the door and surrounding areas of the building are visible in the first image and the vascularity of the forearm is visible against the slightly cooler surrounding tissue in the second image.

IR imaging systems generally include a lens to focus radiation from a scene, a focal plane array (FPA) of IR detectors onto which the IR is focused, a readout to extract information

from the FPA, signal processing to convert the information into a presentable form, and finally an electronic display to present a thermal image to a human observer. Many FPAs convert infrared radiation into an electrical quantity that is read out and displayed using an electronic readout mechanism and computer based signal processing. An infrared direct viewer uses an IR lens to focus radiation onto a FPA that, combined with a purely optomechanical readout mechanism and without the use of any electronics in the FPA, readout, signal processing, or display, transduces the IR directly into a stimulus that is perceivable by the naked human eye. The stages of both an electronic IR imaging system and an IR direct viewer are shown in Figure 1-2.

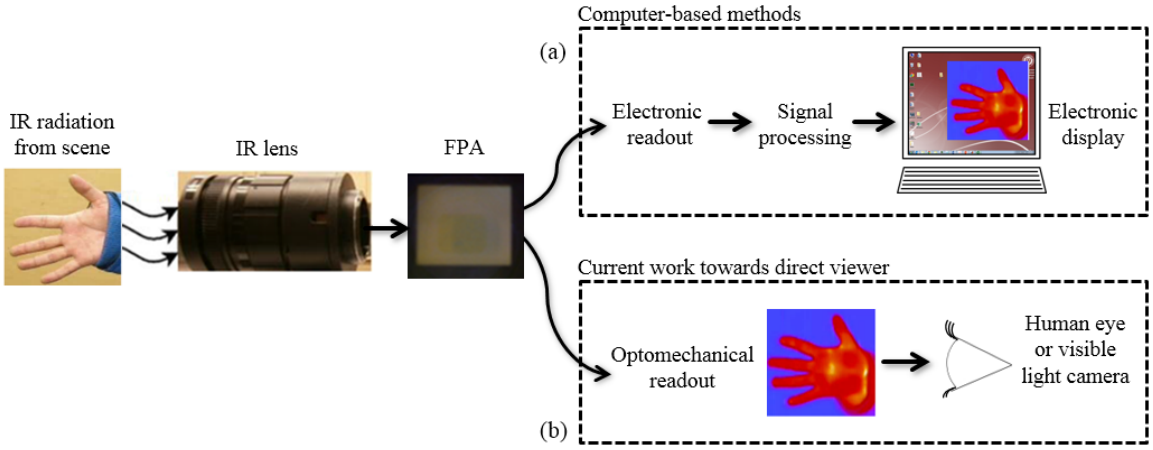

Figure 1-2. Stages of an infrared imaging system: (a) Electronic readout and computer based signal processing in a standard IR imaging system and (b) a direct viewer which produces a visible light signal directly from an optomechanical readout, without any readout integrated circuitry, computer signal processing, or electronic display.

There currently exist FPAs based on microelectromechanical systems (MEMS) that contain bi-material structures which deflect as a function of temperature [**2-4**], and a direct view IR imaging system could be realized if an optical readout could be used to

transduce the deformation of the elements of the FPA directly into visible light images. Several groups have investigated the use of bi-material FPAs in attempts to create IR direct viewers with readout mechanisms based on a variety of optical techniques including deformable diffraction gratings [**5**], holographic compensation of the illuminating light [**6**], and filtering the Fourier spectra of the FPA [**7-8**]. However, published results have often used computer processing to increase system sensitivity and no false color IR direct view systems have been reported. This research investigates the human perceptual response to readouts based on three different mechanisms: holography, Nomarski differential interference contrast (DIC), and reflectometry. This is accomplished through the use of analytical perceptual color modeling and color difference calculations based on the theoretical performance of the human visual system. Based on analytical evaluations and preliminary experimental results for each readout mechanism identified, a reflectometry based readout is determined to be the most suitable mechanism for an infrared direct viewer. A false color direct view IR imaging system based on an FPA of bi-material MEMS cantilevers and a two color reflectometry readout is realized. A color sensitive visible light camera is used to measure the output from the readout, and the performance of the constructed system is analyzed with respect to the color discrimination sensitivity of the human vision system (HVS). Representative thermal images obtained using the developed system are presented, and recommendations for further development and future work are provided.

2. Background

2.1. Radiation

Maxwell's equations combine the work of many other pioneering scientists, including Gauss's laws for electric and magnetic fields, Ampere's law regarding the relationship between magnetic fields and electric current, and Faraday's law for the induction of electric voltage due to changes in a magnetic field. Maxwell determined that electric and magnetic fields are intrinsically related, and that a change in one will affect a change in the other. This coupling of fields can case a cyclical response similar to that of a mechanical wave; electromagnetic waves exhibit an amplitude, wavelength, and frequency. Similarly to mechanical waves such as sound, electromagnetic waves radiate away from a source; however, electromagnetic waves can travel through empty space as well as through many gasses, liquids, and some solids. This is called electromagnetic radiation. It is sometimes also useful to describe electromagnetic waves a particles or packets of energy that are known as photons or quanta [**9**]. Electromagnetic waves can exist with a large range of wavelengths; the most noticeable are those in visible range with wavelengths from just under 400 nm to just beyond 700 nm as shown in Figure 2-1.

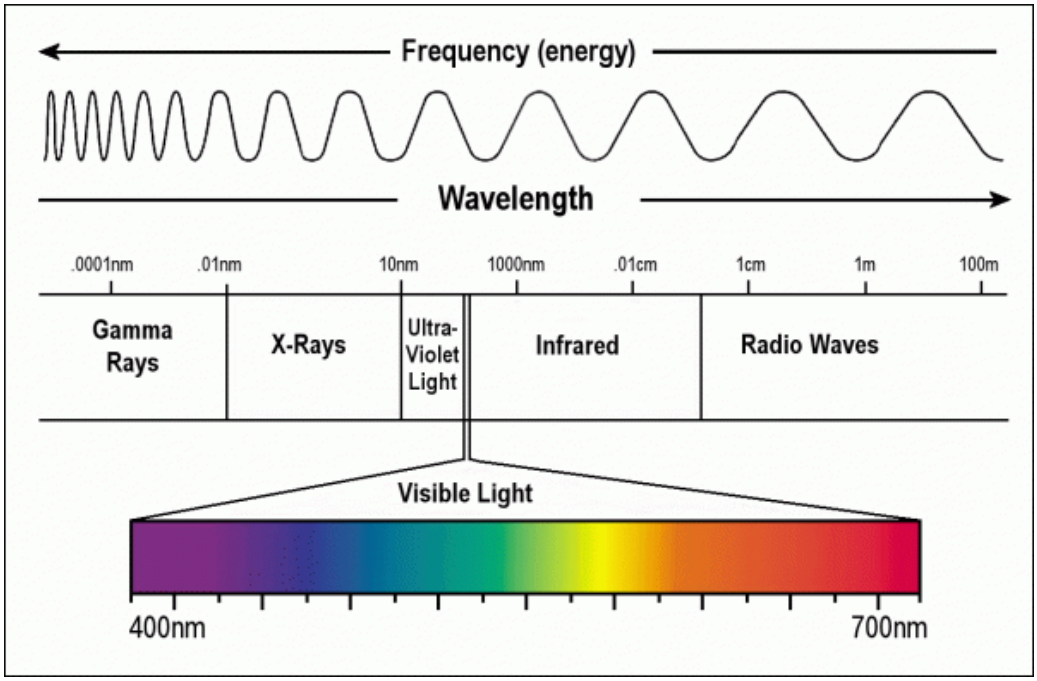

Figure 2-1. Representative electromagnetic spectrum, including a highlight of the visible range[**10**].

The human eye has highly developed systems that are sensitive to certain wavelengths of radiation which have been classified as the visible spectrum. While the wavelengths in this spectrum do not have a color *per se*, the shorter wavelengths produce the perception of the color blue, while the longer wavelengths produce the experience of the color red; the perception of color is a psychological phenomenon somewhat removed from the physical properties of the light from which it arises [**11**].

All matter with a temperature greater than absolute zero will emit electromagnetic radiation due to collisions of the particles that make up that matter. The energy released during these collisions is related to the temperature of the matter, and determines the

energy and wavelength of the radiation that is released. From the second law of thermodynamics, matter that is warmer than its surroundings will release energy to its environment, while matter that is cooler than its surroundings will absorb energy, until thermal equilibrium is eventually reached. Radiation is emitted and absorbed from all directions, suggesting the use of spherical coordinate systems for analysis. As the distance from a radiating object increases, the spatial density of the radiation is inversely proportional to the surface area of a sphere with the radius equal to the distance from the object to the point of observation. The leads to the use of the steradian (sr) as a unit to describe the solid angle defined as the ratio of the subtended area on the surface of a sphere and the square of the distance from the vertex (the radius of the sphere). On the surface of a sphere, the subtended angle will be one steradian for an area equal to the square of the radius. The radiant flux, Φ, is used to describe the total amount of energy radiated from a body per unit time, and is equivalent to power. Radiance, L_{e}, is then given as the amount of energy radiated from a surface area into a unit solid angle. This is given by

$$L_{\mathrm{e}} = \frac{\Phi}{\mathrm{d}a\mathrm{d}\Omega}, \tag{2-1}$$

where $\mathrm{d}a$ is the surface area and $\mathrm{d}\Omega$ is the solid angle into which radiation is emitted [**12**]. Emissivity is used to describe a surface's relative ability to emit radiation. Emissivity can range from 0, for a surface that emits no radiation, to 1 for a surface that is completely emissive. A blackbody is a theoretical material which has an emissivity of 1

that can be used as a comparison to make relative measurements of other surfaces. A blackbody is defined as a diffuse emitter with the characteristic that it absorbs all incident radiation and emits radiation according to its temperature [**13**].

Given that all objects emit radiation, infrared temperature measurements can be accomplished if the relationship between radiation and temperature is known. This relationship is given by Plank's law of Blackbody Radiation where radiance can be determined as a function of wavelength, λ, and temperature, T, as

$$L_{\mathrm{e}}(\lambda, T) = \frac{2hc_o^2}{\lambda^5 \left[\exp\left(\frac{hc_o}{\lambda kT}\right) - 1\right]}, \tag{2-2}$$

where h is the universal Planck constant ($6.62606957 \times 10^{-34}$ m^2 kg / s), k is the universal Boltzmann constant ($1.3806488 \times 10^{-23}$ m^2 kg s^{-2} K^{-1}), and c_o is the speed of light in a vacuum (299,792,458 m / s) [**13**]. Examination of this equation reveals that the amount of radiation varies continuously with wavelength and increases with temperature as shown in Figure 2-2.

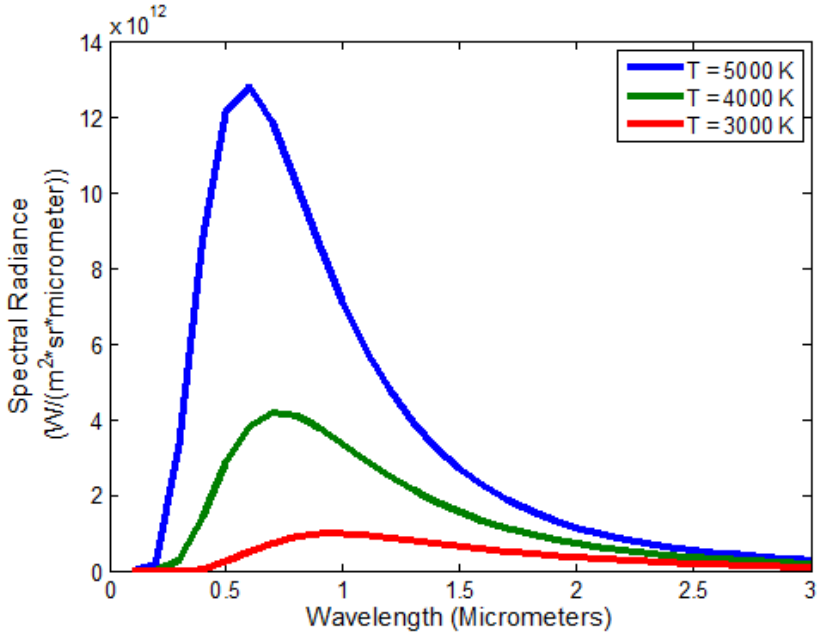

Figure 2-2. Plot of Plank's Law of Blackbody Radiation[**14**].

Infrared imaging systems can take advantage of this behavior to make accurate temperature measurements by measuring the relative amounts of radiation emitted from objects in a scene. From Plank's law follows Wein's displacement law which given by

$$\lambda_{\text{peak}} T = 2.898 \times 10^{-3}\ m\ K, \tag{2-3}$$

which shows that peak radiance will occur at shorter wavelengths for higher temperatures. The range of sensitivity for any infrared imaging system used for temperature measurements must therefore be matched to the emission spectrum at the temperature range of interest; some IR sensing technologies may not be suitable for measurements across the entire IR spectrum.

2.2. Lenses for Infrared and Visible Radiation

Both visible light and infrared systems often make use of lenses in order to focus radiation from a scene onto a focal plane array. Optical systems have a number of parameters that define their performance and capabilities. The focal length of a lens defines how strongly it can affects the direction of a ray of light, and the relationship between the location of the lens and the focal plane array and the distance from the lens at which objects will be in focus. The field of view is the scene that is visible at any time, and the minimum and maximum working distances define the closest and farthest, respectively, distances from the lens at which an object may be in focus. The depth of field defines the range of distances at which objects will be in focus. The ratio of the focal length of a lens to its aperture is known as the *f*-number and gives a metric for the amount of radiation that will be focused by the lens [**15**].

All transmissive materials have an index of refraction. When rays of light travel across a boundary between two indices of refraction the light will be refracted and leave the boundary at an angle different from when it arrived. The specific materials used are determined by wavelengths of radiation that the lens will be used to focus. Many types of glass can be used to effectively focus radiation in the visible light wavelengths. However, materials that work well with visible light are often incompatible with IR radiation; they do not have sufficiently high transmissivity in the IR range to allow the construction of efficient IR lenses. Conversely, some materials efficiently transmit IR radiation while absorbing or reflecting light in the visible range. These materials can be

used to provide spectral filtering of radiation from a scene, and to focus the transmitted IR radiation onto a FPA of infrared detectors. Dielectric coatings, comprised of alternating layers of material with low and high refractive indices, can also be designed to provide specific levels of transmission, absorption, and/or reflection across a particular range of radiation wavelengths. Dielectric stacks can be applied to the surface of optical elements and can be designed to filter the transmitted spectra or to decrease unwanted reflections in order to provide an antireflection coating and increase the transmission efficiency of the optical element. IR lenses are often constructed from specially coated germanium due to its opaqueness across the visible spectrum and transmission efficiency for radiation in the IR range from 2000 nm to beyond 12000 nm [**1**]. The transmittance curves for several materials, including germanium, used in IR systems are shown as a function of wavelength in Figure 2-3

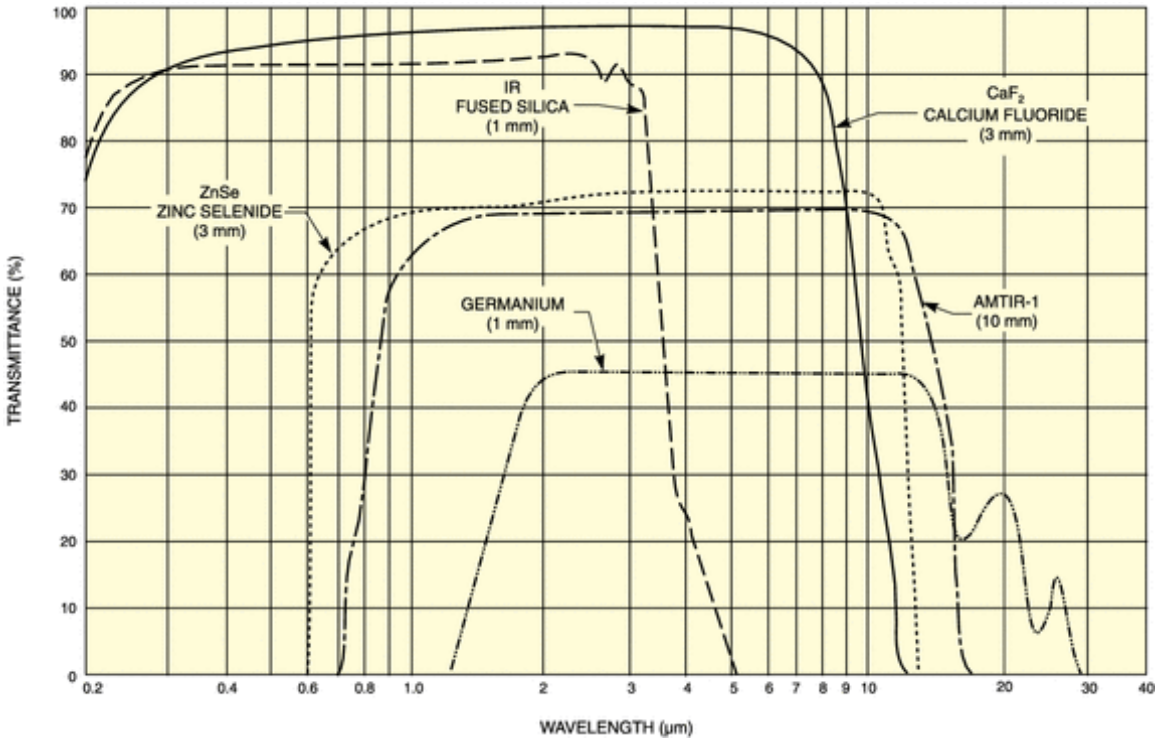

Figure 2-3. Transmittance of several IR optical materials[**16**]. Germanium is a commonly used material for lenses in infrared imaging systems due to its opaqueness in the visible range and transmittance in the range 2000 nm to beyond 12000 nm.

2.3. Infrared Imaging Technologies

Similarly to how a visible light camera has a specified number of pixels in the image it records, IR imaging systems use FPAs made up of many individual IR detectors in order to create an infrared image. In general, most infrared imaging technologies can be separated into two main categories; based on either photon detectors or thermal detectors. Photon detectors measure interactions between photons emitted from a scene and electrons in the material of a detector. Detectors in this category can offer excellent sensing performance, and a quick response time, but require cryogenic cooling in order to

do so [**17**]. Such cooling is often not only mechanically complicated, but can also be very expensive. In contrast, thermal detectors absorb radiation from a scene and experience a change in temperature which is then measured through the sensing of some related material property such as a voltage, resistance, or shape. One of the most common examples of this is a bolometer type sensing device which measures the temperature dependent resistance of a sensing element [**17**]. Modern bolometers offer a wide range of sensing and performance, many without the need for expensive and complicated cryogenic cooling [**17**]. However, bolometers and similar thermal sensor require individual pixel addressing and electrical pathways for the sensing of each pixel in the array. This creates requirements for highly complex readout integrated circuitry (ROIC) in the focal plane array itself, and also provides conductive pathways that reduce the thermal isolation of the sensing structures, leading to reduced sensitivity [**17**]. The signal from photonic and bolometer style infrared detectors must be read out electrically, and this information can be processed and then presented to a human observed by means of an electronic display such as an LCD screen.

2.4. Thermomechanical Infrared Detectors

Another type of thermal detectors are thermomechanical detectors that transduce a change in temperature into a mechanical displacement. One of the earliest examples of this behavior is in the Golay cell which uses the expansion of heated gas to cause a mirrored membrane to deform [**18**]. This deformation can then be measured using optical methods. More recently, MEMS technologies have allowed the creation of micro-scale

bi-material structures that exhibit temperature dependent deformation due to mismatched coefficients of thermal expansion, behavior similar to that of the macro-scale bimaterial springs commonly used in heating, ventilation, and air conditioning (HVAC) thermostats. Many such MEMS designs have been proposed, and several realized, including arrays of micro-cantilevers that experience a nanometer scale changes in orientation and/or shape when exposed to infrared radiation from a scene [**2-4**]. The temperature dependent change in the radius of curvature of each bi-metallic structure can be predicted using the equations developed by Timoshenko [**19**] for the behavior of bi-metallic thermostats. The radius of curvature, ρ, of a beam can be found from

$$\rho = \frac{t\{3(1+m)^2 + (1+mn)[m^2 + (1/mn_E)]\}}{6(\alpha_1 - \alpha_2)(\Delta T)(1+m)^2}, \tag{2-4}$$

where t is the combined thickness of the bonded strip, m is the ratio of thickness of the low- and high- thermal expansion materials of the beam, n is the ratio of their moduli of elasticity, α_1 and α_2 are the coefficients of thermal expansion for the low- and high-expansion materials, respectively, and ΔT is the change in temperature from initial conditions. The deflection, d, at the tip of a cantilever can be determined using

$$d = \rho[1 - \cos(\theta)], \tag{2-5}$$

and the angle θ can be determined by

$$\theta = L/\rho, \tag{2-6}$$

where L is the length of the beam and θ is the included angle of the cantilever, as shown in Figure 2-4.

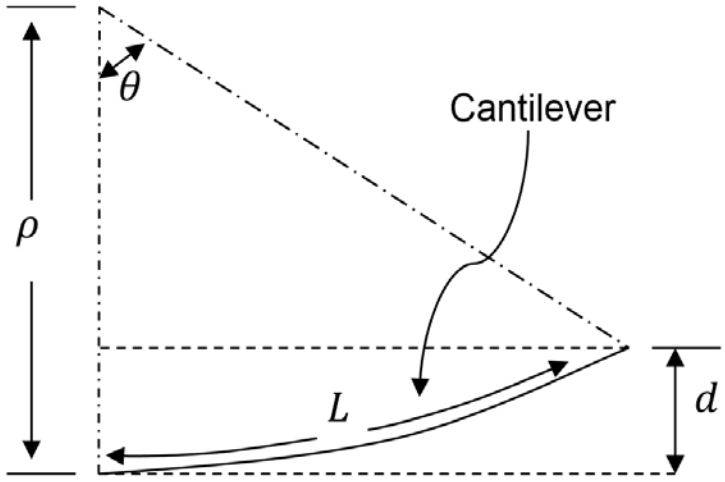

Figure 2-4. Thermomechanical deflections in bimaterial cantilevers.

An example of a MEMS bimaterial thermomechanical infrared detector is shown in Figure 2-5 which has been adapted from [**20**] shows a thermomechanical MEMS structure where visible light from above is reflected off a metallic surface while infrared radiation from below is absorbed by a dielectric material.

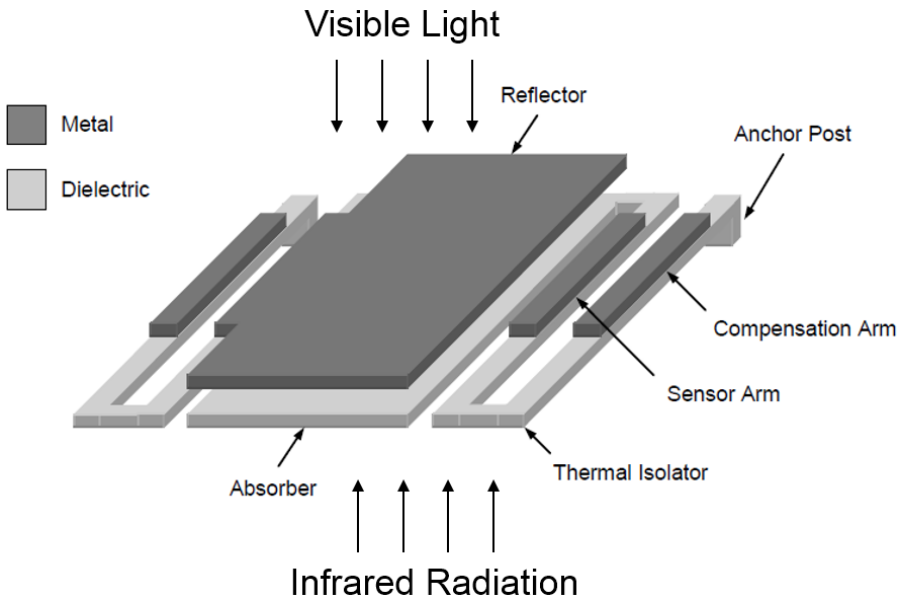

Figure 2-5. MEMS thermomechanical infrared detector [**20**].

The structure shown in Figure 2-5 includes compensation arms that conduct heat from the substrate that the structure is mounted on. This maintains the temperature of the compensation arms at roughly the same temperature as the substrate, and the deformation of these arms can be used to compensate for ambient temperature changes. Microcantilever MEMS devices often use silicon nitride (SiN_x) as an infrared absorber and gold (Au) as the reflective surface. The relevant properties for these materials are listed in Table 2-1.

Table 2-1. Physical properties of materials used in MEMS bimaterial structures

Materials	Young's modulus, E (GPa)	Coefficient of thermal conductivity, k (W/m K)	Coefficient of thermal expansion, α (10^{-6} K^{-1})	Emissivity, ε
SiNx	180	5.5	0.8	0.8
Au	73	296	14.2	0.01

Due to its very low coefficient of thermal conductivity, silicon nitride is also used as a thermal isolator in the support legs of the sensing structures. This reduces the transmission of substrate temperature variations to the bimaterial structures of the array. The significantly different coefficients of thermal expansion allow for pronounced temperature dependent deformation.

Of particular interest is the use of optical readout methods in order to image an entire array of microstructures without the need for complex ROIC or individual pixel addressing. Figure 2-6 shows a representative focal plane array of MEMs thermomechanical infrared detectors, where infrared radiation enters from the left and causes a change in curvature, and nanometer scale deformation, of the bimaterial cantilever elements of the array.

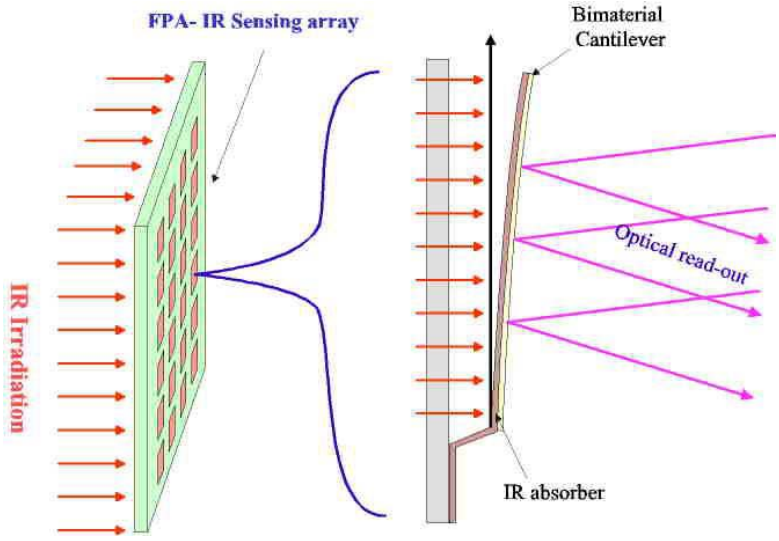

Figure 2-6. Representative thermomechanical MEMs infrared imager comprised of an array of bimaterial structures that exhibit nanometer scale deformations as a result of interaction with IR radiation from a scene [**21**].

2.5. Optical Readouts for Thermomechanical IR Detectors

Several groups have pursued such approaches and obtained noteworthy results including thermal imaging at up to 1000 frames per second when using computer post processing [**21-23**]. This has been achieved with computer processing of intensity based optical readout mechanisms where a reference image is subtracted from subsequent images in order to increase the overall image quality and to reduce the effects of initial non-uniformity in the FPA caused to the manufacturing process used. Additional processing has been used to reduce apparent dead space between active sensing elements in a FPA and further improve the quality of the image appearance. Representative images produced using reference subtraction and image post processing are shown in Figure 2-7.

Figure 2-7. Representative thermal images obtained using reference subtraction and computer post processing of data from a MEMS thermomechanical IR detector [**21**].

2.6. Direct View IR Imaging

The possibility of creating an infrared direct viewer has been the subject of much recent interest. Such a system would project a visible image of the thermal radiation from a scene directly into the eye of an observer, without the use of any computer processing or electronic display. To this end, several optical readout methods have been investigated to achieve such a system, including deformable diffraction gratings driven by bi-material MEMS structures and holographic compensation of the illuminating light in order to increase the sensitivity of the system and compensate for non-uniformity of the focal plane array. Neither of these readout approaches achieved performance suitable for a direct view system [**5**] [**6**]. Another, more promising approach is the use of an optical system based on the filtering of light at the Fourier plane of a lens. This approach has been successfully used with an advanced, deformation magnifying substrate-free, microcantilever FPA to project visible light images of an infrared scene directly onto the CCD of a visible light camera. A schematic of the setup used for this is shown Figure 2-8.

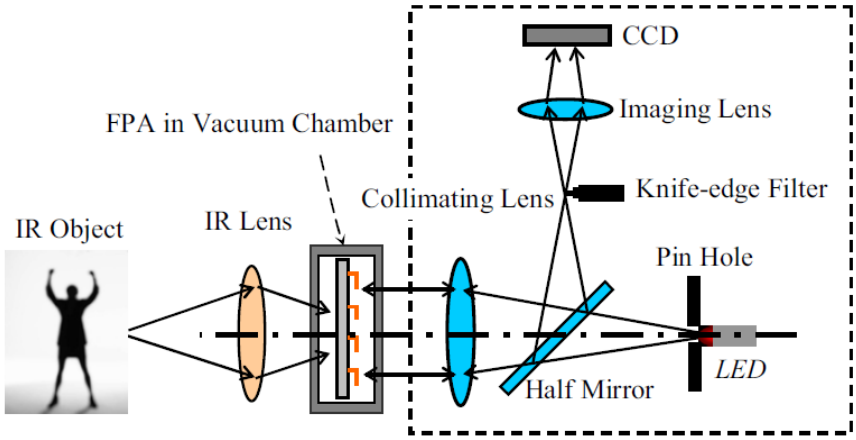

Figure 2-8. Schematic diagram of IR imaging system based on spectra filtering at the Fourier plane [**7**].

It was reported that the optical readout mechanism achieved a resolution of 10^{-5}° for measuring the change in tilt of the microcantilever structures. Room temperature images were detectable using a visible light camera and computer processing to subtract a reference image (of the FPA in a relaxed state) from subsequent frames. Subtraction of a reference image allowed for low temperature scenes to be imaged. This is the smallest published measurement resolution for an optical readout used for imaging a thermomechanical IR detector array. Representative images of the published results are shown in Figure 2-9.

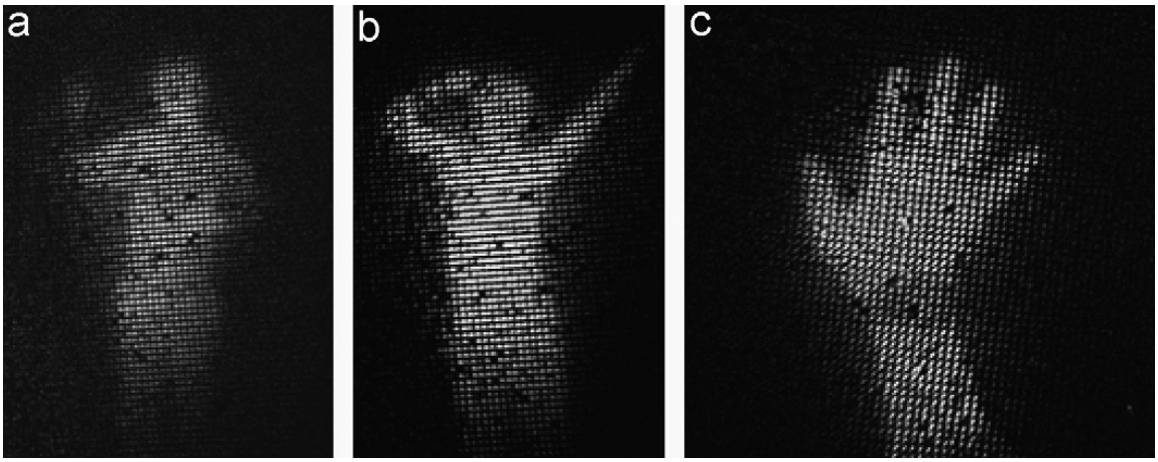

Figure 2-9. Representative infrared images using filtering of the Fourier spectra as reported by [**7**]: (a) a man wearing a coat; (b) a man removing a coat; and (c) a hand and wrist with watch outline visible.

The published work on optical readouts for infrared imaging using thermomechanical IR detectors focuses on the applications of such systems to be used with visible light cameras. In this case, changes in brightness can be easily quantified and presented to a human observer through the use of an electronic display. However, no published work has investigated the performance of a direct view system with consideration for the human eye and visual system. This can be accomplished through the use of perceptual color modeling and color difference calculations based on the response of the human visual system.

Here the implications of human visual perception are considered for several readout mechanisms, and theoretical system temperature sensitivity for a direct human observer is determined. The current work investigates several not previously considered optical readout methods for creating an infrared direct viewer, including phase compensation through live holographic interferometry, false color IR imaging based on Nomarski DIC,

and false color IR imaging using reflectometry based on image-plane filtering of reflected light. The identified readout mechanisms are evaluated based on the color differentiation sensitivity of the HVS and reflectometry is determined to be the most suitable for the realization of a direct viewer. A direct view system is demonstrated based on a reflectometry readout, and the output is characterized based on human perception.

3. Specific MEMS Based Focal Plane Array

The MEMS device utilized in this work, developed by Agiltron Inc., Woburn, MA, is vacuum packaged with a viewable area of approximately 15mm by 13mm and is shown in Figure 3-1. The FPA consists of 540 by 460 sensing structures, for a total of 248,400 elements, each with a reflective area having dimensions of approximately 45μm by 20μm [**20**] [**14**].

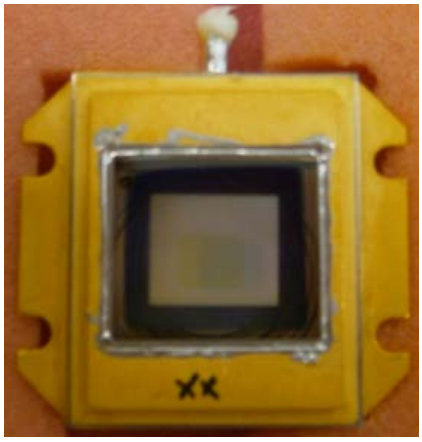

Figure 3-1. Currently used MEMS device. The device consists of a vacuum packaged FPA of thermomechanical IR detectors. Each IR detector consists of a micro mirror supported by bimaterial elements that deflect as a function of temperature changes caused by IR radiation from a scene [**14**] [**20**].

The proportion of the viewable area which is made up of active surfaces, in this case those which deflect measurably with temperature, is known as the fill factor. The current MEMS design, shown in Figure 3-2, has supporting arms, in addition to the anchor posts which hold each structure to the substrate, visible on either side of each reflective element, leading to a reduction in the fill factor of the device.

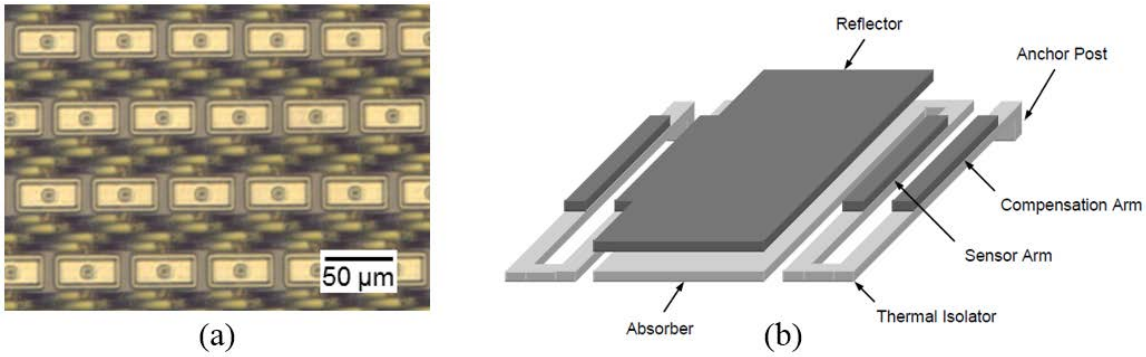

Figure 3-2. (a) A subsection of the array shown in Figure 3-1 and (b) an individual thermomechanical structure [**20**], including the supporting arms and anchor posts that occupy the space between the rows of reflector elements.

The arrangement of the support structures for each cantilever element in the current device leads to a fill factor of less than 50%, with significant "dead" space between each row of sensing elements and small gaps between each sensing element along a row.

The MEMS array has been characterized previously using advanced live digital holographic techniques [**14**]. A Linnik interferometer was used in conjunction with a piezo-driven phase stepping reference mirror in order to achieve accurate, full-frame measurements of the displacement of cantilever structures on a subsection of the FPA. Custom software was developed in order to automatically mask the active areas of the FPA and continuously solve the resulting system of stepped optical phase equations in order to display a modulation image in near-real time. False-color infrared images were presented on an electronic display; representative images obtained using this approach are shown in Figure 3-3.

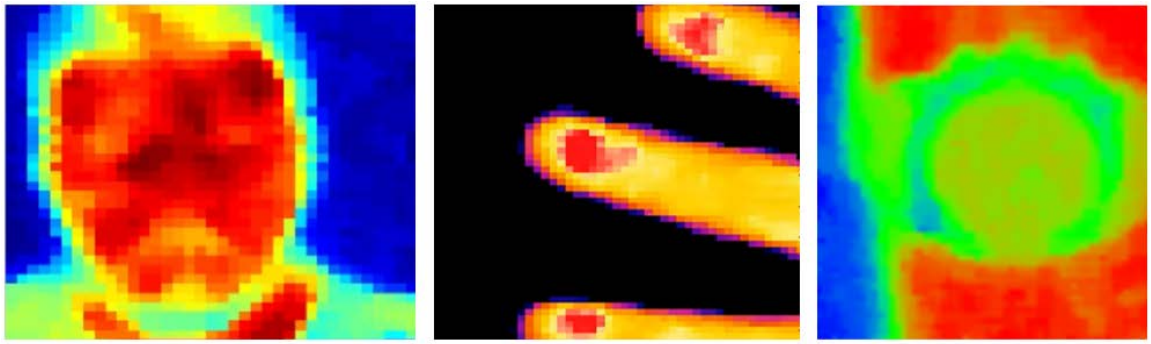

Figure 3-3. Infrared images previously obtained by the WPI-ME/CHSLT group through the use of live digital holography and computer data processing: (a) image of the temperature distribution on a face; (b) thermal image of fingers and fingernails; and (c) thermal image of arm with wristwatch [**14**].

The phase stepping method provides quantitative measurements of the displacement of the structures of the array, and this array was characterized to have a physical responsivity of approximately 1.5nm per Kelvin change in temperature of a scene. It was shown that a linear fit could achieve a correlation of 0.97 for the optical phase across individual elements of the array; the reflective surfaces behaved as tilting flat paddles while the sensing arms of the structure exhibited cantilever bending. The total number of imaged cantilever elements was limited by the magnification required to enable accurate phase stepping measurements, with most trials conducted using a 4x magnification of the FPA along with a camera of 1000 × 1000 resolution and 7.4μm pitch. This resulted in a viewable area of roughly 40 × 40 cantilever elements. A blackbody calibration source was used to measure a total system NEDT of 220mK [**14**].

4. Human Vision Considerations

To achieve a direct viewer system using purely optomechanical methods and without the use of any computer processing, the readout system must produce a stimulus that is easily detected by the human vision system (HVS). Humans possess highly developed mechanisms for the detection and processing of light stimulus with certain characteristics. Therefore, the direct view system that is developed must be designed appropriately. The HVS detects two aspects of light: the rate at which photons are detected and the relative amounts of light detected by cells sensitive in different wavelength ranges. The brain and visual system then process these data and present it as the perception of brightness and color, respectively. Detection occurs using a combination of four structures in the eye. Rods are primarily used for low rate photon detection in low light situations while three different cone structures are less easily saturated and allow for vision in brighter, higher rate, environments. The structure and components of the human eye and light sensing apparatus is shown in Figure 4-1, where it can be observed that light enters the eye through the cornea and lens before traveling to the back of the eye where some light passes through the retina to the photoreceptor cells.

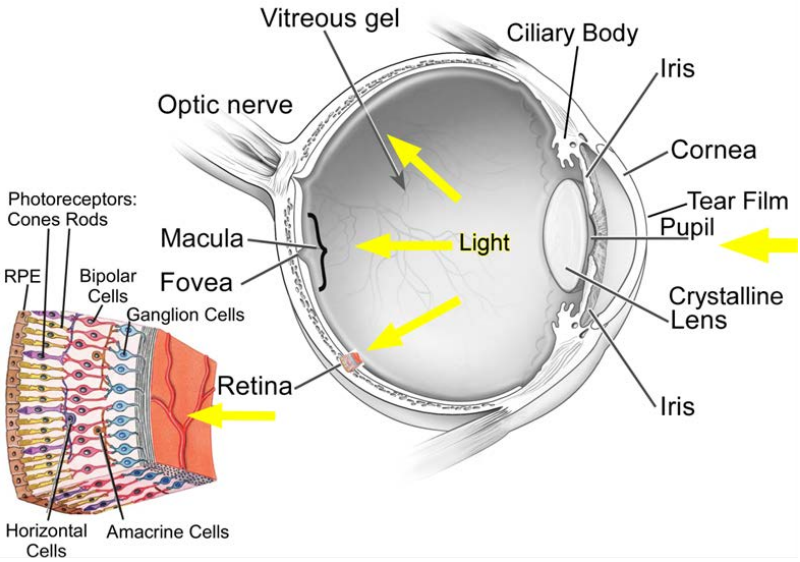

Figure 4-1. Structure and components of the human eye and light sensing apparatus [**24**].

When a photon, or quanta, of light is incident on the sensing structures of the eye, it can be absorbed by opsin pigment proteins in the rods or cones. Rods contain rhodopsin while each of the three types of cones contain one of three different opsin molecules [**25**]. The four types of opsin are sensitive to different wavelengths of light, with rhodopsin having the highest probability of absorption for light at 498nm while the three types of cone opsin have probability peaks at 420nm, 534nm, and 564nm respectively. A plot of the normalized sensitivity curves for the four sensing structures in the human eye is shown in Figure 4-2 [**26**].

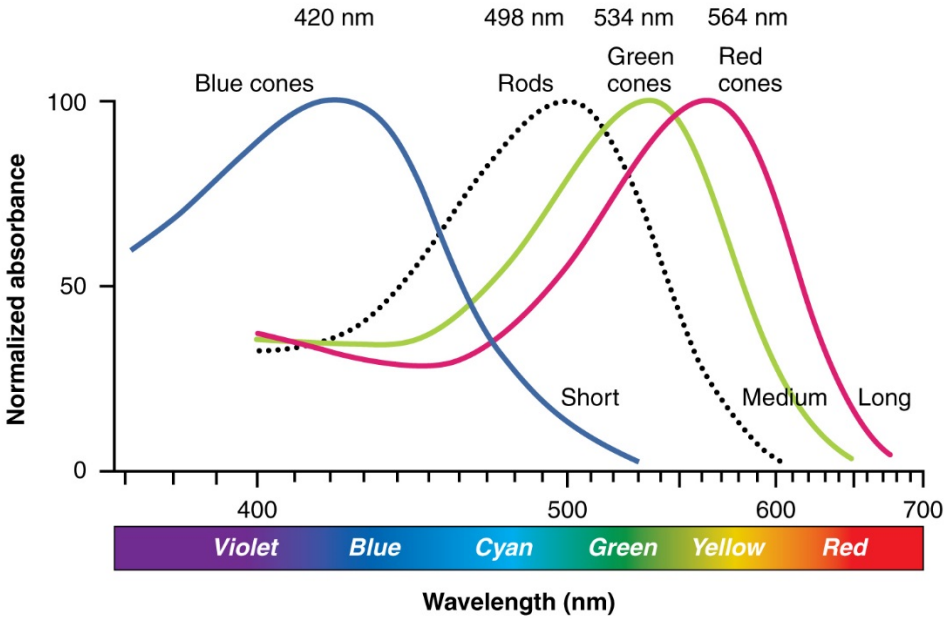

Figure 4-2. Normalized sensitivity curves of the four opsins present in the photoreceptors of the human eye [**26**]. The "blue" cones are sensitive to shorter wavelengths of light, which are perceived as blue, while the "green" cones are sensitive to wavelengths near the middle of the visual range that are perceived as green and the "red" cones are sensitive to the longest wavelengths in the visual spectrum, which are perceived as red. The rods as more sensitive, but more easily saturated, than the cones, and are used in low light conditions. Because there is only one type of rod, color differentiation is not possible in the low light situations where rods are most often used.

Wavelength discrimination, the mechanism of color vision, is achieved through comparison of the signals from the different types of receptors [**25**] [**27**]. The relationship between stimulus and human perception is quite intricate, but key figures of merit for the current work are the ability to distinguish changes in brightness, the ability to discriminate between changes in perceived color, and the ability to resolve information presented at given spatial frequencies. It has been shown that the perception of changes in brightness is strongly related to the original brightness, and that across the region of moderate illumination the just noticeable difference is very close to a constant percent

change in brightness, regardless of the original conditions. This is known as contrast constancy. Steven's Law relates the change in the perception, *S*, to the intensity of a stimulus, *I*, is [**28**]

$$S = k_0(I - I_{\text{th}})^b, \tag{4-1}$$

where I_{th} is a threshold stimulus value. For perceived brightness, the exponent *b* has been found to vary from approximately 0.33 for a dark adapted eye, up to about 0.44 for a bright adapted eye. The constant, k_0, depends on the units chosen for intensity and sensation, commonly candela per square meter. However, it has been found that this equation may not be valid for complex scenes. More complex relationships have been proposed, based on data from test photographs instead of color patches [**29**].

In general, the just noticeable difference in brightness will vary between individuals, and depends on the illumination wavelength, but has been found to be on the order of approximately 8% of the original intensity for low to moderate levels of adaptation and as small as roughly 1% for brighter adaptation illumination [**30**]. Contrast sensitivity as a function of adaptation level is shown in Figure 4-3 where 10^{-2} cd/m^2 corresponds to just less than full moon lighting, 10 cd/m^2 is roughly equal to the lower limit of home or office interior lighting, and daylight can easily exceed many thousands of cd/m^2 [**31**].

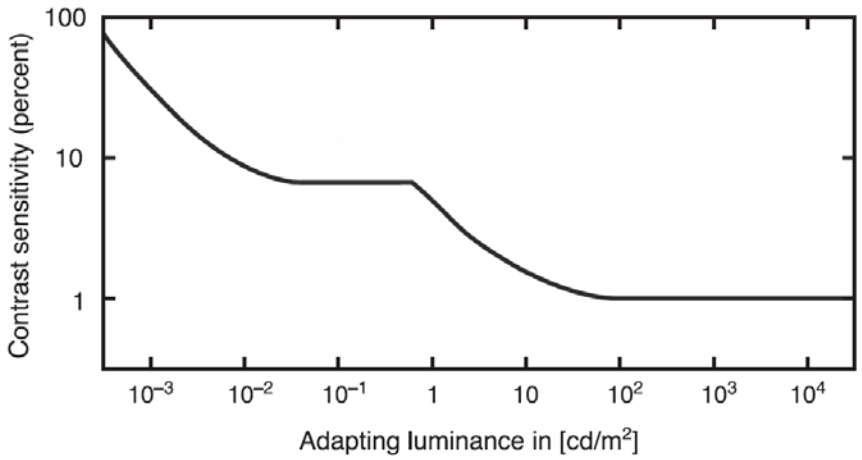

Figure 4-3. Plot of contrast sensitivity versus adapting luminance for the human eye [**30**]. This shows that contrast sensitivity is heavily dependent on adaptation luminance. Many displays and imaging systems operate at luminance levels of greater than 10^2 cd/m^2.

The human eye also has variable sensitivity to information presented at different spatial frequencies. While the optical transfer function of the eye is not linear, and is sensitive to orientation and location in the field of view, in general the human visual system is most sensitive at spatial frequencies of roughly two to three cycles per degree before and after which the sensitivity drops quickly. The relationship between contrast sensitivity and spatial frequency is known as the contrast sensitivity function, and can be used to describe the human ability to perceive details in a scene, known as visual acuity [**32**].

4.1. Color Perception and Modeling

While all visual metrics are somewhat subjective, color discrimination is perhaps the most so since electromagnetic waves have no color in themselves; there is no fundamental difference between visible light waves and other invisible electromagnetic

waves, other than the wavelength. The perception of color is therefore the human interpretation of the relative stimulus of the three types of color receptors in the eye. This leads to an important aspect of color perception, known as metamerism, where any perceivable color can be matched using a combination of other wavelengths that provide the same relative stimulation to the cone receptors in the eye [**11**]. These receptors effectively integrate over a wide range of wavelengths (as shown in Figure 4-2) and produce a signal of the total illumination in that area. This total response is a linear function which can be shown as

$$\int_{400\text{ nm}}^{700\text{ nm}} I(\lambda) f(\lambda) \mathrm{d}\lambda \tag{4-2}$$

where $I(\lambda)$ is the intensity of incoming light and $f(\lambda)$ is the sensitivity of the receptor at each wavelength [**33**]. A single wavelength of light will be perceived to have a specific color and several wavelengths of light can be combined in specific ratios to produce the perception of a color identical to that of the monochromatic source. This is the basis for tri-chromatic theory and allows the reproduction of a wide range of colors through the mixing of three colored sources [**11**]. In order to predict the amounts of different wavelengths needed to produce the perception of a specific color, detailed Color Matching Functions (CMFs) have been created by having test subjects adjust the amount of illumination from three differently colored light sources in order to match an illumination of a specific wavelength [**34**]. One of the first CMFs is the 1931 Standard Colorimetric Observer developed by the Commission Internationale de l'Eclairage (CIE).

This was based on a small number of test subjects but allowed for the creation of the relationships shown in Figure 4-4 where a subject used variable amounts of light sources at 700 nm ($\bar{r}$), 546.1 nm ($\bar{g}$), and 435.8 nm ($\bar{b}$) (the latter two corresponding to prominent green and violet, respectively, lines of the mercury lamp) in order to match the color of a test area that was 2 degrees in visual angle (approximately the size of the fovea, the most color-sensitive section of the human eye) [**34**].

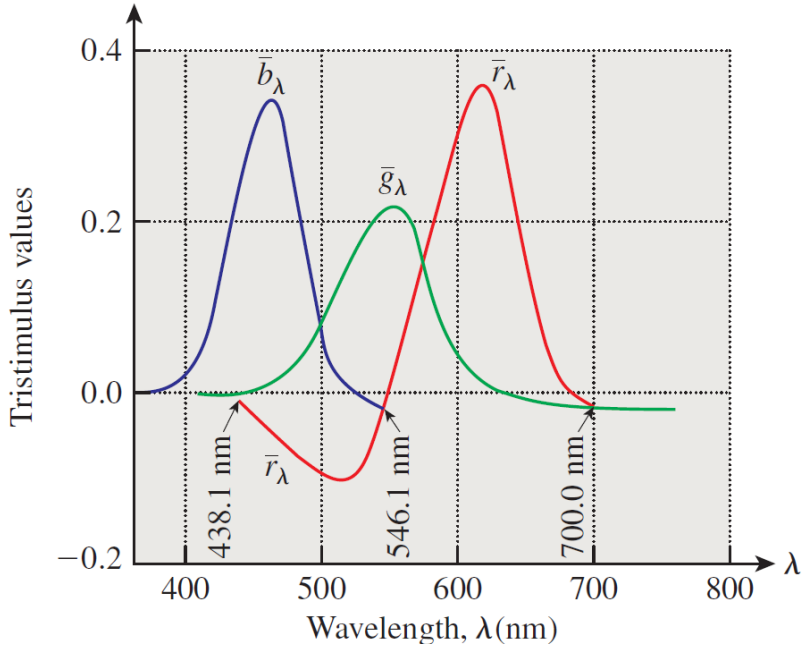

Figure 4-4. Plot of the color matching functions for 1931 2deg standard observer [**33**]. These were some of the earliest color matching functions developed.

More recently, updated and more accurate CMFs have been proposed to better model the response of the HVS [**35**]. One of the most recent versions of these are the XYZ CMFs transformed from the CIE (2006) physiologically-relevant long-, middle-, and short-wavelength-sensitive (LMS) cone fundamental CMFs, available from the Color & Vision

Research Laboratory [**35**]. The range of colors that can be produced by a given set of light sources, known as primaries, is known as the color space or the gamut. The negative section of the red matching function shown in Figure 4-4 is an area where the red primary had to be subtracted from the color that was being matched in order to achieve the same perception. This is an area outside the gamut for the three primaries shown in the $\bar{r}$, $\bar{g}$, $\bar{b}$ color matching functions. The amount of each of these primaries needed to match any given color can be determined by

$$c_{\mathrm{r}} = \int_{400\ \mathrm{nm}}^{700\ \mathrm{nm}} P(\lambda)\bar{r}(\lambda)\mathrm{d}\lambda, \tag{4-3}$$

$$c_{\mathrm{g}} = \int_{400\ \mathrm{nm}}^{700\ \mathrm{nm}} P(\lambda)\bar{g}(\lambda)\mathrm{d}\lambda, \tag{4-4}$$

$$c_{\mathrm{b}} = \int_{400\ \mathrm{nm}}^{700\ \mathrm{nm}} P(\lambda)\bar{b}(\lambda)\mathrm{d}\lambda, \tag{4-5}$$

where c is the amount of each primary, $P(\lambda)$ is the spectral power distribution (SPD) of the color to be matched and $\bar{r}$, $\bar{g}$, $\bar{b}$ are the three components of the matching function. In order to eliminate the negative section of the $\bar{r}$ matching function, the CIE defined three new primaries called X, Y, and Z with the property that these primaries would encompass the entire observable color space [**34**]. The Y primary was also designed the exactly match the aggregate response of the three human cones, in order to give a measure of the

overall brightness of any spectral power distribution. This allows any spectral light *C* to be matched by a combination of the three primaries, as

$$C = X\mathbf{X} + Y\mathbf{Y} + Z\mathbf{Z} \tag{4-6}$$

where the bold script indicates the primary and the light script indicates the amount of each primary. The $\bar{x}, \bar{y}, \bar{z}$ color matching functions are shown in Figure 4-5.

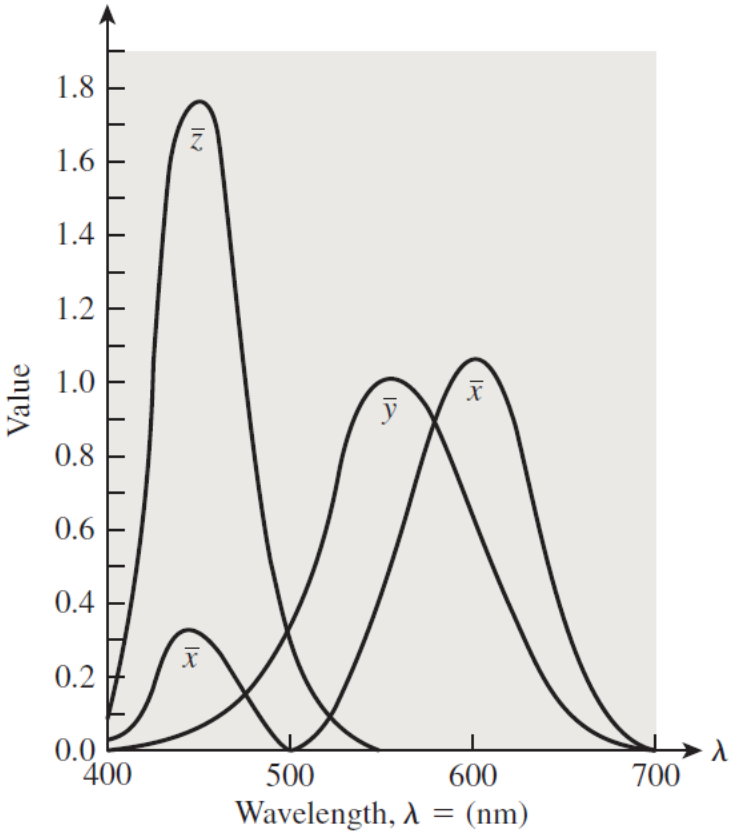

Figure 4-5. Plot of the $\bar{x}, \bar{y}$, and $\bar{z}$ color matching functions for the CIE X, Y, Z primaries [**33**]. These were designed to eliminate the negative region in the original $\bar{r}, \bar{g}, \bar{b}$ CMFs.

It can be observed that the matching functions are normalized such that the $\bar{y}$ matching function peaks at a value of exactly 1.0 at approximately 555 nm, the wavelength to which the eye is most sensitive. Integrating any spectral power source over the $\bar{y}$ matching function can give a measure of the total luminous efficiency of the light source, or the total brightness that will be perceived. The X, Y, Z primaries for any given spectral power distribution can then be given by

$$X = k_\lambda \int_{400\text{ nm}}^{700\text{ nm}} P(\lambda)\bar{x}(\lambda)d\lambda, \tag{4-7}$$

$$Y = k_\lambda \int_{400\text{ nm}}^{700\text{ nm}} P(\lambda)\bar{y}(\lambda)d\lambda, \tag{4-8}$$

$$Z = k_\lambda \int_{400\text{ nm}}^{700\text{ nm}} P(\lambda)\bar{z}(\lambda)d\lambda, \tag{4-9}$$

where k_λ is a photometric constant equal to 680 lm W^{-1} for emissive sources [**11**]. For partially transmitting mediums or reflective surfaces, k_λ is defined as

$$k_\lambda = \frac{100}{\int S(\lambda)\bar{y}(\lambda)d\lambda} \tag{4-10}$$

where $S(\lambda)$ is the relative spectral distribution of the light source [**11**]. The values are often scaled so that Y has a maximum of 100. If relative amounts of color are desired, it can be useful to eliminate the overall effects of brightness by dividing the amount of each primary by the sum of the three as

$$x = \frac{X}{X + Y + Z}, \tag{4-11}$$

$$y = \frac{Y}{X + Y + Z}, \tag{4-12}$$

$$Z = \frac{Z}{X + Y + Z}. \tag{4-13}$$

These three values then define an intensity- and device-independent color space which can be visualized by the CIE chromaticity diagram shown in Figure 4-6. The dark spot in the middle of the diagram is the location at which all wavelengths are roughly equal, and the resulting light will be perceived as close to white.

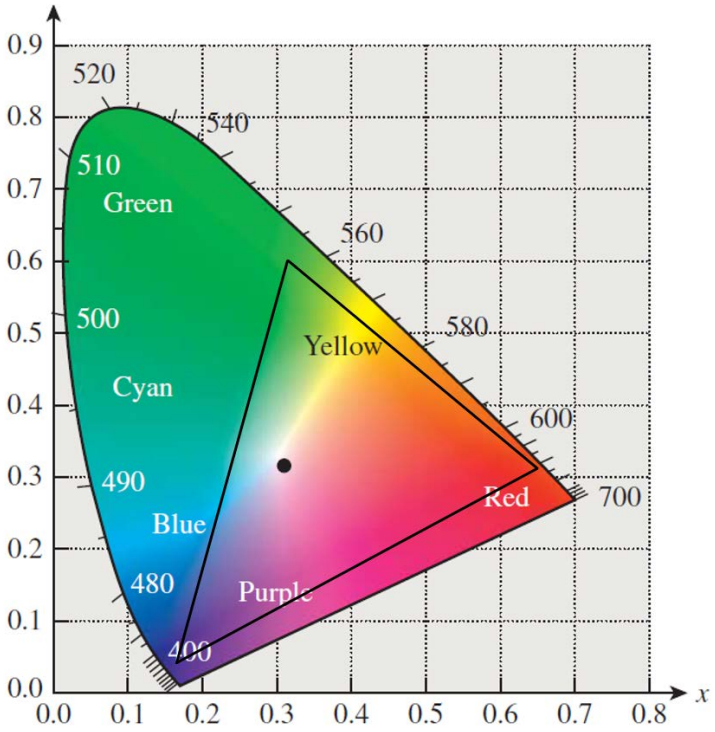

Figure 4-6. Plot of the CIE chromaticity diagram where the edge of the colored space corresponds to monochromatic light sources[**33**]. The color gamut of a standard sRGB color display is represented by the area inside the triangular region shown.

According to Figure 4-6, any monochromatic light source can be shown as a location along the curved edge of the colored area, and the colors along the flat bottom edge cannot be achieved using any single wavelength. Any two light sources can produce the range of colors on the line between them, and three sources can produce the colors enclosed inside the boundary formed by connecting them with straight lines. The R, G, B primaries and corresponding color space used in many modern electronic color displays are approximately shown by the triangular region in Figure 4-6 [**34**].

4.2. Perceptual Color Spaces and Color Difference Calculation

In order to accurately predict how different combinations of light will be perceived by the HVS, it is useful to have a method to calculate the difference between two colors. While the XYZ chromaticity diagram does define all observable colors, the space of the diagram does not linearly relate to the experience of color; the distance between two points on the diagram has a low correlation to the actual perceived difference between the colors. Therefore, it is necessary to define a perceptual color space that more closely matches the sensitivity of human color perception. Among many perceptual color spaces, the CIE L*a*b* color space (also known as Lab) is the most popular and widely used [**34**]. The L^* component defines the luminance that is proportional to the energy of the light and is given by

$$L^* = \begin{cases} 116(Y/Y_{\mathrm{n}})^{\frac{1}{3}} - 16 & Y/Y_{\mathrm{n}} < 0.008856 \\ 903.3Y & Y/Y_{\mathrm{n}} \geq 0.008856 \end{cases}, \tag{4-14}$$

where Y_{n} is the intensity value of a reference white. The other two components, a^* and b^*, can then be given by

$$a^* = 500\left[(X/X_{\mathrm{n}})^{\frac{1}{3}} - (Y/Y_{\mathrm{n}})^{\frac{1}{3}}\right], \tag{4-15}$$

and

$$b^* = 500\left[(Y/Y_{\mathrm{n}})^{\frac{1}{3}} - (Z/Z_{\mathrm{n}})^{\frac{1}{3}}\right], \tag{4-16}$$

for moderate levels of illumination where cones are active (the photopic range) and where X_{n} and Z_{n} are values for a reference white point. The reference white point is determined by the illumination spectrum that is used, and is generally equal to a surface that reflects all wavelengths of light equally. This can be calculated using the CMFs for the appropriate observer and the given illumination spectrum. For cases where the range of illumination extends to sufficiently low levels that scotopic (rod dominated) vision takes over, the calculation of the *L**, *a**, and *b** values must be adjusted [**36**]. The L*a*b* model, shown in Figure 4-7, uses the opposing red-green and yellow-blue color pairs and is much more perceptually uniform than the XYZ color space. This allows for color differences to be roughly approximated by calculating the Euclidean distance (along *L*, *a*, and *b*, coordinates) between two points.

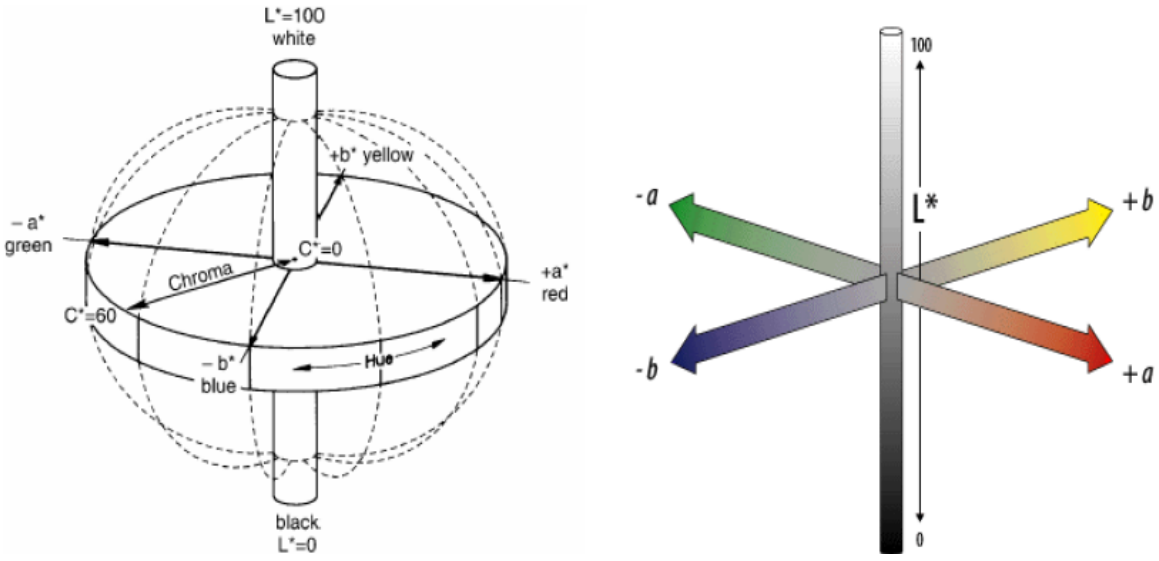

Figure 4-7. Representation of CIE L*a*b* color model[**37**]. The *L* axis defines lightness while the *a* and *b* axes define the opponent color pairs red-green and yellow-blue, respectively.

The color difference metric that is generally used is called delta E, and, in the case of the L*a*b* model, the color difference is represented by ΔE^*_{ab} which can be calculated by

$$\Delta E^*_{\mathrm{ab}} = [(\Delta L^*)^2 + (\Delta a^*)^2 + (\Delta b^*)^2]^{1/2} . \tag{4-17}$$

This color difference was proposed in 1976 and is also known as CIE76, de76, or simply ΔE^*. However, this does not provide a perceptually uniform color difference because the HVS is slightly less sensitive to changes in color (a^* and b^*) than it is to changes in brightness (L^*) and the CIE76 method has only approximately a 75% agreement with human vision. Other, significantly more complicated color difference methods have been proposed, including CIE94 which achieves 95% agreement with human vision and the

CIEDE2000 method which is the most computationally intensive and is being refined [**37**]. Since color models are used extensively in industry to determine acceptable color matching in material goods, it is critical to have an accurate and precise measurement for the difference of color and to predict the color difference that will be noticeable.

In order to perform perceptually uniform color difference calculations, the CIEDE2000 color difference formula is used to account for some of the non-uniformities in the CIELAB color space, especially for small color differences. This formula includes many different correction factors that increase the accuracy color difference calculations. This is especially apparent in the blue regions of the CIELAB color space, and it has been shown that the CIEDE2000 formula outperforms other color difference methods including the CIE76, color measurement committee color difference CMC(l:c) (often used in the textile industry), and CIE94 methods [**34**] [**38**]. While the CIEDE2000 method has been shown to provide high quality results, its implementation is substantially more complicated than for other formulas. Current work in the field of colorimetry includes the development of a new color space that would allow accurate color differences using a Euclidian distance method similar to the original de76 method. Even though the de76 method has been shown to be non-uniform and its use is no longer recommended, it is still often used in industry due to the simplicity of its implementation.

The use of perceptual color modeling and color difference calculations allows for the determination of the correlation between the spectral output of an optical readout mechanism and the perceptual sensitivity of a human observer. This can be used to

evaluate the theoretical temperature sensitivity of direct view IR imaging systems based on the color differentiation sensitivity of a human observer, and to determine the most suitable readout for the development of a direct view system. The steps that are required for the analytical evaluation, based on the performance of the HVS, of an optical readout system are given by the flowchart in Figure 4-8.

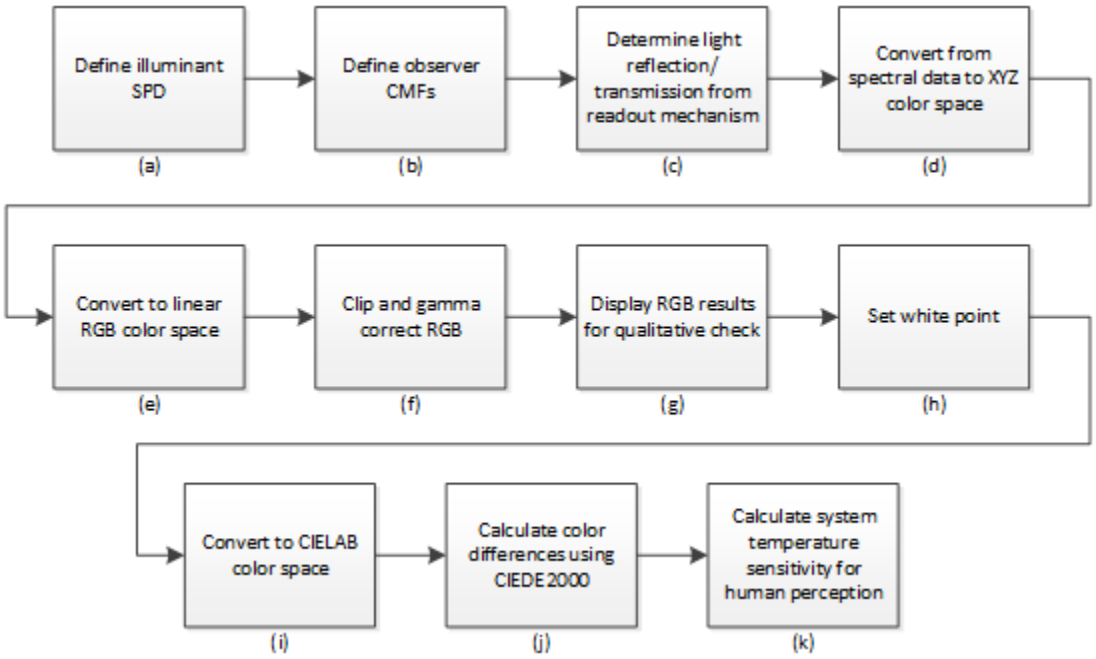

Figure 4-8. Flow chart of the process for the analytical evaluation of optical readout mechanisms: (a) the process starts with the definition of the illuminating light that is present in the system and completes with (k) the determination of the temperature sensitivity, based on a human observer, of an IR imaging system given a particular optical readout method. This is the process that is applied to evaluate and compare the different optical readout mechanisms that were considered for the development of a direct view system.

Any optical readout system must have some source of visible light illumination containing a particular spectral power distribution. The illuminant is defined in Figure

4-8a in order to determine the wavelengths of light that will be present in the optical system and which can be utilized to convey information to a human observer. The observer color matching functions (CMFs) are then defined in Figure 4-8b, based on the sensitivity of the HVS to different wavelengths of light. The CMFs provide a bridge between the spectral power output of an optical readout and the light sensitivity of a human observer that could view the output from the optical system. The interaction between an optical readout mechanism and the physical deformation of the thermomechanical structures in an FPA is then calculated in Figure 4-8c in order to determine the spectral output from the IR imaging system, based on the temperature of a scene. The spectral power is then converted into the human vision color space in Figure 4-8d in order to determine the perceived color that is produced by the relative response of the three types of cone receptors in the human eye. A qualitative check of the previous processes can be performed by transforming the data from the human vision color space to the color space of an electronic display, given in Figure 4-8e, so that the data may be presented on a computer monitor or similar display. These data must be gamma corrected to match the gamma decoding that will be used by a given display and also corrected to account for color gamut limitations of a standard three color (sRGB) display, as given in Figure 4-8f. This ensures that relative colors presented on an electronic display will more closely match the colors that would be observed from the actual optical readout, and allow for the displayed colors to be used as a qualitative intermediate check in Figure 4-8g. If the displayed colors are qualitatively similar to what might be expected from an optical readout, then the quantitative evaluation process can continue with the

definition of a white point in Figure 4-8h. The white point accounts for illumination and ambient light adaptation of the HVS, and specifies the color that would be perceived as pure white in order to accurately determine the relative perception of other colors. The color data can then be transformed from the XYY human vision color space to the CIELAB perceptual color space in Figure 4-8i. This perceptual color space more closely matches the perception that results from the opponent process that the human brain uses to interpret the relative signals from the different cone cells in the eye, and provides a color space from which perceptual color differences can be calculated. The CIEDE2000 color difference formulas can then be used in Figure 4-8j to determine what changes in color will be consciously noticeable by a human observer, and what different colors would be indistinguishable. The change in temperature of a scene, and corresponding thermomechanical deformations in an FPA, which would result in a noticeable change in color for a particular optical readout, can then be determined in Figure 4-8k in order to quantitatively define temperature sensitivity of the IR imaging system. This metric for the smallest noticeable change in scene temperature can be used to determine the suitability of an optical readout for the development of a direct view system, and for the comparison of different optical readout methods. A description of the Matlab algorithm that was developed, along with the source code used, to implement the processes described in Figure 4-8 and compare several optical readouts, is contained in Appendix D.

5. Methods

The MEMS FPA uses bimaterial cantilever structures to transduce infrared radiation from a scene into nanometer scale mechanical displacement. However, the scale of the displacement exhibited by the structures of the FPA is too small for it to be easily directly observed with the naked eye. In order to achieve a direct viewer using purely optomechanical methods and without the use of any computer processing, a readout system must transduce the deformation of the structures in the FPA into a stimulus that is easily detectable by the HVS. Working inside the constraints imposed by both the performance of the current FPA and the abilities of the human visual system, it is necessary to develop a readout mechanism that presents thermal information about a scene in the form of brightness or color information that can be perceived and interpreted by a human observer. Perceived brightness is a result of the amount of light that enters the human eye, while perceived color is a result of the specific mixture of light wavelengths that are present. To this end, several potential readout mechanisms were identified in order to transduce the physical deflection of the structures in the FPA into visible images based on either changes monochromatic brightness or variations in perceived color. As shown in Figure 5-1, three readout mechanisms were considered, two based on interferometry and a third based on geometrical optics.

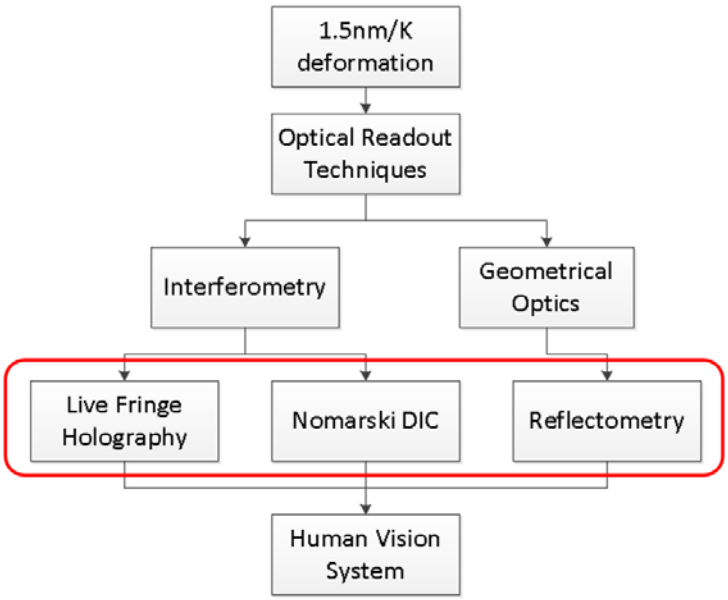

Figure 5-1. Optical readout methods identified for the transduction of nanometer scale microcantilever displacement into perceivable light output. Three readouts were considered, two based on interferometry and a third based on geometrical optics.

The first readout mechanism investigated uses live holographic interferometry to produce a visible fringe pattern of brightness based on the deformation of the sensing elements of the array. A hologram is used to record, and then recreate, the wavefront of light reflected from the FPA in a relaxed or reference state. A live wavefront of light reflected from the FPA in a heated state is then superimposed on a reference wavefront of light, and changes between the two will be visible. When the elements of the FPA deform, the difference between the wavefronts causes interference which can be observed as changes in brightness while the color remains similar to that of the illuminating source.

The next mechanism presented is based Nomarski Differential Interference Contrast (Nomarski DIC), where white light is sheared to create two orthogonally polarized

wavefronts which are reflected off slightly different locations on the FPA. The two wavefronts are then re-aligned and superimposed before being directed towards an observer. When elements of the FPA deform and create a sloping surface, adjacent reflected light waves will have different path lengths. This results in interference when the waves are superimposed. The many wavelengths of light contained in the white light illumination all interfere slightly differently, and the result is that as the elements of the FPA deform, the observed intensity at some wavelengths is decreased while the observed intensity at other wavelengths is increased. This leads to the perception of changes in color based on the angle of the surface of the elements of the FPA. The final mechanism is based on geometrical optics, and does not directly involve interference. This mechanism will be referred to as reflectometry and uses the thermally-induced changes in shape of the micro-cantilever elements to change the angle at which light is reflected from the FPA. The light can be either reflected towards an observer, or away from an observer, based on the deflection of the cantilever elements caused by infrared radiation from a scene. This will vary the amount of light that is observed in order to produce either changes in brightness when a single light source is used. If several differently colored light sources are used, this readout mechanism can produce changes in the ratio of light from these sources which is observed, resulting in a change in color. This approach offers significant adjustability based on the arrangement of the components of the readout, and the optics used.

5.1. Optical Readout Mechanisms

5.1.1. Live Holographic Interferometry

Interferometry relates to a variety of methods that make use of superimposed electromagnetic wavefronts in order to extract information about the individual wavefronts. It has wide ranging applications but the use of visible light interferometry for optical metrology is of particular relevance since it allows for measurements of small scale features and displacements. In order for interference in electromagnetic waves to occur, the wavefronts must have either a constant relative phase in space or in time. These conditions are known as spatial and temporal coherence, respectively. Temporal coherence is of particular interest because, given the speed of light in a particular medium, the maximum time delay between two wavefronts that still remain coherent defines the coherence length of the light source. The coherence length is then the maximum optical path length difference between two waves that will still experience interference. Interference between two coherent light waves behaves similarly to the interference experienced by physical waves; constructive interference, which occurs where peaks of a wave are in phase, causes an increase in the amplitude while destructive interference, where the two waves are out of phase, causes a decrease in amplitude. If the amplitude of the two interfering waves are equal, and the waves have no phase difference, the resulting amplitude will be the sum of the two waves, or twice the amplitude of either original wave due to complete constructive interference. If two

waves with a phase difference of 180 degrees (π radians) interfere, the resulting amplitude will be the difference between the two waves. In the case of equal amplitude waves, the result will have no amplitude due to complete destructive interference [**39**]. Figure 5-2a shows an example of constructive interference in waves with equal magnitude and no phase difference, where the result is a wave with twice the amplitude of the two initial waves while Figure 5-2b shows an example of destructive interference in out-of-phase waves with equal magnitude, where the result is a wave with no amplitude.

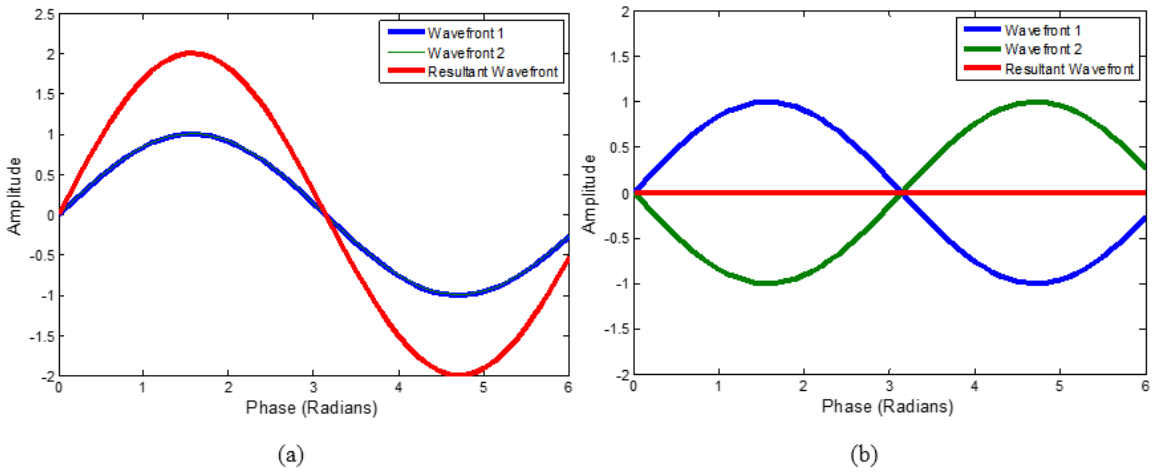

Figure 5-2. Interference of wavefronts: (a) waves with no phase difference interfering constructively; and (b) waves with a phase difference of pi radians interfering destructively [**14**].

Live holographic methods use interferometry to measure deformation in complex shapes through the superposition of wavefronts. A hologram can be used to exactly recreate a wavefront, and allows the real time interference of a wavefronts from an object in two or more states. If the two wavefronts are identical, they will experience constructive

interference at every point, however, any differences between the two wavefronts will cause varying states of interference, and the formation of observable interference pattern or “fringes” which correspond to areas of larger amplitude (greater perceived light intensity) and smaller amplitude (lower perceived brightness).

A holograph is the recording of the interference between a wavefront created by an object and a separate, coherent, reference wavefront. While standard photographic film and imaging sensors can only record the amplitude (brightness) of light, phase information about the wavefronts is needed in order to perform interferometric measurements on a surface or object. The changes in amplitude due to interference of coherent waves is the key mechanism which allows phase information to be encoded and recorded as a visible interference pattern. Figure 5-3 shows an arrangement that can be used to record the interference pattern between two coherence wavefronts [**40**].

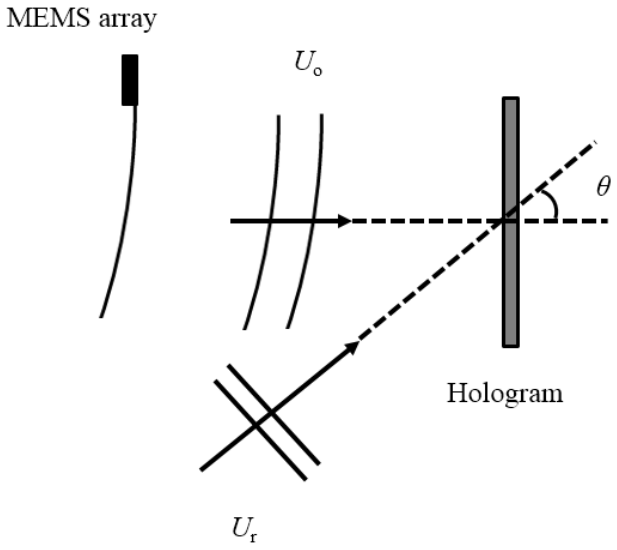

Figure 5-3. Recording of the interference pattern between two coherent wavefronts. The hologram records the superposition of the reference wave, U_r, and the object wave, U_o, reflected from the MEMS array.

In Figure 5-3 U_o is the wavefront reflected from the object and U_r is a planar reference wavefront. Each wavefront contains a complex amplitude and is a function in space (the *x* and *y* directions along the wavefront) and time, *t*, (as the wavefront propagates). The complex amplitude of the two wavefronts can then be written as

$$U_o(x,y,t) = |U_o(x,y)|e^{i[-\phi_o(x,y)+\omega(x,y)t]}, \tag{5-1}$$

and

$$U_r(x,y,t) = |U_r(x,y)|e^{i[-\phi_r(x,y)+\omega(x,y)t]}, \tag{5-2}$$

where $|U_o(x,y)|$ and $|U_r(x,y)|$ are the amplitudes of the two waves, ϕ_o and ϕ_r are the phases of the two waves, respectively, and ω is the frequency of the waves. When the waves are superimposed, the result is the sum of the two complex amplitudes, given by

$$U(x,y,t) = U_o(x,y,t) + U_r(x,y,t), \tag{5-3}$$

where $U(x,y,t)$ is the complex amplitude of the combined waves. The interference pattern and intensity of light which can be observed, *I*, is then given by

$$\begin{aligned} I &= (U_o + U_r)(U_o^* + U_r^*) \\ &= U_o U_o^* + U_r U_r^* + U_o^* U_r + U_r^* U_o, \end{aligned} \tag{5-4}$$

where the dependence on (*x*, *y*, *t*) has been omitted to simplify representation and the asterisk is used to denote a complex conjugate. The intensities of the object and reference waves, $I_o = |U_o|^2 = U_o U_o^*$ and $I_r = |U_r|^2 = U_r U_r^*$ respectively, do not contain any information about the phase of the waves, while the last two terms from Eq. 5-4 can be written as

$$\begin{aligned} U_o^* U_r + U_r^* U_o &= |U_o||U_r|\left[e^{i(\phi_o - \phi_r)} + e^{i(\phi_r - \phi_o)}\right], \\ &= 2|U_o||U_r|\cos(\phi_o - \phi_r) \end{aligned} \tag{5-5}$$

$$= 2\sqrt{I_{\mathrm{o}} I_{\mathrm{r}}}\cos(\phi_{\mathrm{o}} - \phi_{\mathrm{r}}),$$

where the resulting intensity depends on the phase difference of the two waves. This creates the interference pattern that can be observed or recorded on a photosensitive medium to create a hologram. Finally, the complete representation for the intensity resulting from two interfering waves can then be shown by rewriting Eq. 5-4 as

$$I = I_{\mathrm{o}} + I_{\mathrm{r}} + 2\sqrt{I_{\mathrm{o}} I_{\mathrm{r}}}\cos(\phi_{\mathrm{o}} - \phi_{\mathrm{r}})\,. \tag{5-6}$$

If the intensity recorded as a hologram, *I*, has the same transmittance as the original interference pattern, and is then illuminated by the reference wave, the result can be shown as

$$U_{\mathrm{r}} I = U_{\mathrm{r}}|U_{\mathrm{r}}|^2 + U_{\mathrm{r}}|U_{\mathrm{o}}|^2 + U_{\mathrm{r}} U_{\mathrm{r}}^{*} U_{\mathrm{o}} + U_{\mathrm{r}} U_{\mathrm{r}} U_{\mathrm{o}}^{*}, \tag{5-7}$$

where the third term is of particular interested because it is the original object wave modulated by the intensity of the reference beam. With a constant intensity reference beam of the appropriate power, this can be observed as an exact reconstruction of the object wavefront as shown in Figure 5-4 [**41**].

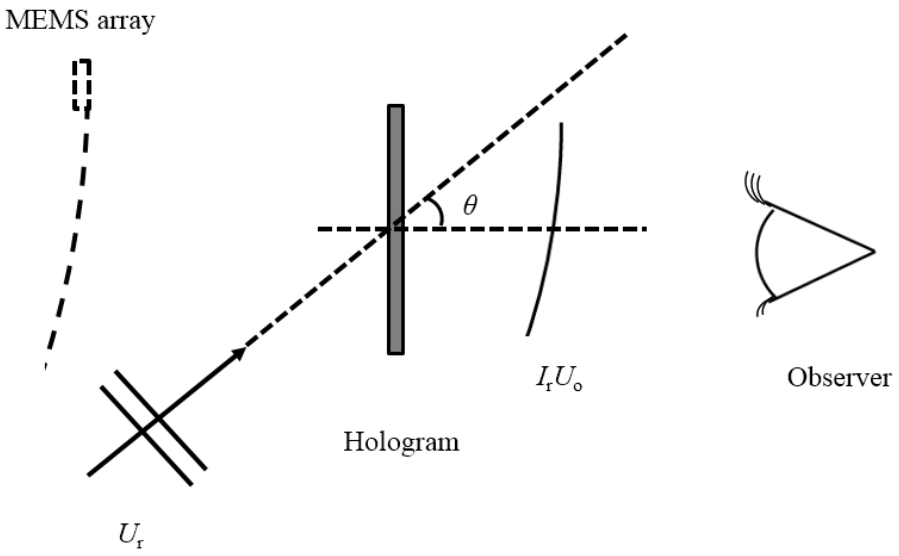

Figure 5-4. Hologram illuminated with reference beam, U_r, to produce reconstruction of the original object wave, I_rU_o.

Here I_rU_o is the reconstruction of the original object wave, which appears to originate from the same location at which the object was originally placed. Live fringe holographic interferometry can be performed by precisely maintaining the relative positions of the hologram and object, and then illuminating both after the hologram has been developed. The reconstruction of the object wavefront then appears to originate at the object itself, and the two waves can be superimposed to produce interference. If the object is then deformed slightly, the new object wave will cause a change in the interference between the two waves, as shown in Figure 5-5 where U_h is the holographically reconstructed reference beam that interferes with the live object beam U_o.

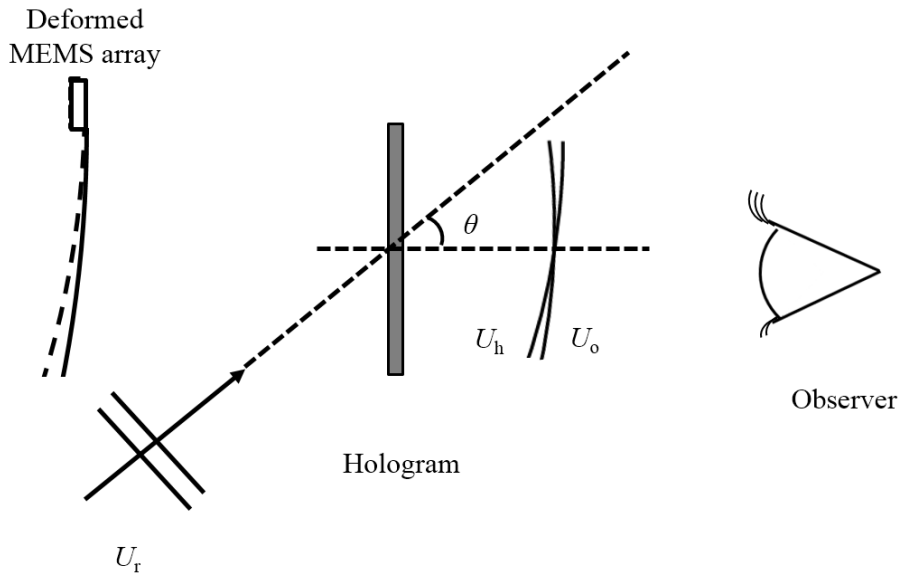

Figure 5-5. Interference of live object wave, U_o, and holographically reconstructed object wave, U_h.

This can be observed as the formation of fringes of constructive and destructive interference visible as light and dark bands that appear to be on the object. The intensity of the superimposed waves at any point can be found using Eq. 5-5 and the result of interference between two waves of equal intensity is shown in Figure 5-6.

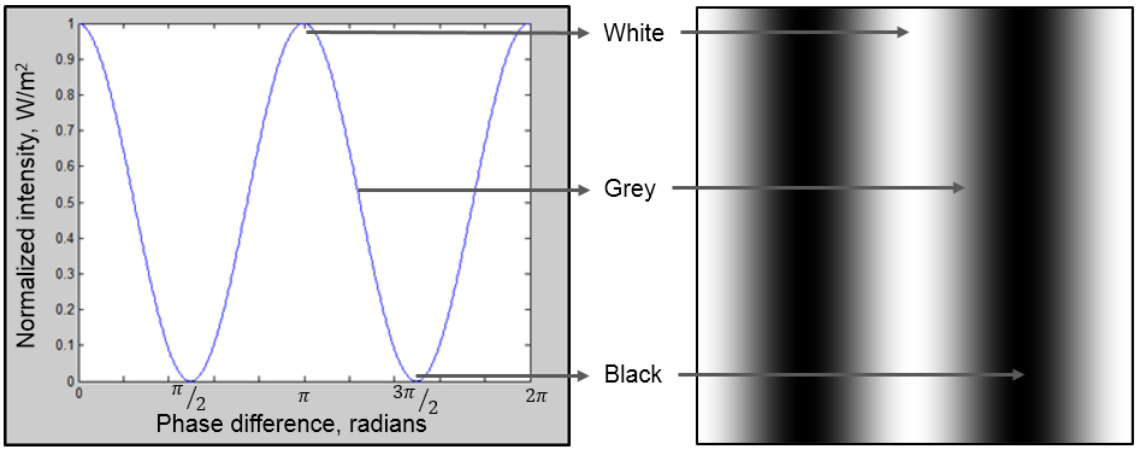

Figure 5-6. Relationship between optical phase difference and intensity ofinterfering waves.

It is often useful to define the phase difference between two waves as the fringe locus function, Ω. This can be shown as

$$\Omega = \phi_o - \phi_r, \tag{5-8}$$

where ϕ_2 and ϕ_1 are the phase of the two interfering waves, such as those from an object and reference. The fringe locus function depends on the geometry of the optical setup, and can be defined as the difference between the angle of the illuminating light and the angle from which an observation is made. For practical purposes, it is sufficient to define a sensitivity vector, $\boldsymbol{K}$, as the difference between the observation vector, $\boldsymbol{K_1}$, and the illumination vector, $\boldsymbol{K_2}$, or

$$\boldsymbol{K}(x, y) = \boldsymbol{K_2} - \boldsymbol{K_1}. \tag{5-9}$$

The magnitude of the wave vectors, K, known as the wave number, or angular wavenumber, is related to the wavelength of the wave and is given by

$$K = |\boldsymbol{K}_1| = |\boldsymbol{K}_2| = \frac{2\pi}{\lambda}, \tag{5-10}$$

where λ is the wavelength. In order to describe the change in shape or position of an object, we then define a displacement vector, $\boldsymbol{D}$, which is given by

$$\boldsymbol{D} = D_x\boldsymbol{i} + D_y\boldsymbol{k} + D_z\boldsymbol{j}, \tag{5-11}$$

where $\boldsymbol{i}$, $\boldsymbol{j}$, and $\boldsymbol{k}$ are unit vectors in three directions and D_x, D_y, and D_z are the respective magnitudes of displacement in those directions. The fringe locus function describes the difference in the relative phase of the two waves. This can be found as the scalar product of the displacement vector and the sensitivity vector [**40**], shown as

$$\Omega(\mathrm{x}, \mathrm{y}) = \boldsymbol{K} \cdot \boldsymbol{D}. \tag{5-12}$$

If the illumination and observation vectors are parallel, then the problem is substantially simplified and becomes one-dimensional as shown in Figure 5-7.

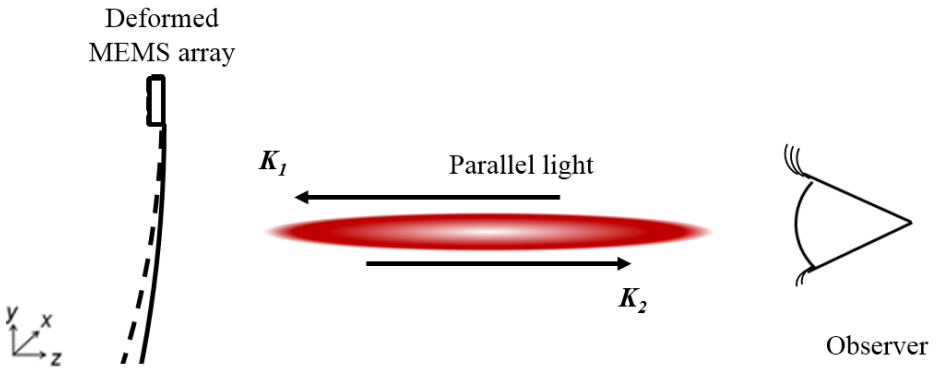

Figure 5-7. Sketch of parallel illumination and observation.

In this case, the sensitivity vector can be simplified due to the lighting conditions, and the resulting dot product is only affected by one component of the displacement vector. This allows the fringe locus function to be

$$\Omega(\mathrm{x},\mathrm{y}) = \frac{4\pi}{\lambda} D_z(x,y), \tag{5-13}$$

where the displacement vector in the z direction is only a function of y along the length of a single cantilever element but a function of x and y across an array of cantilever elements. Eq. 5-6 can then be rewritten as

$$I = I_\mathrm{o} + I_\mathrm{r} + 2\sqrt{I_\mathrm{o} I_\mathrm{r}} \cos\left[\frac{4\pi}{\lambda} D_z(x,y)\right], \tag{5-14}$$

where the resulting intensity will vary from complete darkness to double the intensity of either of the illuminating waves if equal intensity object and reference illumination is used.

In the current application, live fringe holography can be used to observe the superposition of two waves at every point on the FPA using a setup similar to that shown in Figure 5-8.

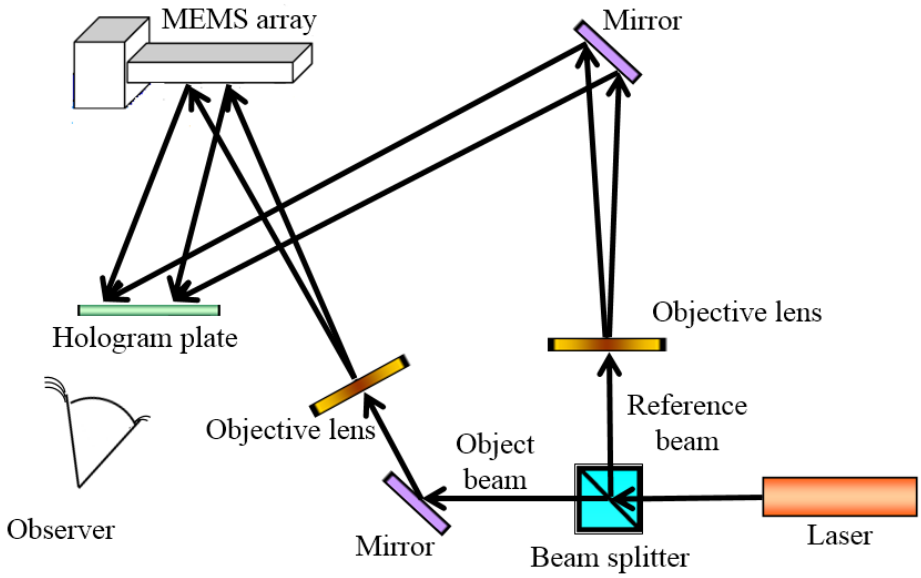

Figure 5-8. Schematic for the readout mechanism based on live holographic interferometry [**42**].

When the cantilever elements in the MEMS array are exposed to infrared radiation from a scene, they will deflect and cause observable fringe patterns due to the interference of the object and reference light wavefronts. This can be observed by looking through the hologram at the FPA where, in ideal conditions, the brightness range will extend from completely black to a bright color determined by the laser wavelength.

5.1.2. Nomarski Differential Interference Contrast (DIC)

Nomarski differential interference contrast (DIC) offers a unique advantage in that it allows for the direct formation of a full range of observable from a single white light source [**43**]. This is especially important because, when combined with the human ability to identify named colors such as red or blue, it then becomes possible to introduce a quantitative element to a direct viewer system; if a direct viewer mechanism can be calibrated to produce an output perceived as a specific color for a certain scene temperature, then the human interpretation is greatly simplified and enhanced. For instance, the ability to observe something cool as having a blue color, while something warm as having a red color, becomes much more easily interpreted than a simple comparison of brightness when using a monochromatic viewer.

Nomarski DIC is a form of interferometry that uses a Wollaston or Nomarski prism to create a shear between two orthogonally polarized components of light. The incident light is polarized using a linear polarizer before it enters the upper wedge of the prism. The prism is made of two cemented wedges of birefringent material, such as quartz or calcite, where the material has a different refractive index depending on its orientation relative to the polarization direction of incident light. The behavior of two orthogonally polarized waves of light interacting with a Wollaston prism is shown in Figure 5-9.

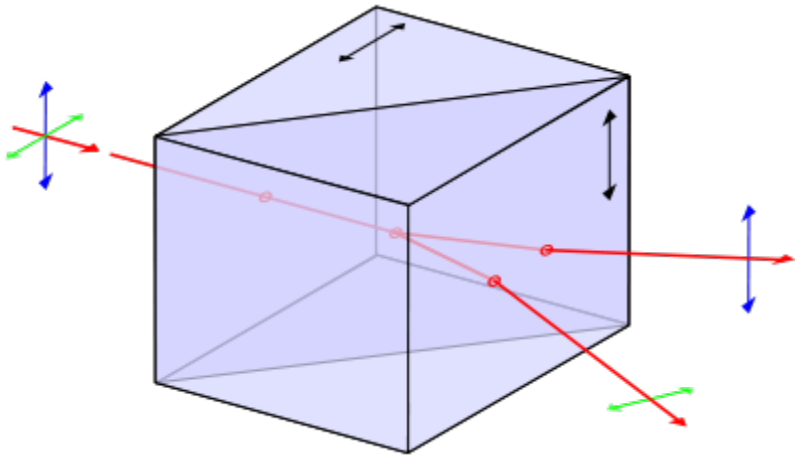

Figure 5-9. Shear of polarized waves interacting with a Wollaston prism [**44**]. The ordinary wave (green indicator) oscillates in a horizontal plane perpendicular to the optical axis (fast axis) of the final wedge of the prism while the extraordinary wave (blue indicator) oscillates on a vertical plane, parallel to the optical axis of the final wedge.

In a Wollaston prism, the two wedges are cut so that their optical fast axes are perpendicular to each other, and also perpendicular to the top and bottom surfaces of the prism. The polarizer can be oriented so that the light entering the prism is polarized at a 45° angle between the optical axes of the two wedges. When light passes through the surface of the prism it is split into two equal waves, the ordinary wave (which vibrates in a direction perpendicular to the optical axis of the wedge) and an extraordinary wave (which vibrates parallel to the optical axis of the wedge), as shown in Figure 5-9.

Because each wave experiences a slightly different refractive index, the waves propagate at slightly different speeds; propagation speed through a medium is inversely proportional to the refractive index, so the wave that experiences the lower refractive index will travel slightly faster. When the light traveling through the prism encounters

the interface between the two wedges, it is refracted when it experiences the change in refractive index at the wedge boundary. The angle of refraction is determined by Snell's Law, which is given as

$$n_1 \sin\theta_1 = n_2 \sin\theta_2, \tag{5-15}$$

where n_1 and n_2 are the indices of refraction for the original and new mediums, and $\sin\theta_1$ and $\sin\theta_2$ are the angles of incidence and refraction, respectively. Thus, if the two waves are traveling parallel through the top wedge of the prism (there was no refraction at the top surface of the prism because the light was incident normal to the surface), they will experience the same angle of incidence at the boundary of the two wedges. However, because the optical axes of the two wedges of the prism are perpendicular, the ordinary and extraordinary waves from the top wedge will switch to become the extraordinary and ordinary, respectively, waves in the bottom wedge. While one wave will experience a decrease in the refractive index, the other wave will experience an increase in the refractive index, and this will lead to each wave having a different angle of refraction. This creates a shear between the two wavefronts as they travel through the bottom wedge, and then exit the lower surface of the prism, as shown in Figure 5-10.

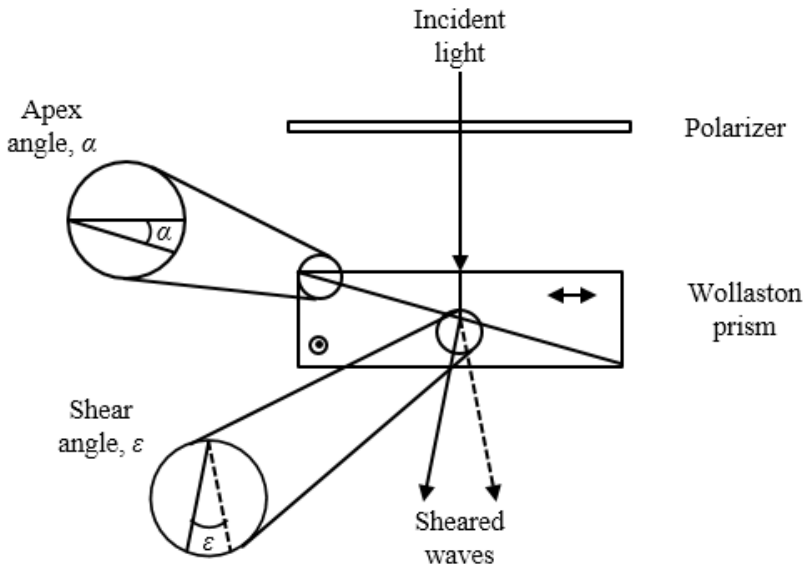

Figure 5-10. Light shear in a Wollaston prism where light is split into two orthogonally polarized wavefronts. The optical axis of the top wedge is normal to the figure while the optical axis of the bottom wedge is horizontal relative to the figure.

The angle of incidence at the wedge boundary is controlled by the apex angle, α, while the difference between the two angles of refraction is controlled by the degree of birefringence of the material; the difference between the two refractive indices, n_1 and n_2. The total included angle between the two exiting waves is given by [**45**]

$$\varepsilon = 2(n_2 - n_1)\tan\alpha, \tag{5-16}$$

where ε is the shear angle between the two light waves.

Where the optical axes of both wedges in a Wollaston prism are perpendicular to both each other and the entry and exit faces of the prism, a Nomarski prism has one wedge

with an optical axis parallel to the surface of the prism and the second wedge cut so that the optical axis is oriented at a specific angle, β, to the top and bottom surfaces of the prism. This is shown in Figure 5-11 where the angle of the optical axis in the Nomarski prism, β, can be modified to control the location of the interference plane for the prism.

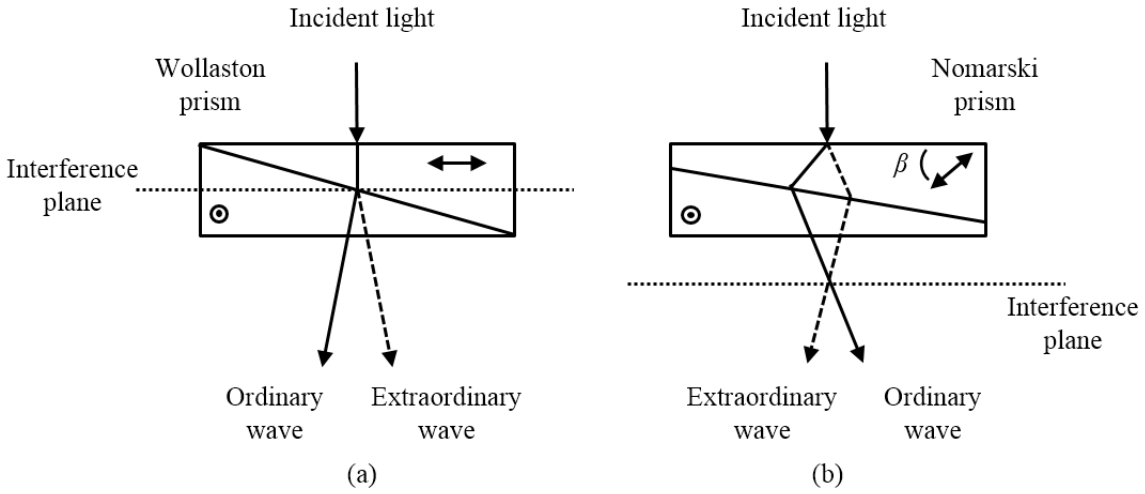

Figure 5-11. Light behavior and interference planes in Wollaston and Nomarski prisms. The Nomarski prism orients the optical axis of one wedge of the prism at an angle, β, to the surface and allows for the formation of the interference plane outside the prism. This allows for compatibility with microscope objectives that have an internal rear focal plane.

Optical systems, including DIC microscopy, can take advantage of the interference plane external to the prism in the case of the Nomarski design so that the rear focal plane of the condenser, or objective, is very near the interference plane of the prism. This allows both waves to be focused onto adjacent, slightly displaced, areas of the specimen. In the case of reflected light DIC, these sheared wave fronts are reflected off of a sample before being re-aligned by passing back through the prism and then caused to interfere through the use of a linear polarizer as an analyzer. By aligning the polarizer at an angle of 45

degrees from the crossed optical axes of the prism, the linearly polarized light will be split into equal ordinary and extraordinary waves in the prism. If the waves are reflected and travel back through the prism to exit coincidentally, they will interfere and be polarized in a plane that is the vector sum of the two waves. If the waves experience no path difference, or a path difference that causes a phase difference equal to an integer coefficient of pi, they will fall back onto the same plane as the original polarized light. This can be achieved by a path difference equal to an integer multiple of the wavelength ($n\lambda$) of the light. If for this case the analyzer is positioned at an angle of 90 degrees from that of the polarizer, and the two waves experience complete destructive interference, no light will be transmitted. This is shown in Figure 5-12 (a) where two components of a light wave experience a phase difference of pi after traveling through a birefringent crystal.

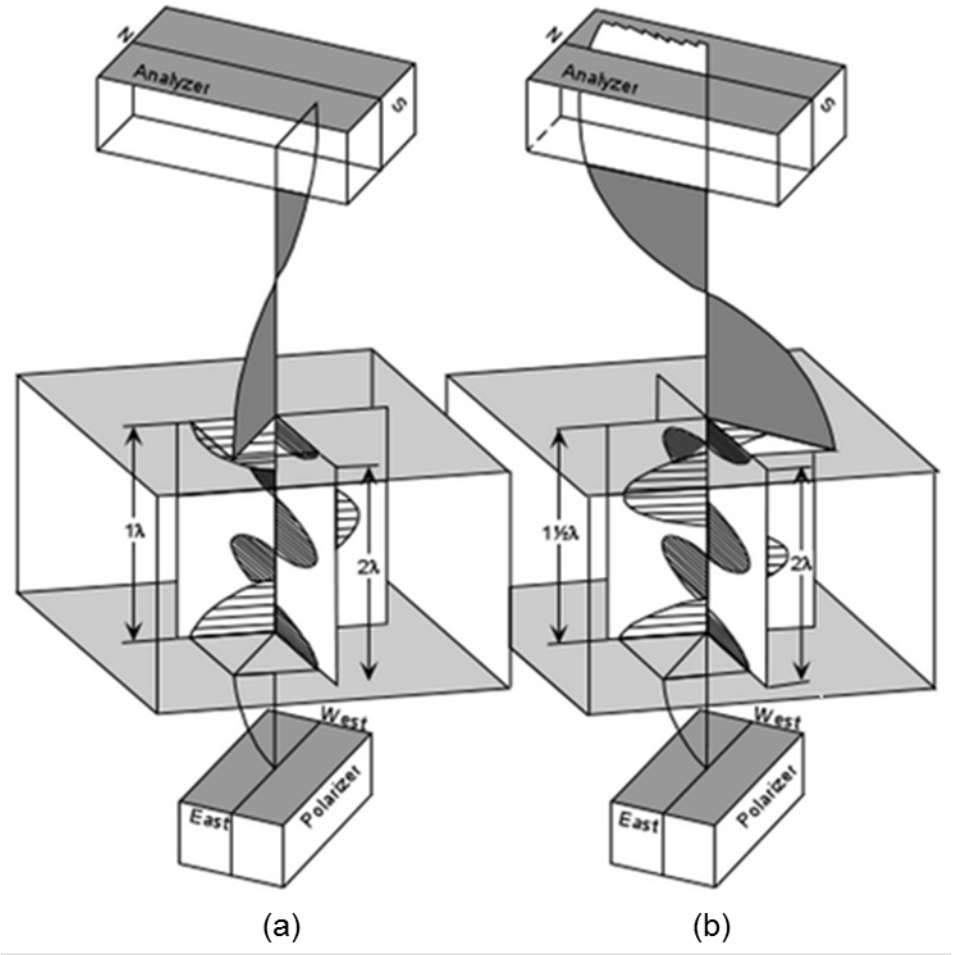

Figure 5-12. Change in polarization plane of light due to phase difference of interfering components. Light is either (a) blocked or (b) transmitted depending the phased difference introduced by the birefringent medium [**46**].

However, if the ordinary and extraordinary waves experience a phase difference of exactly 1/2 pi, caused by a path difference of an odd multiple of ½λ, the interference will cause the resulting wave to exist on a plane 90 degrees away from the polarizer plane. This is shown in Figure 5-12b where the analyzer is in a similar orientation to Figure 5-12a but the rotated light now passes through the analyzer unhindered. These two cases can also be visualized as shown in Figure 5-13.

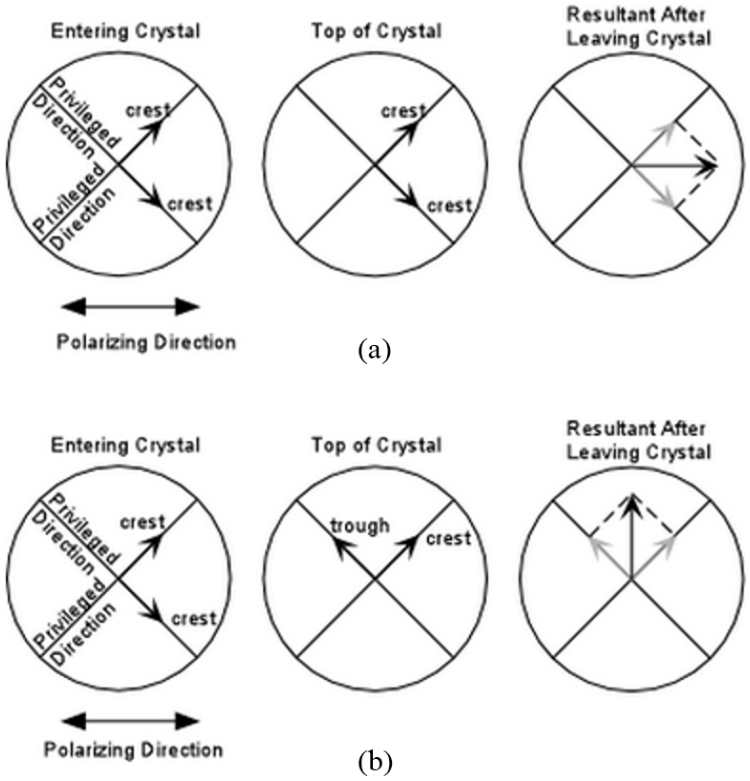

Figure 5-13. Polarization diagrams for phase differences of (a) π and (b) ½π[**46**].

Figure 5-13a shows that the resulting vector sum for waves that experienced no phase difference, or a path difference of nλ, is the same plane as the original polarized light. The vector sum in Figure 5-13b is rotated 90 degrees, demonstrating the case where the waves experience a phase difference of an odd multiple of ½π, or a path difference of an odd multiple of ½λ. The amount of light transmitted through the analyzer, L_λ, is given by [**47**]

(5-17)

$$L_\lambda = \cos^2\varphi - \sin^2(\tau-\varphi)\sin^2(\tau)\sin^2\left(\frac{180^\circ\,\Gamma}{\lambda}\right),$$

where φ is the angle between the polarizer and analyzer planes, τ is the angle between the polarizer and the crystal's closest privileged direction (fast optical axis), λ is the wavelength of the light, and Γ is the path difference between the two waves. For the case of the polarizer and analyzer oriented exactly 90 degrees apart, the resulting intensity of transmitted light can be simplified to

(5-18)

$$L_\lambda(\Gamma,\lambda) = \sin^2\left(\frac{180^\circ\,\Gamma}{\lambda}\right),$$

where it can be observed that the light transmission is purely a function of the wavelength and path difference [**47**]. The total transmission then follows the square of the sine function, as shown in Figure 5-14.

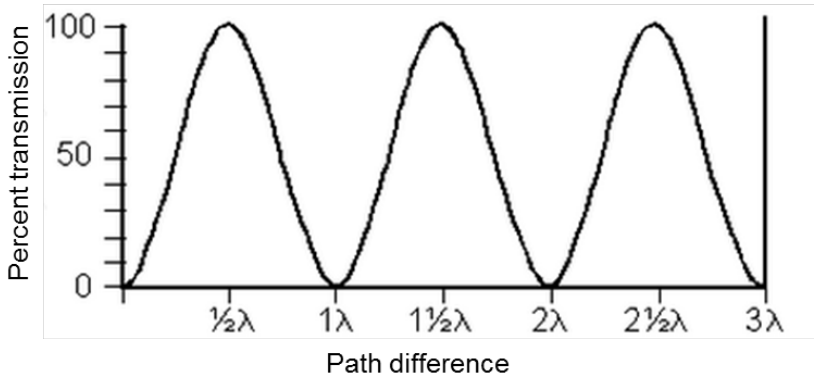

Figure 5-14. Plot of light transmission as a function of path difference for a given wavelength with perpendicular polarizer and analyzer.

Thus, in a white light source used for Nomarski DIC, interference occurs at all wavelengths of light that were reflected from the specimen. All wavelengths in the illumination spectrum will experience the same path difference, but the phase difference will vary according to the relationship between path difference and the particular wavelength. Shorter wavelengths will be more sensitive to path differences when compared to longer wavelengths, and the selective interference at different path lengths will cause a change in the mixture of wavelengths in the observed light. This results in a change in the perceived color. The effects of path length difference on the perceived color are shown in Figure 5-15 where the dashed and dotted lines are interfering waves and the solid traces are the resultant magnitude and Δ represents the path length difference.

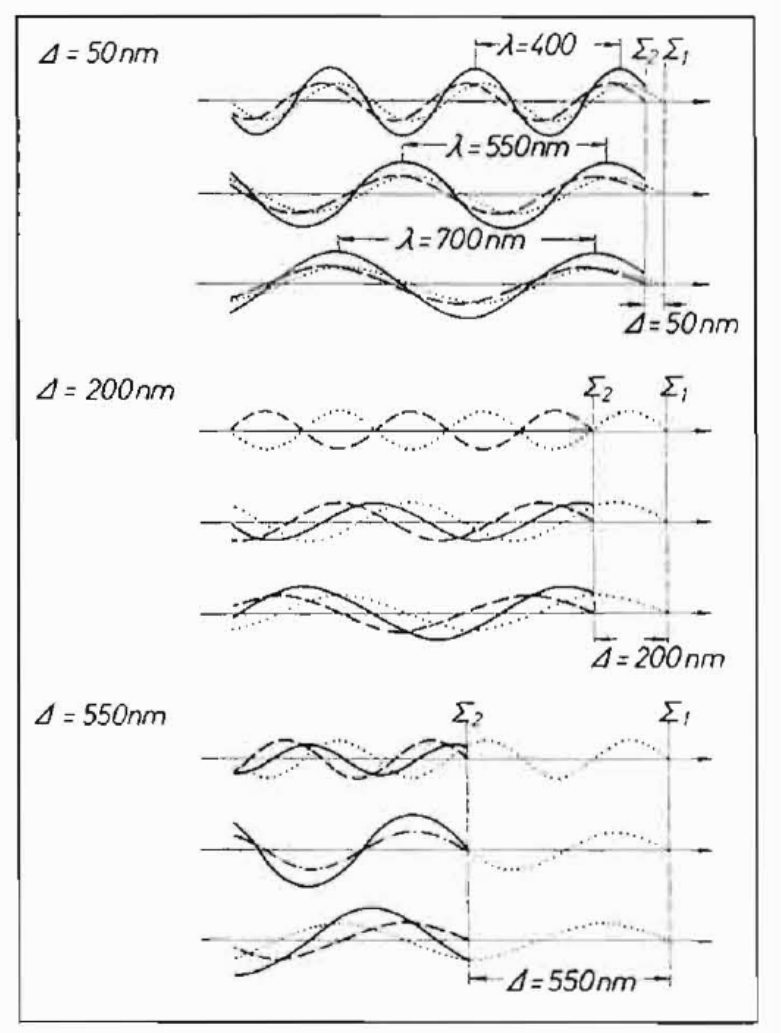

Figure 5-15. Interference of white light at several wavelengths. For clarity shown as three components to represent approximately blue (400nm), green (550nm), and red (700nm). The dashed and dotted lines represent the two interfering waves while the solid line represents the result of interference [**43**].

According to Figure 5-15, it can be observed that while the path difference of 50nm does produces constructive interference at all wavelengths, the path difference of 200nm (½λ for the blue light) exactly cancels out the blue component of the light while still transmitting the green and red light. The path difference of 550nm (1λ for the green

wave) produces constructive interference and increased amplitude in the green channel while producing slightly decreased amplitude for the blue wave and slightly increased for the red wave, respectively.

Nomarski DIC systems often include a method for the introduction or an additional arbitrary phase difference between the two waves. This can be accomplished by introducing an arbitrary angle to the specimen such that there is a slope across the surface relative to the optical axis of the system. Waves reflected from adjacent locations on the specimen will be affected by the local slope and will experience a path difference dependent on severity of the angle. Another method for introducing a phase difference is the lateral translation of the shearing prism such that the waves spend relatively more or less time as the ordinary or extraordinary wave in the prism. The phase difference is determined by the difference in thickness of the two wedges of the prism along the path of the light. A third method is through the use of a de Sénarmont compensator which uses a rotating polarizer along with a quarter-wave plate to introduce a phase difference in the illuminating light; rotation of the polarizer relative to the quarter-wave plate varies the ellipticity of the polarization of the light that is produced. When the elliptically polarized light is incident on the birefringent shearing prism, it is separated into orthogonally polarized components and the result is a change in the relative phase of the two sheared waves.

The mechanism of action of a reflected light Nomarski DIC microscope system applied to image a cantilever element of a FPA is shown in Figure 5-16.

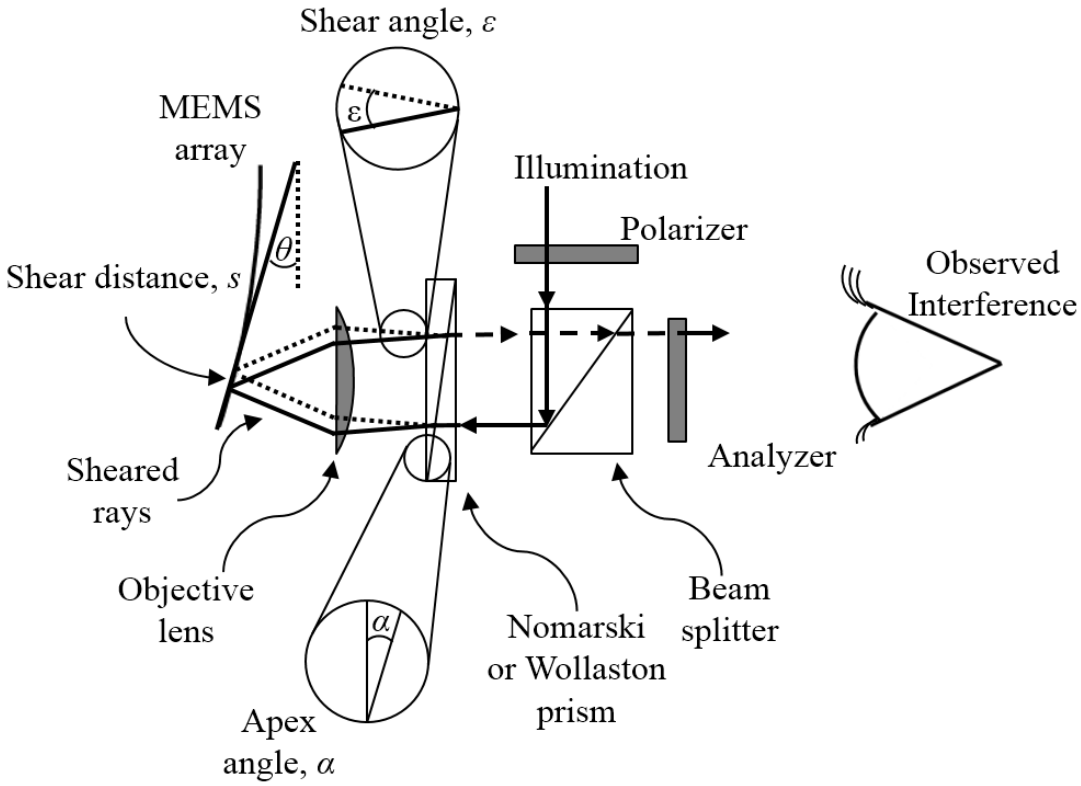

Figure 5-16. Diagram of reflected light Nomarski DIC system used as an optical readout for a MEMS based IR imaging system. The observed color difference is a function of the angle of the imaged MEMS structures.

If the MEMS structures have some angle relative to the direction of illumination, the path length from the prism to adjacent locations on the specimen will be slightly different. Here the incident and reflected light paths at the outer edges of the objective have been traced in order to avoid overlapping rays and increase clarity of the diagram; the light that travels through the center sections of the prism and objective will experience conditions close to those of parallel illumination and observation allowing straightforward determination of path length difference. The difference in path length between the two waves is then be given by

$$\Gamma = 2 \cdot s \cdot tan(\theta), \tag{5-19}$$

where *s* is the shear distance at the specimen. If the previously sheared wave fronts have experienced any difference in path length due to angled surfaces or textures on the MEMS array, interference is forced to occur when the re-aligned wave fronts pass through the analyzer. The resulting interference color that will be observed is similar to what might be observed when inspecting a birefringent crystal with thickness and birefringence such that the effect of a similar path difference is created. A depiction of the interference colors found in birefringent specimens is often referred to as a Michel-Lévy chart, as shown in Figure 5-17.

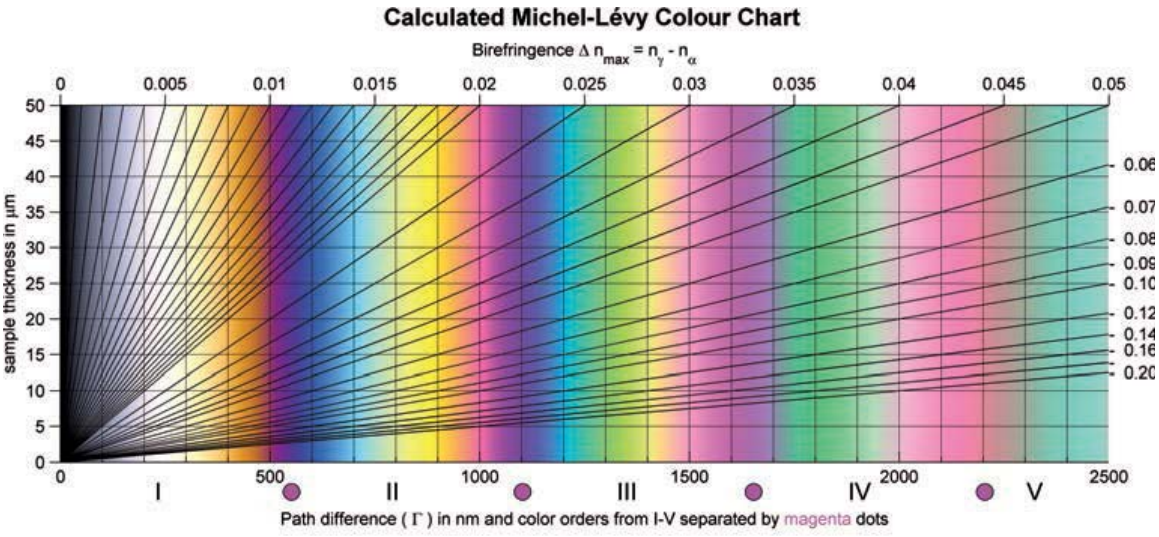

Figure 5-17. Michel-Lévy color chart which shows the interference colors as a function of optical path length difference. This is used in the investigation of birefringent mineralogical specimens [**47**].

Here the interference color and equivalent path difference for a sample of given thickness and birefringence can be found. It can be observed that with a path difference of approximately 500nm there is a significant shift in color, from orange through purple and into blue, which occurs within a relatively narrow range of path differences. This behavior can be used to create a readout system where deformation of cantilever elements in the FPA will cause a change in path difference between two sheared waves, and result in a change in the perceived color.

5.1.3. Reflectometry

When light is reflected from a specular surface (smooth relative to the wavelength of the light), it will reflect at an angle equal to the angle at which it arrived. This is shown in Figure 5-18.

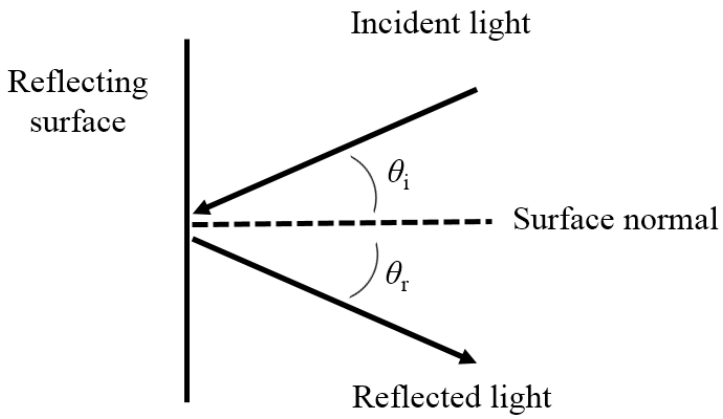

Figure 5-18. Diagram of behavior of reflected light where the angle, θ_i, of incidence is equal to the angle of reflection, θ_r.

Here the angle between the incident ray and a surface normal is known as the angle of incidence, θ_i, and is equal to the angle of reflection, θ_r, (the angle between a surface normal and the reflected ray). This behavior can be utilized to create a system where the angle of reflected light is varied due to deflection of the bi-material structures in the FPA. This will be referred to as a reflectometry readout, where the visible light is used to measure the angle of deflection of elements in the MEMS array. Figure 5-19 demonstrates this behavior, where IR radiation from a scene is focused onto the FPA, and causes thermomechanical deformation in the MEMS structures, while incident visible light is used to define a reflectometry readout.

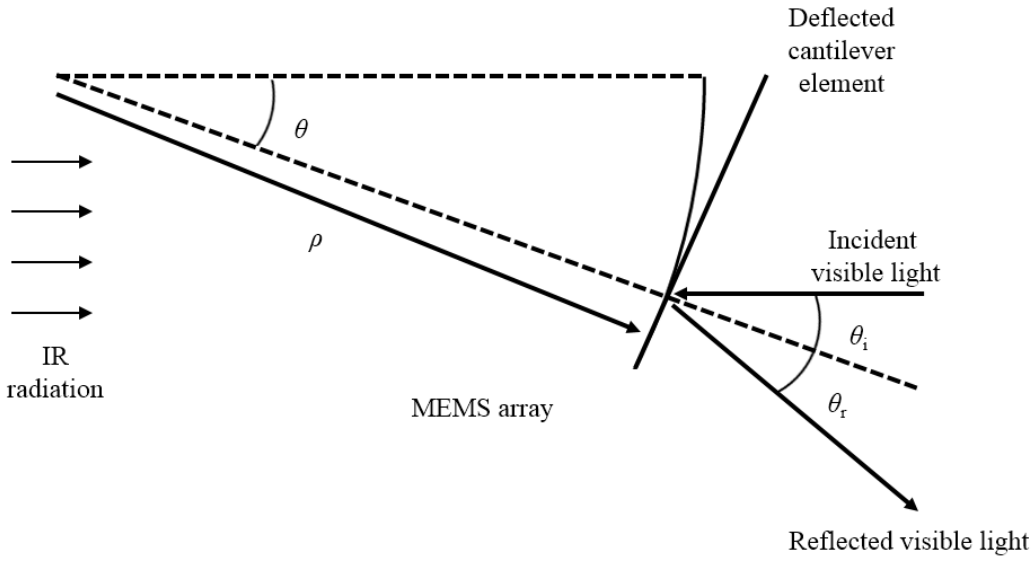

Figure 5-19. Reflectometry concept showing the angle of visible light reflection determined by the angle of a cantilever element in the FPA. Structures in the MEMS array deflect with a curvature, ρ, due to heating from IR radiation. This causes a change in the angle of reflected visible light used to image the array.

The curvature, ρ, in the legs of a cantilever element and subsequent deflection across a cantilever in the current FPA can be determined for any temperature input from the deflection equations presented in Eqs 2-4 and 2-5. Then, assuming that the visible light reflected from the array is initially incident normal to the reflector surface and that the reflector is initially flat, any change in angle of a cantilever element in the FPA will result in a change in the angle of the reflected visible light. It can be found that the angle of incidence, θ_i, and the angle of reflection, θ_r, will each be equal to the included angle of the cantilever, θ. This behavior can be used to create an arrangement where light is blocked at certain cantilever positions and not at others. This leads to a change in apparent light intensity based on the position of the structures in the MEMS array. The total angle θ encompassed by a cantilever beam can be found as

$$\theta = L * \rho, \tag{5-20}$$

where L is the total length of a cantilever element, and ρ is found using Eq. 2-4. The angle of reflected light will vary depending on the thermomechanical deformation of each cantilever element in the array. If an obstacle, such as a knife edge, is placed appropriately, it is possible to block light that is reflected at sufficiently large angles, while allowing light reflected at smaller angles to pass by unaffected, or vice versa. This is shown in Figure 5-20, where the solid trace represents light reflected at a relatively large angle (and blocked by a knife edge filter), while the dashed trace represents light reflected at a relatively small angle (which is allowed to pass by the filter).

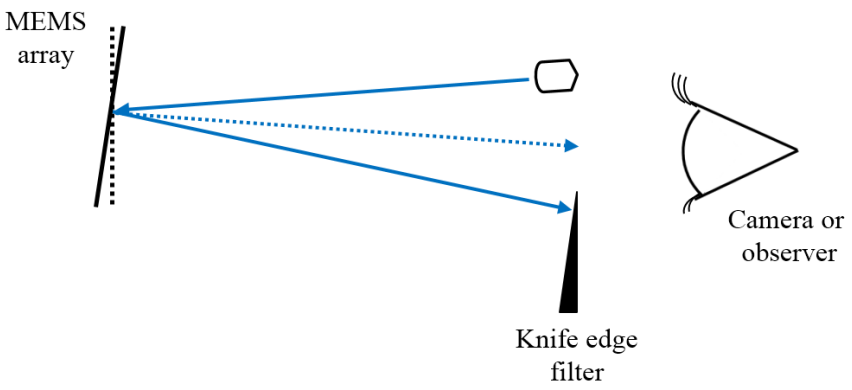

Figure 5-20. Filtering of light based on the angle of reflection. The observed intensity of the visible light used to image the MEMS array is a function of the amount of deflection of the MEMS structures in the array.

When all cantilever elements in the array are in a relaxed state, they will (ideally) act similarly to a single mirror surface and all reflect light in a similar manner. However, when such an array is used for infrared imaging, the response across the array will be dictated by the infrared radiation from the scene. While sensing the response at each pixel would then allow for the readout of the array, it is desirable to simultaneously image the entire array using a human eye or visible light camera. In order to use a single knife edge to filter the light from every cantilever in the array, lenses can be used to focus the light used in the readout.

A lens can be used to focus light from an object or source onto another plane, known as the image plane. The focal length of the lens, f, and the distance from the lens to the object, S_1, control the distance from the lens to the image plane, S_2, with this relationship defined by

$$\frac{1}{S_1}+\frac{1}{S_2}=\frac{1}{f}. \tag{5-21}$$

The deflected light readout approach uses a lens to focus the diverging light from a light source, such as an LED or an optical fiber, back to a small point, as shown in Figure 5-21 which shows the ray traces for light interacting with a lens. This setup can be thought of as creating an image of the light source, at the distance S_2 from the lens.

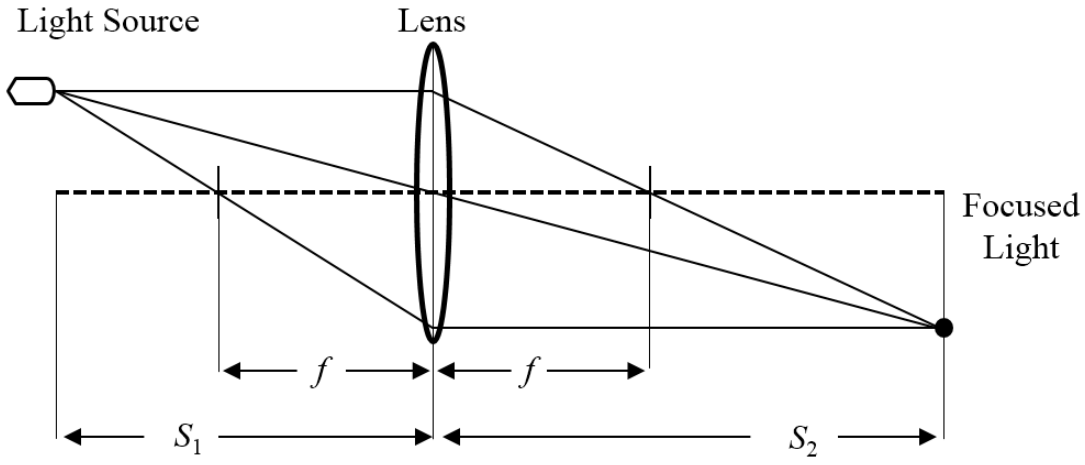

Figure 5-21. Ray trace of image formation through a lens.

If the MEMS array is then placed in the path of the light at the large diameter section of the light beam that occurs near the lens, the reflected light will cause the image of the light source to appear at a different location. The angle of the light reflected from the mirror will be equal to the angle of incidence, as shown in Figure 5-19, and the location of the image of the light source will move depending on the angle of the mirrored surface of the MEMS array. This is shown in Figure 5-22 where the MEMS array is placed such

that the illuminating light from the first lens is reflected back through a beam splitter and refocused to a small point on the lens's image plane.

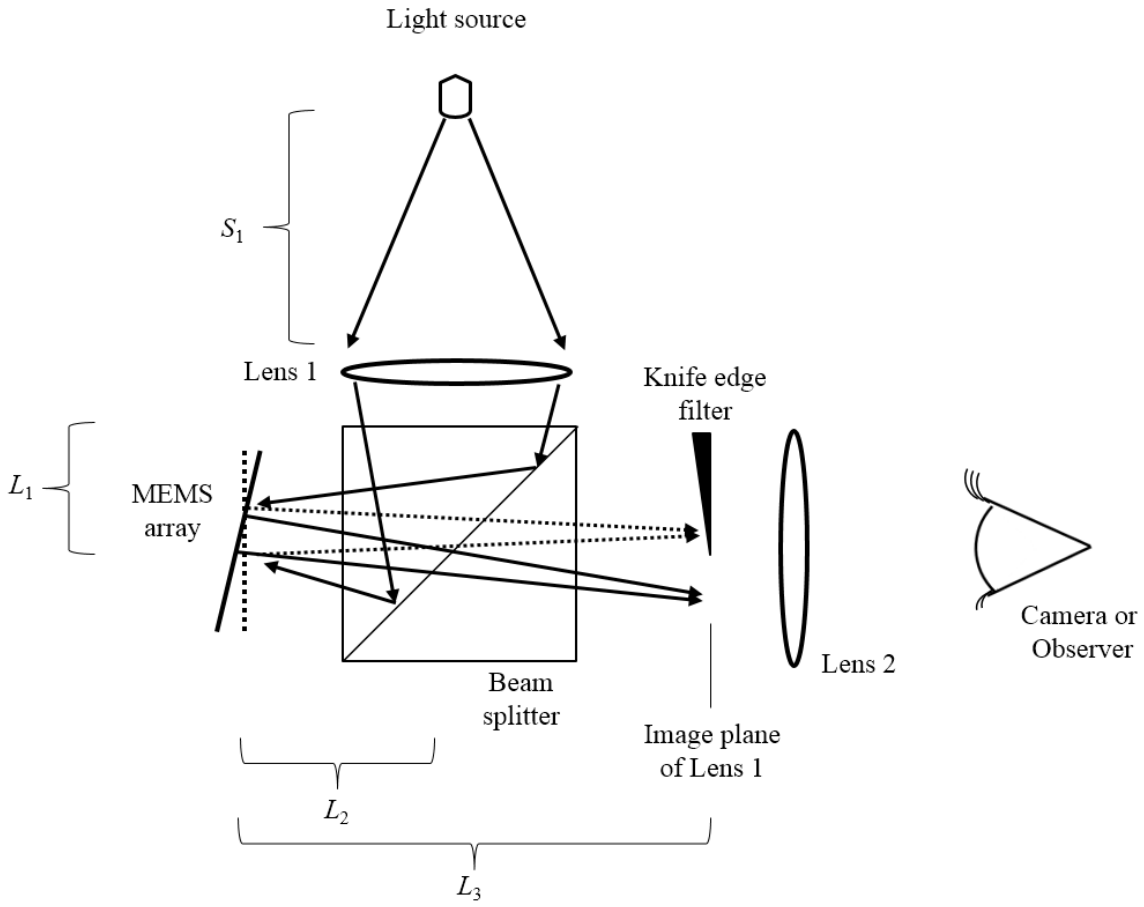

Figure 5-22. Schematic for the deflected light readout method based on filtering at the image plane of the first lens. Lens 1 is the illuminating lens used to focus an image of the light source onto the filter plane and Lens 2 is the imaging lens used by the observer to image the MEMS array.

According to Figure 5-22, the distance from the light source to the first lens is given as S_1 and the distance from the first lens to the knife edge filter, $L_1 + L_2 + L_3 = S_2$, is such that Eq. 5-21 is satisfied for the given lens focal length. Because all of the light used to

illuminate the FPA is focused to a small spot (the "image" of the light source) on the image plane of the first lens, the knife edge filter can be positioned to block light that is reflected from the FPA at a certain range of angles. If the knife edge filter is positioned to block only light reflected off of cantilever elements in a flat, or unloaded state (shown by the dashed ray traces in Figure 5-22), elements that experience deflection due to thermal loading will reflect light past the knife edge filter and into the second lens (shown by the solid ray traces in Figure 5-22). The second lens is placed such that the FPA is on the object plane and the observer is at the image plane in order to focus the light from the FPA into a camera, or onto a screen or eye for direct viewing where the illumination presented to the viewer will change as the cantilevers deflect with changes in temperature. This allows the FPA to stay in focus regardless of the angle at which light is deflected because the second lens effectively looks past the knife edge filter to maintain a clear image of the FPA.

It has been shown that when filtering on the Fourier plane using parallel illumination of the MEMS array, as presented in Figure 2-8, the sensitivity of the readout can be determined as [7]

$$\theta_{\min} = \frac{\Delta d_{\mathrm{f}}}{fN} = \frac{f\lambda/L}{fN}, \tag{5-22}$$

where Δd_{f} is the half width of the zero order spectra of a single cantilever element, f is the focal length of the lens used for both collimation and as the Fourier lens, L is the

length of the cantilever element, λ is the wavelength of light used, and N is the number of greyscale levels of the detector used to image the FPA. It has also been shown that the relationship between the observed intensity and either inclination angle of the array or temperature is linear [**7**].

In this work, the light used to illuminate the FPA is converging when it arrives at the FPA and continues to converge until it reaches the plane at which are located the knife edge filters, as shown in Figure 5-22. Thus, the spot size of the light reflected from a single cantilever can be found from

$$2\Delta d = \frac{\phi_{\mathrm{F}}}{\phi_{\mathrm{FPA}}} L, \tag{5-23}$$

where $2\Delta d$ is the diameter of the spot size at the filter plane (twice the half width of the spot), ϕ_{FPA} is the diameter of the total illumination at the FPA, and ϕ_{F} is the size of the total illumination at the filter plane. The ratio of the diameters of the illumination at the FPA and filter plane is primarily determined by the positioning and size of the focusing lens, Lens 1, but has been found to be approximately 1/5 in experimental setups used for this work. When a cantilever element deflects, the location (on the image plane of Lens 1 shown in Figure 5-22) of reflected light will then experience an excursion equal to

$$d_{\mathrm{i}} = L_3 * tan(2\theta)\,, \tag{5-24}$$

where d_i is the change in location of the reflected image of the light source, θ is the angle of the cantilever element, and L_3 is the distance from the element to the image plane of the focusing lens, as shown in Figure 5-23.

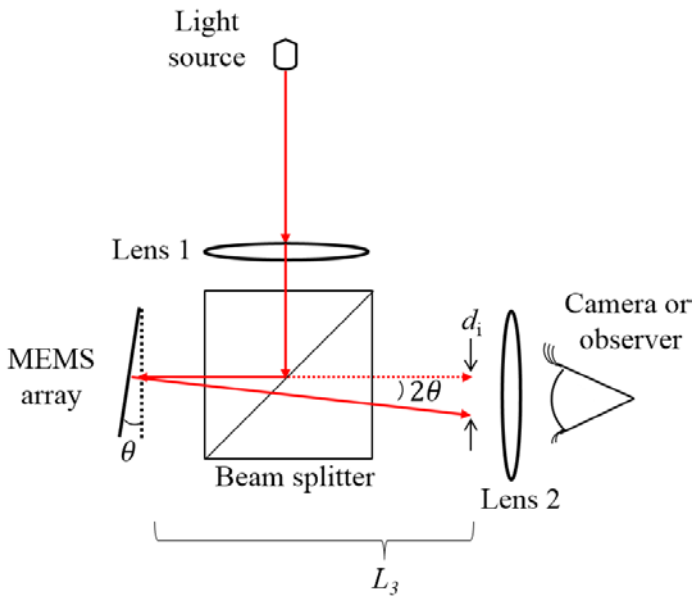

Figure 5-23. Change in location of reflected light based on the change in angle of a cantilever element of the MEMS array. The angle of reflection is twice the angle of the MEMS element.

The change in angle required to move the light from one cantilever a distance equal to its spot size (the measuring range of the readout) can then be found by combining Eqs 5-23 and 5-24 as

$$\theta_{\max} = \frac{2L\dfrac{\phi_\mathrm{F}}{\phi_\mathrm{FPA}}}{L_3}, \tag{5-25}$$

where $\theta_{\max}$ is the change in angle of the cantilever required for its reflected light to be completely blocked (or transmitted past, if it was initially blocked) the knife edge filter. This if effectively the angular measurement range. The observed changes in brightness will be highly dependent on both the distance from the array to the knife edge filter and the position of the knife edge filter, giving this system significant adjustability depending on the temperature range and sensitivity that are desired. Using representative values of 1/5 for ϕ_F/ϕ_{FPA}, 45 μm for the length of the cantilever L, and 12 cm for L_3 results in a full range sensitivity of $1.5*10^{-4}$ rad or $8.6*10^{-3}$°. The value of L_3 is largely defined by the working distance of the lens used to image the FPA, with longer working distances theoretically allowing for a more sensitive readout. If this full range sensitivity is discretized using a visible light camera, the minimum angle resolution, $\theta_{\min}$, can then be given by

$$\theta_{\min} = \frac{\theta_{\max}}{N}, \tag{5-26}$$

where N is the number of levels of a CCD or similar detector. The use of a 12bit camera will result in a theoretical angular resolution of $2.10*10^{-6}$°. This angle is an order of magnitude smaller than that reported when using Fourier plane filtering [**7**], indicating an improved resolution.

Through the introduction of a second light source, and adding a second knife edge filter, it is possible to cause light from only one source to be transmitted past the filters for a given deflection of the cantilevers in the FPA, as shown in Figure 5-24.

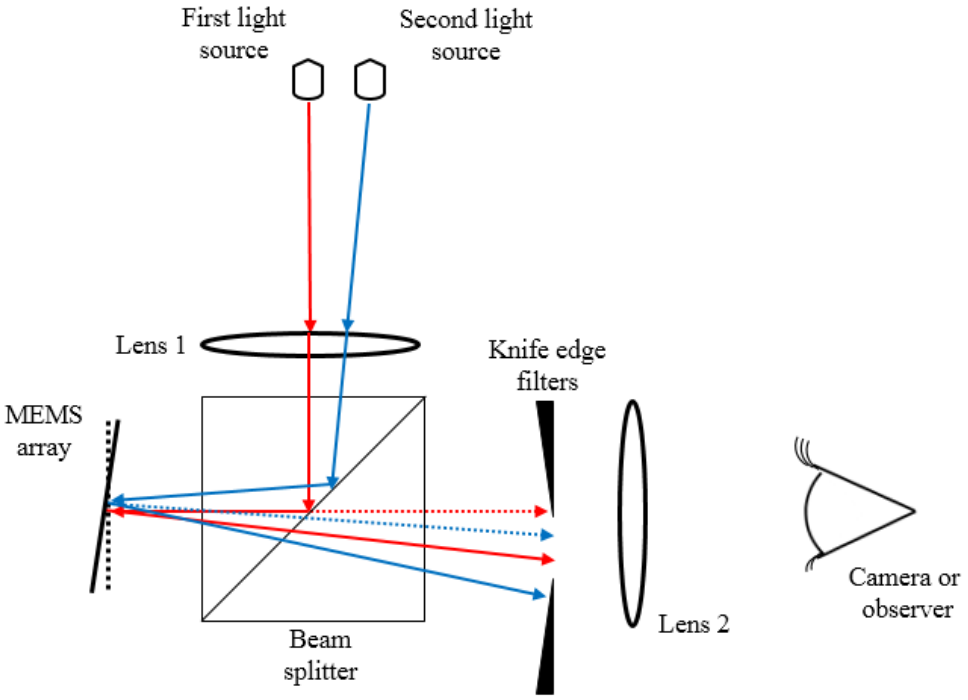

Figure 5-24. Schematic of deflected light readout using two light sources for false color image formation. Only the light from the second source is transmitted from MEMS elements in a relaxed state while only light from the first source is transmitted from MEMS elements deflected elements. The observed color is dependent on the position of elements in the MEMS array.

According to Figure 5-24, it can be observed that when the cantilever is in a relaxed (vertical) position (shown by the dashed line), light from the first source (dashed red trace) is blocked by the knife edge while light from the second source (dashed blue trace) is allowed to pass between the filters to the second lens and the observer. Then, when the

cantilever is deflected (solid line), only light from the first source (solid red trace) is allowed to pass between the filters, while light from the second source (solid blue trace) is blocked. This is of particular interest as it indicates the possibility of creating a false color readout mechanism, e.g., where cooler scenes are shown as one color (such as blue) while warmer scenes that produce more deflection of the elements of the FPA will be shown as a different color (such as red). This matches the display scheme of many modern infrared cameras that make use of electronic color displays to present temperature scales.

5.2. Evaluation of Optical Readout Mechanisms

In order to evaluate each of the readout mechanisms that were identified, it was required to determine a relationship between the temperature of a scene and the perception of an observer. The behavior of the MEMS device used has been previously characterized and the mechanical deformation as a function of temperature is known [**14**]. The interaction between each readout mechanism, the MEMS device, and the human observer then remain as areas of interest. The process used to arrive at a metric for the comparison of each readout mechanism can be divided into three general steps, as shown in Figure 5-25.

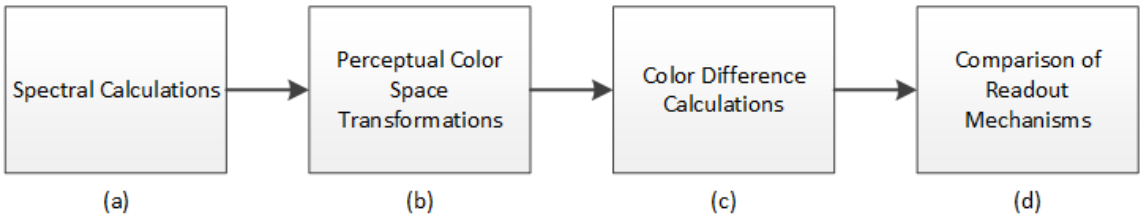

Figure 5-25. Flow chart of the process used to compare the identified readout mechanisms: (a) the spectral output from each readout is determined using analytical approaches; (b) the output is transformed into a perceptual color space using color matching functions; (c) perceptual color differences are computed using published color difference formulas; and (d) the sensitivity of each readout mechanism is compared with respect to the HVS.

According to Figure 5-25, analytical solutions for the thermomechanical behavior of the MEMS cantilever structures and the behavior of interfering and reflecting light were used to determine the relationship between the temperature of a scene and the observed spectral power distribution of the output for each readout mechanism. The spectral power distribution was then transformed into a standard human vision color space using color matching functions based on the performance of the HVS and then transformed into a perceptual color space based on the particular illumination conditions and non-uniformities of human perception. This allowed for the calculation of perceived color differences using published color difference formulas. The perceived color differences can be correlated to the performance of the MEMS device in order to achieve a system temperature sensitivity based on the perception of a human observer. A Matlab program was developed to evaluate the identified readout mechanisms and the source code is included in Appendix D, along with examples of the required data input format. The program follows the flowchart presented in Figure 5-25, beginning with spectral power

calculations and ending with the temperature sensitivity of the MEMS IR imaging system based on the color differentiation sensitivity of a human observer.

5.2.1. Spectral Power Calculations

The first step in characterizing each readout mechanism is to determine the illumination that will be used. This determines the wavelengths of light present in the system, and what relative power they will have. There are several standard illuminants that can be used to determine color appearances in daylight. However, for this work, illuminants based on the output of real light sources were used to better model the perception that would occur in the readout mechanisms considered. Illuminant wavelengths were discretized into 1nm bins ranging from 390 nm to 830 nm, for a total of 441 wavelengths, shown by

$$S(\lambda) = \begin{bmatrix} S(390\text{ nm}) \\ \vdots \\ S(830\text{ nm}) \end{bmatrix}, \tag{5-27}$$

where $S(\lambda)$ is the relative power of the illuminant at any particular wavelength. The power distribution across this range was chosen based on the individual readout mechanism and is discussed in more detail in later Sections of this work. In order to determine the amount of light at each wavelength that will be contained in the output of the readout, the interaction between the illuminating light and the MEMS array is

determined analytically, based on the illumination spectrum and the behavior of the particular readout mechanism. These data were used to create a spectral intensity matrix that describes the amount of light as a function of two variables; the first variable affecting the amount of light produced is the wavelength itself while the second variable is the temperature dependent deformation of a MEMS cantilever elements. The general case of the spectral intensity matrix, which varies according to the particular readout mechanism, is

$$I(\lambda,T)=\left\{\begin{bmatrix}L_\lambda(390\text{ nm},T_1)\\ \vdots \\ L_\lambda(830\text{ nm},T_1)\end{bmatrix},\begin{bmatrix}L_\lambda(390\text{ nm},T_2)\\ \vdots \\ L_\lambda(830\text{ nm},T_2)\end{bmatrix},\cdots\begin{bmatrix}L_\lambda(390\text{ nm},T_n)\\ \vdots \\ L_\lambda(830\text{ nm},T_n)\end{bmatrix}\right\}, \qquad (5\text{-}28)$$

where λ is the wavelength, T is the scene temperature , and $L_\lambda(\lambda,T)$ is the light intensity that depends on the specific readout mechanism used. The relative color stimulus functions can then be determined from element-by-element multiplication between the relative spectral power distribution, Eq. 5-27, and the columns of the spectral intensity matrix given in Eq. 5-28 with,

$$\emptyset(\lambda,T)=I_\lambda(\lambda,T)*S(\lambda), \qquad (5\text{-}29)$$

where $\emptyset(\lambda,T)$ is the relative spectral color stimulus function that may be perceived by an observer.

5.2.1. Transformation of Spectral Power to Human Vision Space

Color matching functions allow a spectral power distribution to be transformed into a color space based on human vision and a given set of primaries. The CMFs used for this work were based on the 2-deg XYZ CMFs transformed from the CIE (2006) 2-deg LMS cone fundamentals [**35**]. These allow the transformation into the CIE XYZ human vision color space. These are the most recent and updated CMFs available and can be obtained in 1nm increments to match the illuminants that were used [**35**]. The CMFs are given by

$$\begin{matrix}\overline{x_\lambda}(\lambda) \\ \overline{y_\lambda}(\lambda) \\ \overline{z_\lambda}(\lambda)\end{matrix} = \begin{bmatrix}\overline{x_\lambda}(390\text{ nm}) & \dots & \overline{x_\lambda}(830\text{ nm}) \\ \overline{y_\lambda}(390\text{ nm}) & \dots & \overline{y_\lambda}(830\text{ nm}) \\ \overline{z_\lambda}(390\text{ nm}) & \dots & \overline{z_\lambda}(830\text{ nm})\end{bmatrix}, \tag{5-30}$$

where $\overline{x_\lambda}(\lambda)$, $\overline{y_\lambda}(\lambda)$, and $\overline{z_\lambda}(\lambda)$ are the color matching functions as a function of wavelength for CIE XYZ color space. The CMFs used are plotted in Figure 5-26 and are included in tabular form in Appendix A.

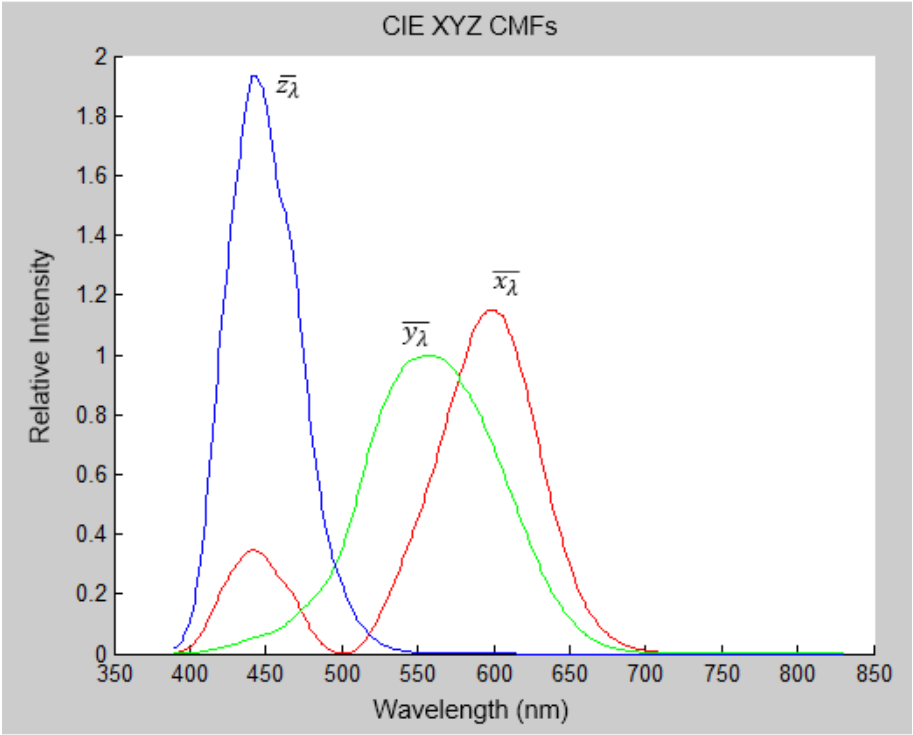

Figure 5-26. Plot of 2-deg XYZ CMFs transformed from the CIE (2006) 2-deg LMS cone fundamentals [**35**].

The spectral data representing the light output from the readout was then converted into the human vision CIE XYZ color space. This was completed using a numerical summation in the place of the integrals presented in Eqs 4-7 to 4-9 shown by

$$\begin{bmatrix} X \\ Y \\ Z \end{bmatrix} = \begin{bmatrix} k_\lambda \sum_\lambda \emptyset\,(\lambda,T)\overline{x_\lambda}(\lambda)\Delta\lambda \\ k_\lambda \sum_\lambda \emptyset\,(\lambda,T)\overline{y_\lambda}(\lambda)\Delta\lambda \\ k_\lambda \sum_\lambda \emptyset\,(\lambda,T)\overline{z_\lambda}(\lambda)\Delta\lambda \end{bmatrix} = k_\lambda \begin{bmatrix} \overline{x_\lambda} \\ \overline{y_\lambda} \\ \overline{z_\lambda} \end{bmatrix} I_\lambda(\lambda,T), \tag{5-31}$$

where *X*, *Y*, and *Z* are the tristimulus values for the primaries of the CIE XYZ color space and k_λ is the photometric constant in Eq. 4-10. The XYZ tristimulus values are now known for each temperature included in the relative spectral stimulus function shown in Eq. 5-29. These values can be transformed to the RGB color space of an electronic display in order to perform a qualitative check on the color distribution and to observe colors similar to what a readout mechanism might produce. The transformation from the XYZ color space to the RGB color space is accomplished using a linear transformation matrix that is described by the specific set of RGB primaries that will be used. In this case the sRGB color space was chosen in order to achieve good color matching across a wide range of electronic displays such as those used for many windows computers [**33**], and the required transformation matrix, M^{-1}, is [**36**]

$$M^{-1} = \begin{bmatrix} 3.2404542 & -1.5371385 & -0.4985314 \\ -0.9692660 & 0.8760108 & 0.0415560 \\ 0.0556434 & -0.2040259 & 1.0572252 \end{bmatrix}, \tag{5-32}$$

so that the conversion to the linear sRGB color space is accomplished with

$$sRGB_{\text{linear}} = \begin{bmatrix} R \\ G \\ B \end{bmatrix} = M^{-1} * \begin{bmatrix} X \\ Y \\ Z \end{bmatrix}. \tag{5-33}$$

It is important to note that the XYZ color space contains all perceivable colors, while any given RGB color space is limited to the bounds of the three primaries chosen. This range

of displayed colors is called the color gamut. In the case where colors lie outside the gamut of a particular display, they must be clipped in order to preserve the relative values of the other colors present and produce a displayed color that is close to what might be observed. Simple clipping can be accomplished by replacing any colors outside the gamut with values at the edge of the gamut, *e.g.*, one or more of the RGB primaries will remain at its maximum value for all colors outside the gamut. Gamut mapping refers to methods, other than simple clipping, of adjusting the values of the RGB primaries in order to minimize the visual effects of out of gamut colors. This is an area of ongoing research [**48**]. In this work a simple clipping strategy is implemented for out of gamut colors. Scaling may also be employed to reduce the amount of clipping necessary for a given color. This provides a more appropriate range of relative displayed colors at the expense of color accuracy. For color difference calculations it is important to maintain the accuracy of the color information used. However, for producing a qualitative output that can represent the relative colors that might be observed from a given readout, a combination of clipping and scaling is utilized.

Because the response of the eye is not linear with respect to luminance, but rather follows a logarithmic function where equal percent changes in luminance appear similar, smaller changes in luminance may be detected at lower relative luminance levels. Most cameras are designed to encode picture information similarly to that of the human eye, with more bits of data allocated to lower relative luminance. The relationship between light input to a capturing device, and the output signal often includes an encoding gamma, γ, which can be approximately given by

$$V = L_V{}^{\gamma} , \tag{5-34}$$

where L_V is the measure luminance and V is the output signal from the device. A gamma of 1/2.2 is used for the sRGB color space on windows based computers [**48**]. A plot of the sRGB encoding and decoding gamma is shown in Figure 5-27 where the decoding gamma represents the response of a standard sRGB monitor attached to a windows computer.

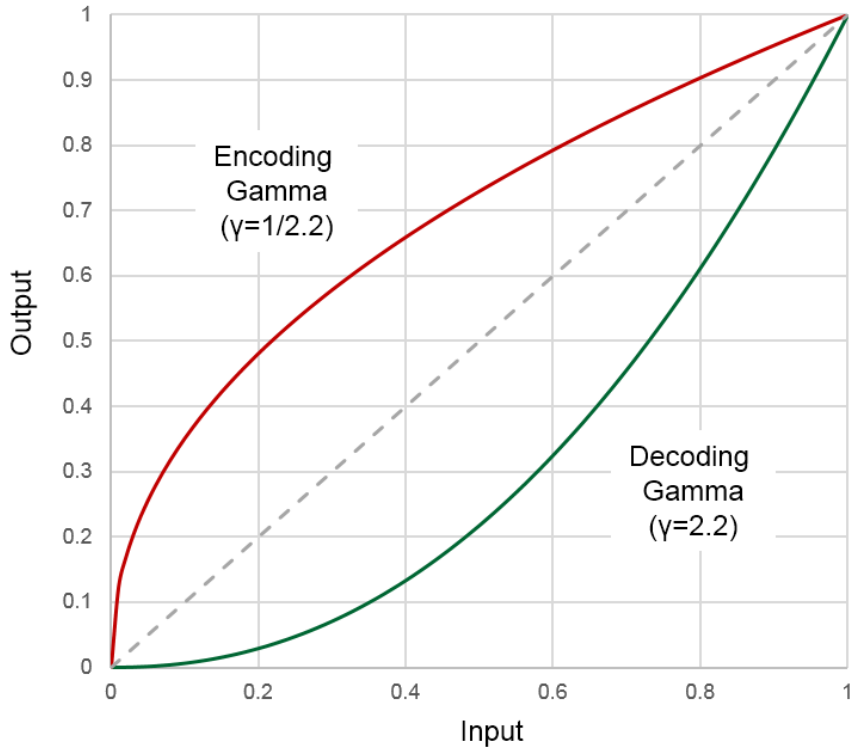

Figure 5-27. Output versus input for representative encoding and decoding gamma curves for the sRGB color space.

In order to correctly display linear levels of luminance from spectral power distributions, the image must be gamma corrected using the inverse of the decoding gamma used by the computer monitor. This gamma correction and simple clipping are simultaneously accomplished through the use of the *imadjust* function in Matlab where the level of gamma correction is manually specified. The gamma corrected image is then displayed to give a qualitative check of the output from the spectral calculations and transformation into human vision space. It is important to note that no standard computer display can accurately recreate all of the colors perceivable by the human eye, therefore the displayed RGB image will not necessarily be a precisely accurate representation of the somewhat wider gamut of colors an observer might see when directly observing the spectral output of an optical readout system.

While the CIE XYZ color space represents the entire range of human vision, it is not linearly distributed with respect to perception. It is therefore necessary to transform the XYZ color data into the CIE L*a*b* or CIELAB color space using Eqs 4-14 to 4-16. This requires the use of a reference white value to account for color adaptation and color constancy in the HVS. The reference white represents a surface that reflects or transmits all wavelengths of light equally; if illuminated by white light, it will appear white [**34**]. This is accomplished by

$$\begin{bmatrix} X_{\mathrm{n}} \\ Y_{\mathrm{n}} \\ Z_{\mathrm{n}} \end{bmatrix} = k_{\lambda} \begin{bmatrix} \overline{x_{\lambda}} \\ \overline{y_{\lambda}} \\ \overline{z_{\lambda}} \end{bmatrix} S(\lambda). \qquad (5\text{-}35)$$

where the constant k_λ ensures that the output will be scaled such that Y_n is equal to 100 [**34**]. A daylight reference white can be calculated using the spectral power distribution of the D65 standard daylight illuminant [**11**]. This allows for the calculation of colors as they would be perceived relative to daylight. The implementation of the CIE XYZ to CIELAB transformation formulas that was used in this work was obtained online from the School of Computer Science and Software Engineering at The University of Southern Australia [**49**].

5.2.2. Color Difference Calculations

The implementation of the CIEDE2000 color difference formula is computationally intensive and will not be described fully here and more details can be found in [**50**]. In brief, it includes many correction factors to rotate and adjust the CIELAB color space such that perceptually uniform color difference calculations can be achieved [**50**]. The specific Matlab implementation used for this work was obtained online from the School of Engineering & Applied Sciences, Electrical & Computer Engineering Department, University of Rochester and can be found in Appendix C [**51**]. Briefly, a pair of L*a*b* data triplets are supplied to the CIEDE2000 function, and the color difference between them is returned as value of delta E. In theory, a delta E of 1 is equal to the threshold of color difference perception. However, in practice it has been found that the 50% acceptability threshold for color difference in practical applications is approximately 2 [**52**]. In this work, a CIEDE2000 delta E of 2.0 is used as a representation of the smallest change in color is noticeable. Each readout mechanism is evaluated based on the

temperature change required produce an equivalent change in output. This leads to the just noticeable temperature change for each readout mechanism and gives a criteria for the selection of the most suitable readout mechanism.

5.2.3. Analytical Evaluation of Holographic Readout

The holographic readout mechanism utilizes interference between a live wavefront reflected from the FPA and a holographically recorded wavefront of the FPA in a reference state. Any changes in the position of the cantilever elements of the FPA will result in a change in the relative phase of the two wavefronts, and the resulting interference can be observed as a change in brightness. The deformation of the elements of the FPA has been previously characterized as a function of scene temperature [**14**]. The intensity as a function of illuminating wavelength and scene temperature is then given by

$$I(\lambda, T) = I_{\mathrm{o}} + I_{\mathrm{r}} + 2\sqrt{I_{\mathrm{o}} I_{\mathrm{r}}} \cos\left[\frac{4\pi}{\lambda} D(T) + \pi\right], \tag{5-36}$$

where λ is a particular wavelength of illumination and $D(T)$ is the thermomechanical deformation of the elements of the FPA previously found to be 1.5 nm/K [**14**]. A half-wave plate can be added to the optical path of one of the wavefronts in order to produce a phase difference of π radians and destructive interference, which is observed as a dark scene, in areas that do not experience deformation [**53**]. The intensity matrix, given in

Eq. 5-28, is then calculated, for the desired ranges of wavelength and temperature, and used in Eq. 5-29 together with information for the spectral power of a light source to determine the spectral color stimulus function. For these purposes, the spectral output of a ThorLabs M617-L2 light source is used to define the relative illumination of the light source, $S(\lambda)$ [**54**]. The calculated spectral color stimulus function includes variations between darkness and bright red (the color of the light source), as a function of wavelength and scene temperature, with brighter areas corresponding to wavelength and temperature combinations that produce constructive interference and darker areas corresponding to wavelength and temperature combinations that produce destructive interference. In order to determine the human perception that will be produced by the spectral power distributions contained in the columns of the spectral color stimulus function, the spectral power distribution for each temperature is transformed into the CIE XYZ human vision color space using the CIE XYZ CMFs, which were transformed from the CIE (2006) LMS cone fundamentals, with Eq. 5-31 and the photometric constant, k_λ, computed with Eq. 4-10. The data in the CIE XYZ color space is then converted into the sRGB color space for electronic displays by application of the corresponding transformation, as described in Eq. 5-33. The transformation into the sRGB color space is required in order for the data to be presented on a standard electronic computer display. The sRGB data are gamma corrected by the application of Eq. 5-34 so that the intensity is accurately displayed by the gamma decoding of a standard computer display and these gamma corrected sRGB data were displayed for use as a qualitative intermediate check of the perceptual color space transformations and observation of the relative color output

that could be expected from the optical readout mechanism. Afterwards, the XYZ data are transformed into the CIELAB color space by application of Eqs 5-14 to 5-16. The CIELAB color space is more perceptually uniform than the CIE XYZ color space and allows for color comparisons and the calculation of perceptual color differences. The X, Y, and, Z values for the D65 daylight reference white, calculated with Eq. 5-35, are used in the CIE XYZ to CIELAB transformation in order to determine the colors perceived relative to daylight. Finally, in order to relate these data to the color differentiation sensitivity of the HVS, color differences are calculated by applying the CIEDE 2000 color difference formulas described in [**50**] and implemented using the CIEDE2000 Matlab function included in Appendix C. The sRGB representation of the interference colors that could be expected based on the previously defined light source and thermomechanical behavior of a MEMS cantilever structure across a temperature range of 0 °C to 400 °C is shown in Figure 5-28.

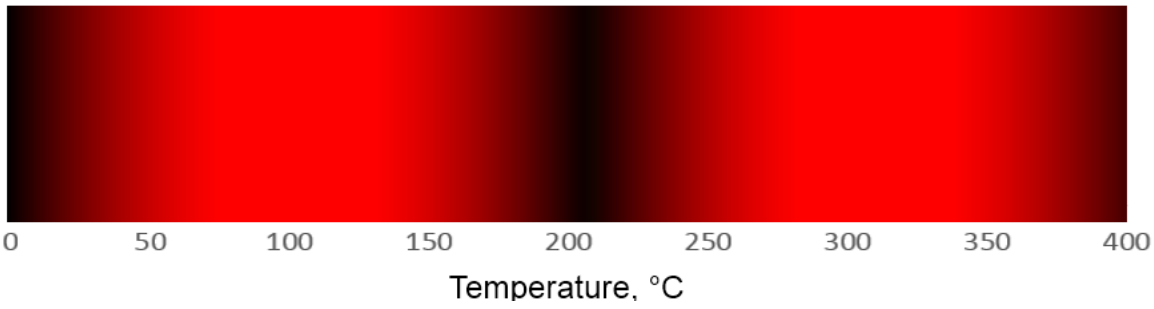

Figure 5-28. Simulated interference colors for holographic readout based on temperature range of 0 °C to 400 °C.

The simulated interference colors shown in Figure 5-28 have been scaled and clipped to fit inside the color gamut of a standard electronic display. The combination of scaling and clipping provides a more accurate representation of the relative colors and brightness that could be expected. Contrary to the sRGB data that were used for a qualitative check with a standard electronic display, the data used for perceptual color difference calculations were not scaled or clipped in order to preserve their quantitative nature. Every color in the calculated output can be compared to other colors through the use of color difference calculations that provide a measure of the perceived color difference as value of delta E. A CIEDE2000 delta E of 2.0 is approximately equal to the threshold of color difference that is noticeable in practical applications and smaller values of delta E will be indistinguishable in these applications [**52**]. The calculated color differences can be used to achieve a quantitative relationship between the output from the holographic readout and the perception of a human observer. The temperature sensitivity, with respect to human perception, of an IR imaging system based on a holographic readout can be determined from the calculated color differences. A representative result is shown in Figure 5-29, which presents the increase in scene temperature required, at every point in the temperature measuring range, for the output from the readout to produce a change in color equivalent to a noticeable color difference (delta E of 2.0).

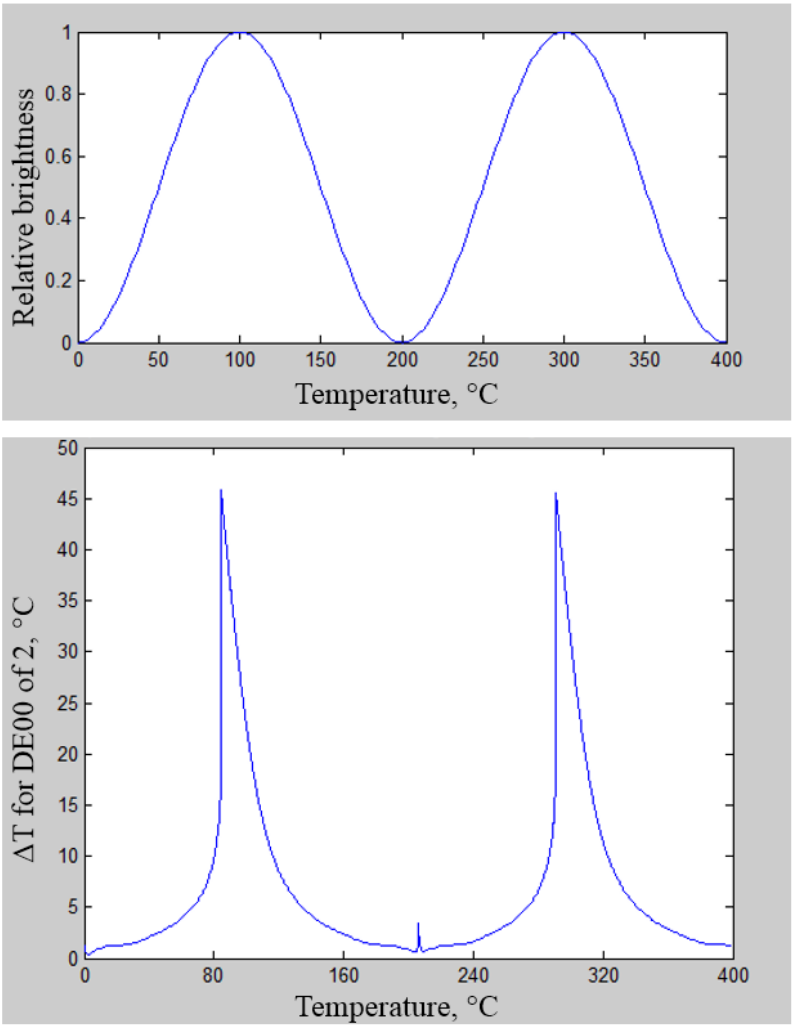

Figure 5-29. Relative brightness and noticeable change in temperature versus scene temperature for a holographic readout. The twin peaks are a result of phase wrapping where the interfering waves have the same relative phase. The relative brightness, plotted on for the same temperature range, is shown above the temperature sensitivity.

From the simulated output, it can be observed that the holographic readout will experience phase wrapping inside the selected temperature range. This will cause certain, significantly different, temperatures to become indistinguishable and is one drawback of this readout. It can be observed that the holographic readout is more sensitive in the

darker areas where there is significant destructive interference between the two wavefronts. The temperature change corresponding to a noticeable change in color is much larger near the areas of higher relative brightness, resulting in decreased sensitivity. The result of phase wrapping can be seen by the formation of two perceptually identical temperature regions, highlighted by the twin peaks in Figure 5-29.

5.2.4. Preliminary Results Using Holographic Readout

Preliminary results using a holographic readout were achieved using a self-developing photopolymer hologram and an optical setup similar to that shown in Figure 5-8. The photopolymer hologram can be developed in-situ and does not require any wet processing. The laser source used to record and reconstruct the live hologram had a wavelength of approximately 630 nm (red) and a power of 15 mW. The hologram was recorded with the MEMS array in a reference state and live interference patterns were observed during reconstruction. This system was able to produce live thermal images of a scene. A representative thermal image produced by the holographic readout system, captured using a monochromatic camera, is shown in Figure 5-30.

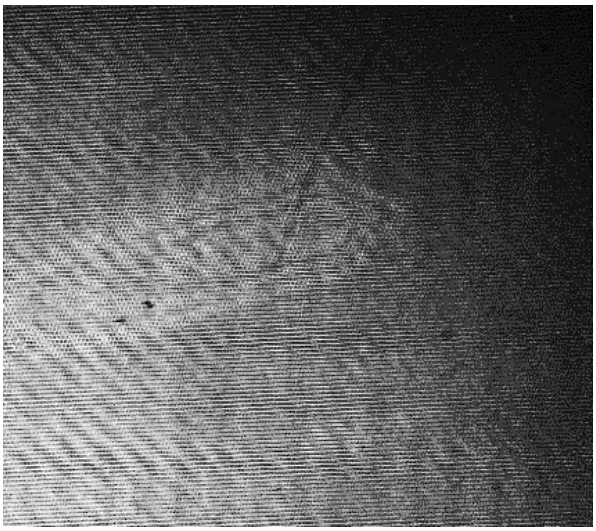

Figure 5-30. Preliminary result of a holographic readout based on a photopolymer hologram showing a live thermal image of a soldering iron at approximately 400 °C. Significant laser speckle noise is apparent and phase wrapping can be observed as concentric fringes across the surface of the hot iron.

The thermal source shown in Figure 5-30 is a soldering iron with a temperature of approximately 400 °C and phase wrapping can be observed as the concentric bands across the heated surface of the iron. The laser speckle noise in the image is substantial, and the contrast is lower than desired. While the system was able to image high temperature scenes, such as a heated soldering iron, lower temperature scenes such as a human hand produced no noticeable change in output. Preliminary results also were previously achieved by other members of the WPI-ME/CHSLT group through the use of conventional silver-halide holograms which displayed similar speckle noise and low contrast as shown in Figure 5-31 [**42**].

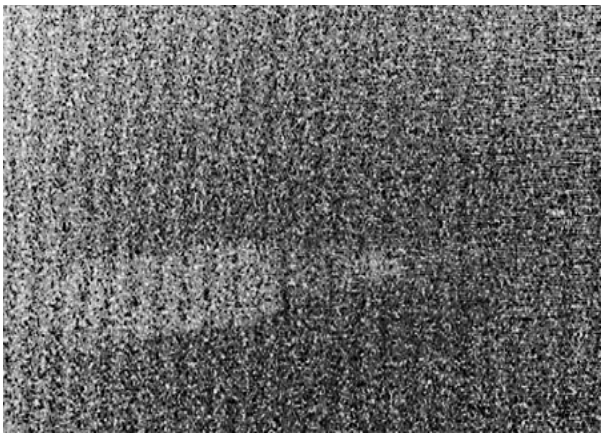

Figure 5-31. Thermal image of a soldering iron at approximately 350 °C captured using an optical readout based on a silver-halide hologram [**42**]. The image displays significant laser speckle noise as well as lower than desired contrast between the iron and background.

5.2.5. Analytical Evaluation of Nomarski DIC Readout

The Nomarski differential interference contrast (DIC) based readout uses interference between sheared and recombined white light waves in order to produce a wide range of colors. When the sheared waves are reflected from adjacent locations on the FPA, they will experience a relative optical path difference, depending on the angle of the reflecting surface, which will result in a phase difference and interference when the waves are recombined and observed through a polarizing filter. The evaluation of the Nomarski DIC based readout follows a process similar to that of the evaluation of the Holographic readout. However, there are several differences between the two. While holography uses a single color light source with a relatively narrow emission spectrum, Nomarski DIC is based on interference in broadband light. The range of interference colors that can be produced from this illumination are similar to those shown in the Michel-Levy chart

shown in Figure 5-17. These can be calculated using the intensity equation for Nomarski DIC interference as a function of wavelength and relative optical path length using Eq. 5-18 along with the spectral power distribution of the light source, and following the procedure presented for generating the qualitative interference colors in the holographic readout. For the simulation of the Nomarski DIC readout, the D65 standard illuminant, which represents the power spectrum of a representative light source with a color temperature of approximately 6500 K, is used to define the relative spectral illumination, $S(\lambda)$, in order to provide a perceptually white light source that contains radiation across the entire visible range. The calculated interference colors for relative path differences ranging from 0 nm to 1500 nm are shown in Figure 5-32 where the calculated colors have been gamma corrected and clipped to fit inside the sRGB color space in order to be displayed on a standard computer monitor.

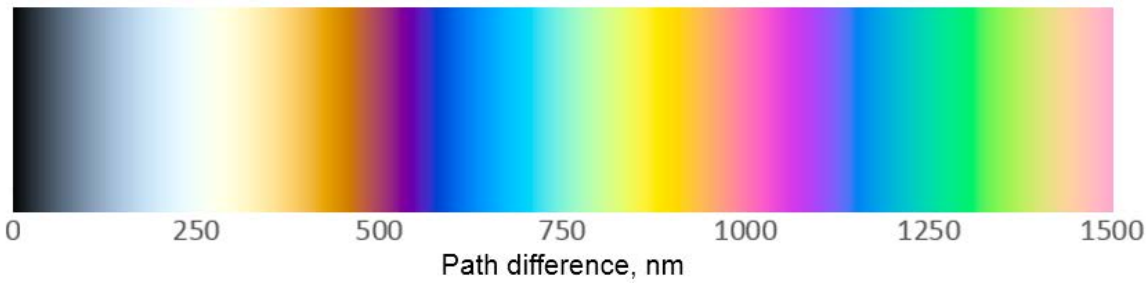

Figure 5-32. Calculated interference colors versus path difference for Nomarski DIC system.

Because the color formation in a Nomarski DIC system is a function of the relative path difference between the two sheared waves, and an additional path difference can be added using one or more of several methods described previously, it is useful to

determine the path difference range that will produce the range of colors inside which the HVS is most sensitive to changes in color. The interference colors are most intense at small path length differences, and become less saturated at larger path differences due to the loss of coherence between the sheared waves of white light. Therefore, the range of interference colors shown in Figure 5-32 will include the most significant color gradients of the entire range of possible relative path differences and a Nomarski DIC readout will be most sensitive when operated in a subsection of the range shown. Using a procedure similar to the color difference calculations that were performed for the evaluation of the holographic readout, the relative color differentiation sensitivity of an observer can be determined across the range of calculated interference colors for the Nomarski DIC readout. The relative change in path difference required for a noticeable change in color is shown in Figure 5-33.

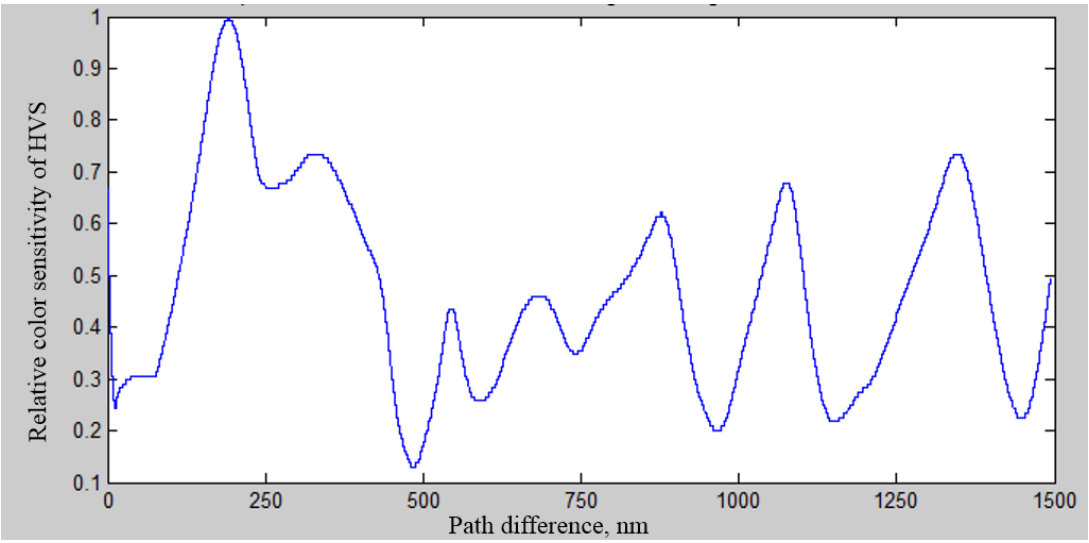

Figure 5-33. Relative color sensitivity of the HVS to changes in relative path difference in a Nomarski DIC system. This was calculated using the CIEDE2000 color difference formulas and the color range depicted in Figure 5-32.

According to Figure 5-33, the range of relative path differences inside which a human observer is most sensitive to changes in relative path difference is the orange-purple-blue region, shown in Figure 5-32, that occurs around relative path differences of approximately 500 nm; the highest sensitivity is at a relative path difference of 485 nm. This is the initial relative path difference that will provide the greatest readout sensitivity, based on the perception of a human observer. The orientation of the FPA can also be adjusted to achieve a specific direction of color shift with increasing temperature, depending on the direction of deflection of the MEMS structures relative to the sheared waves of the Nomarski DIC readout. The use of a path difference of 530 nm, along with the FPA arranged such that the relative path difference decreases as temperature increases, allows for a natural color map that starts in the sensitive blue-purple region at 530 nm and shifts towards orange as the temperature increases.

Using the known temperature-dependent behavior of the elements of the FPA, the angle of a cantilever element as a function of temperature, $\theta(T)$, is found by combining Eqs 2-4 and 2-6. The resulting path difference as a function of cantilever angle, $\Gamma(\theta)$, arises from the subsequent combination of Eq. 5-19 with the angle of the cantilever as a function of temperature. A realistic shear distance of 1.0 μm [**55**] is used for the separation, at the FPA, of the sheared waves. Finally, the relative intensity as a function of illuminating wavelength and temperature is

$$I(\lambda, T) = \sin^2\left[\frac{180° \, \Gamma(\theta(T))}{\lambda}\right]. \qquad (5\text{-}37)$$

The intensity matrix, given in Eq. 5-28, is then calculated, for the desired ranges of wavelength and temperature, and used in Eq. 5-29, together with information for the spectral power of the light source, to determine the spectral color stimulus function. The interference colors for a given temperature range, shown in Figure 5-34, can be determined from the relative spectral color stimulus function using a procedure similar to that used for holography.

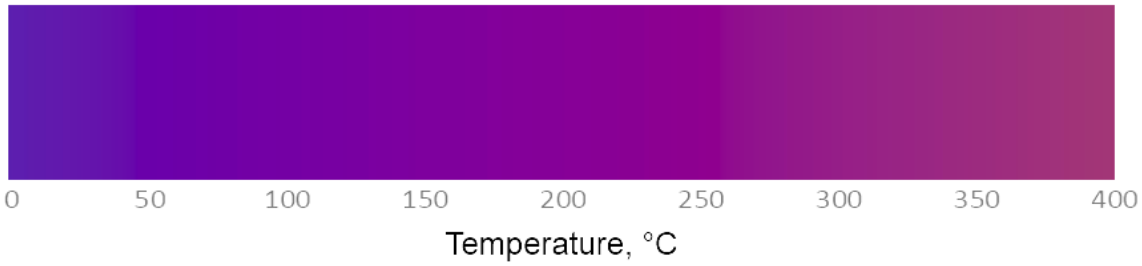

Figure 5-34. Simulated interference colors for Nomarski DIC based readout for a temperature range of 0 °C to 400 °C. The image shown here has been enhanced for display and visualization purposes due to low contrast in the original.

The temperature sensitivity of the Nomarski DIC readout, based on a human observer, is shown Figure 5-35 and can be calculated from the color differences in the CIELAB color space, similar to for the holographic readout evaluation.

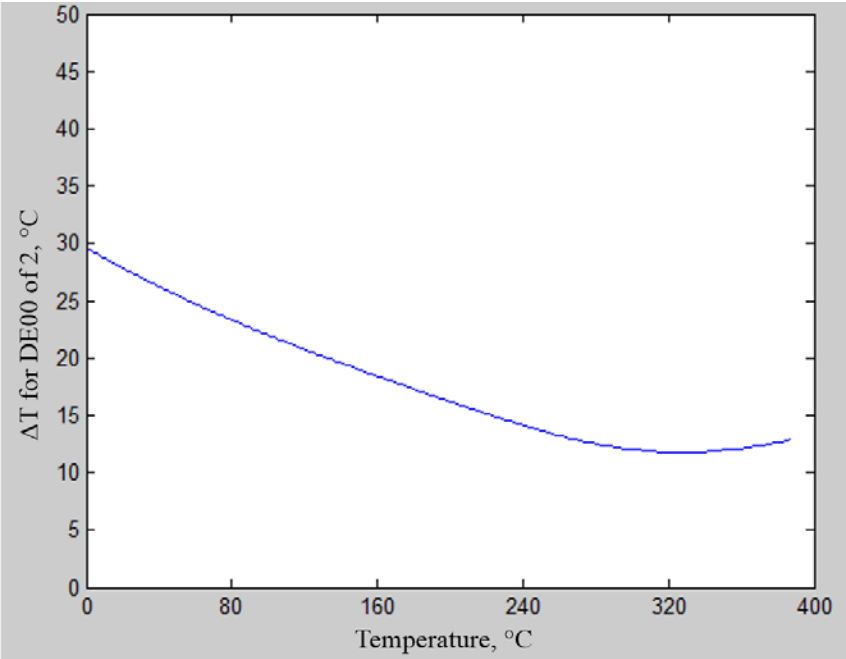

Figure 5-35. Noticeable change in temperature versus scene temperature for a Nomarski DIC readout with an initial path difference of 530 nm, the area of maximum color sensitivity according to Figure 5-33.

The initial path difference, selected to achieve the maximum color sensitivity, can be adjusted to achieve a specific starting color. The sensitivity of the Nomarski DIC readout system is highly dependent on the initial relative path difference and the shear distance between the two waves at the FPA; the results shown in Figure 5-35 are based on a realistic path shear similar that encountered in a Nomarski DIC microscope system. The color shift is small across the temperature range shown, however the transition between colors is relatively smooth and gradual which suggests that a Nomarski DIC based readout could offer consistent sensitivity across the measuring range. However, while the system sensitivity is relatively linear compared to the holographic readout, the minimum temperature sensitivity is approximately 12 °C. This is less sensitive than the dark

regions of the holographic readout range but more sensitive than the bright regions of the holographic readout range. This suggests that the Nomarski DIC readout has a moderate sensitivity when combined with a realistic shear distance and the responsivity of the current FPA.

5.2.6. Preliminary Result Using Nomarski DIC readout

Preliminary investigations of a Nomarski DIC readout were performed on two arrays (the packaged array described previously as well as an unpackaged MEMS array) using two Toolmakers microscopes (a Nikon Eclipse MA200 and a Nikon Measurescope MM-11) both with Nomarski DIC capabilities, objectives with different magnifications, and halogen illumination sources.

Due to the constraints imposed by the optical systems used and the dimensions of the packaged MEMS array, preliminary imaging with Nomarski DIC was only achievable with the unpackaged MEMS array. The unpackaged array was heated by placing a hot soldering iron in close proximity to the array in order to produce deformations of the bimaterial structures and images were recording using a color sensitive visible light camera. A comparison of several structures in the array in relaxed and heated states is shown in Figure 5-36.

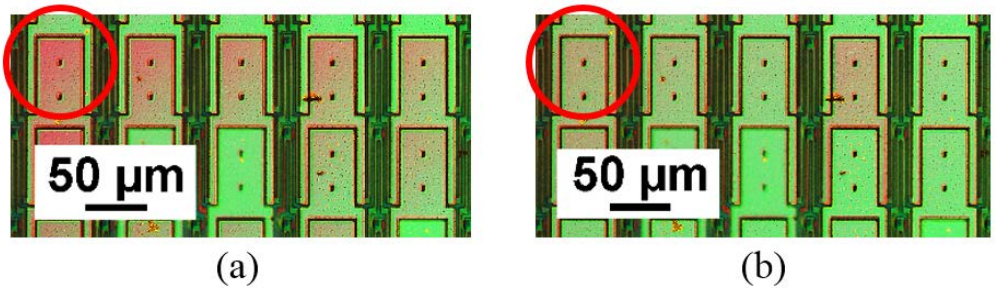

Figure 5-36. Preliminary results of Nomarski DIC readout comparing: (a) elements of MEMS array at room temperature; and (b) the same elements heated by a soldering iron held close to the array. The highlighted areas shows a structure that exhibited noticeable color change as a function of array temperature.

While the color formation is significant on some structures, other structures did not exhibit any noticeable change in color for the applied thermal load. This shows that the deformations of the MEMS device are small compared to the measuring sensitivity of the Nomarski DIC system and, according to the analytical evaluations, the Nomarski DIC readout will not be suitable for use in a direct view thermal IR imaging system. It is also possible that the cover glass used on the MEMS package affected the spatial and/or phase relationship between the sheared light waves and reduced the observed color formation.

5.2.7. Analytical Evaluation of Reflectometry Readout

The reflectometry based system produces perceivable changes in output by reflecting light either towards or away from an observer based on the temperature-dependent position of the elements of the MEMS array. By configuring this mechanism as shown in Figure 5-24, two light sources at slightly different positions can be used such that, as the elements of the FPA deflect, light from one source is directed towards an observer while

light from the second source is blocked from view and this behavior is then reversed when the elements of the FPA relax to their original position. Any color of light source may be used and a false color imaging system (where the output color changes as a function of scene temperature) can be achieve through the use of two differently colored light sources. For the evaluation of the reflectometry readout, the first light source was defined with dominant wavelengths in the red region and the second source contained dominant wavelengths in the blue region. These light sources were chosen such that they could produce a natural color map that would be easily recognizable; cooler temperatures could be shown as blue while warmer temperatures could be displayed as red and temperatures between the two extremes will produce a mix of the two colors and appear as different shades of purple and pink. In order to achieve realistic simulated results, the spectral power distributions for two commercially available LED light sources were used. The relative spectral illumination of the first source, $S_1(\lambda)$, was based on the spectral output of a ThorLabs M617-L2 mounted high-power LED while the relative spectral illumination of the second source, $S_2(\lambda)$, was defined by the spectral power distribution of a ThorLabs M455-L2 mounted high-power LED. These light sources have emission peaks at 617 nm and 455 nm and appear bright red and blue, respectively. In order to determine the colors that might be observed from a reflectometry readout based on these two light sources, the amount of light transmitted from each source as a function of temperature is then required.

The total light intensity output from the reflectometry readout is determined by the combination of light from the two spectral light sources, $S_1(\lambda)$ and $S_2(\lambda)$, modulated by

the filtering elements in the readout. The modulation of the light transmitted from each source is a function of the angle of a cantilever element as a function of temperature, $\theta(T)$, from the combination of Eqs 2-4 and 2-6, relative to the angular measuring range of the readout, $\theta_{\max}$, given by Eq. 5-25. If the system is assembled as shown in Figure 5-24, so that light from only the second source is transmitted from cantilevers in a relaxed state and light transmission from the first source begins when cantilever elements deform, the relative color stimulus function for the calculation of the total output from the readout as a function of temperature and wavelength is then given by Eq. 5-38.

$$\emptyset(\lambda,T)=\begin{cases}\left[1-\dfrac{\theta(T)}{\theta_{\max}}\right]S_2(\lambda)+\left[\dfrac{\theta(T)}{\theta_{\max}}\right]S_1(\lambda)\,, & \theta(T)<\theta_{\max}\,,\\ \left[1-\dfrac{\theta(T)-\theta_{\max}}{\theta_{\max}}\right]S_1(\lambda)\,, & \theta_{\max}\le\theta(T)<2\theta_{\max}\,,\\ 0\,, & 2\theta_{\max}\le\theta(T)\,.\end{cases} \tag{5-38}$$

According to Eq. 5-38, as the temperature of the elements of the MEMS array increase, the light transmitted from the first source will increase while light from the second source will decrease, until the angle of the cantilever reaches the angular measuring range of the system, $\theta_{\max}$, where only light from the first source will be transmitted. If the cantilever angle increases further, the light transmitted from the first source will decrease until the cantilever angle reaches an angle equal to $2\theta_{\max}$ after which no light will be transmitted. The change in the amount of each light that is transmitted from each source will produce change in the observed brightness and the change in the relative amounts of light

transmitted from each source will produce a perceived change in perceived color. Together, the changes in perceived brightness and color provide the method of communicating thermal information about the scene.

While the theoretical angular measuring range, $\theta_{\max}$, for a reflectometry readout is defined by Eq. 5-25 for a given illumination and filtering arrangement, it has been found experimentally that a practically achievable system shows nearly complete blocking/transmission of light from a single source across an angular measuring range, $\theta_{\max}$, of approximately 26.7 mrad. This is the measuring range that will be used in order to evaluate the performance of a practically achievable reflectometry readout. The relative spectral color stimulus function given by Eq. 5-38 can then be used similarly to those calculated for the Nomarski DIC and holographic readouts in order to evaluate the performance of the readout mechanism with respect to the perception of a human observer. The transformations from spectral power to the CIE XYZ perceptual color space and then to the sRGB color space are accomplished similarly to the evaluation of the Nomarski DIC and holographic readouts and representative colors of the spectral power distribution across the given temperature range for the reflectometry readout are shown in Figure 5-37. The data presented in Figure 5-37 have been gamma corrected and scaled to fit inside the gamut of a standard electronic display, similarly to what was done for the evaluation of the Nomarski DIC readout and holographic readouts.

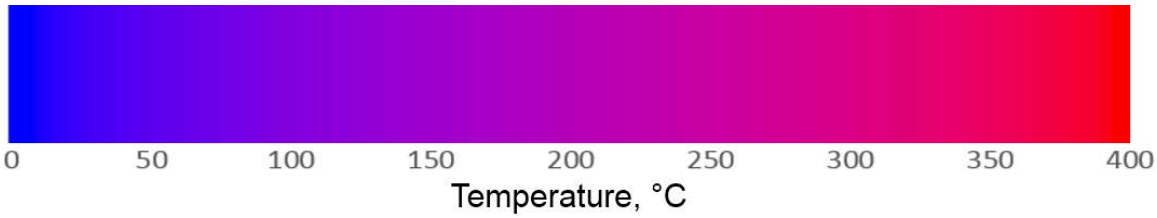

Figure 5-37. Simulated interference colors for two color reflectometry readout based on temperature range of 0 °C to 400 °C. The colors shown have been scaled and clipped to fit inside the color gamut of a standard electronic display.

The transformation from the CIE XYZ color space to the CIELAB color space was again performed using the D65 white point in order to produce colors relative to daylight which could then be used to determine perceptual color differences across the given color range. Color differences were calculated similarly to the other readouts evaluated, and the human vision temperature sensitivity of an IR imaging system based on the reflectometry readout is shown in Figure 5-38.

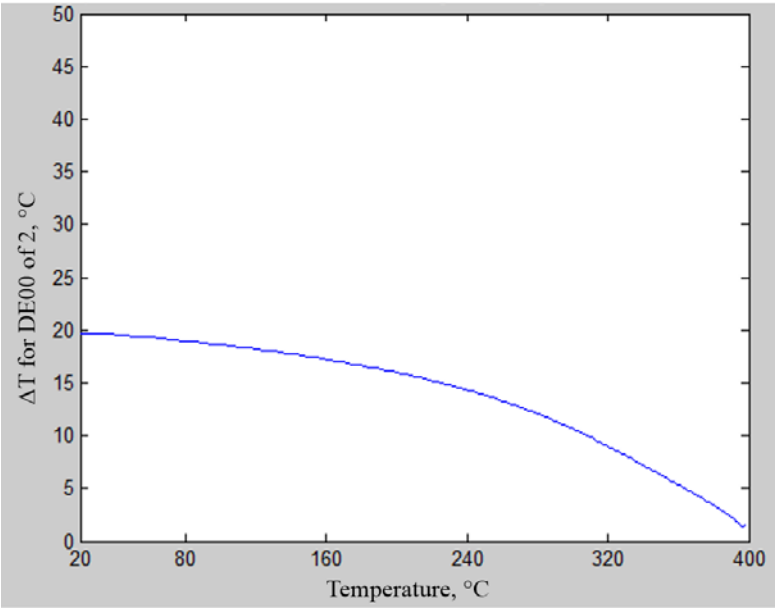

Figure 5-38. Noticeable change in temperature versus scene temperature for a two color reflectometry readout.

The reflectometry readout offers relatively linear sensitivity across the entire measuring range compared to the Nomarski DIC readout, and a wide range of colors can be observed. The color map is dependent on the light sources chosen and can be varied independently of the temperature range while the sensitivity of the system is dependent on the geometry of the optical setup and the arrangement of the knife edge filter elements. According to Figure 5-38, the reflectometry system temperature sensitivity is higher than that observed for the Nomarski DIC readout, and significantly more consistent across the measuring range when compared to the holographic readout.

5.2.8. Preliminary Results Using Reflectometry Readout

Preliminary results for the reflectometry readout were achieved using a setup similar to that shown in Figure 5-24. Two light sources, with relative power spectra similar to those used in the analytical evaluation of the reflectometry readout, were used for illumination along with a soldering iron operating at a temperature of approximately 400 °C. The reflectometry readout produced live thermal images of the hot soldering iron that could be observed with the naked eye. The output of the reflectometry system was captured using a color sensitive visible light camera and a representative IR image is shown in Figure 5-39.

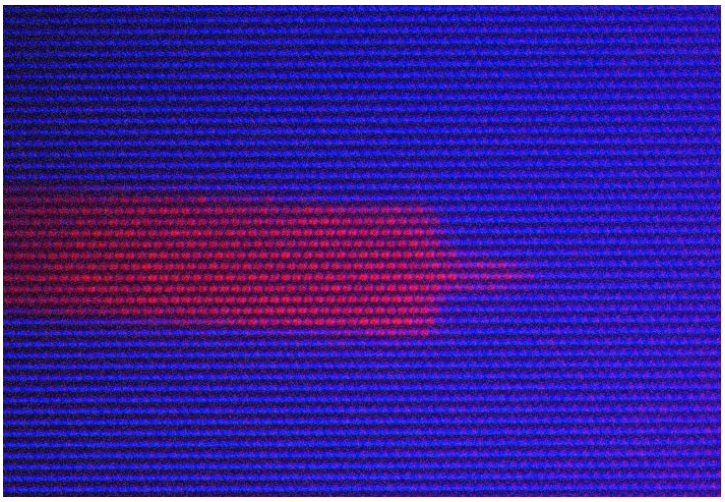

Figure 5-39. Representative result of reflectometry readout showing color formation when imaging a soldering iron with a temperature of approximately 400 °C. This image of the directly observable output was captured using a color sensitive visible light camera.

The reflectometry readout showed strong color formation for high temperature scenes such as a soldering iron however, the readout did not appear to be sensitive to low temperature objects such as a human hand or face. The system does not rely on interferometry or coherent light, and was observed to be less sensitive to vibration when compared to the holographic readout. The reflectometry system offers significant adjustability in terms of color map flexibility.

5.3. Selection of Readout Technique

Based on the perception of the HVS, the range of expected output colors and resulting temperature sensitivity of each readout can be used to compare the performance of the identified optical readout mechanisms and determine the readout that is most suitable for

use in a direct viewer. Preliminary experimental results also provide insight into the performance that could be expected from a realized IR imaging system based on each readout mechanism. Evaluation of the holographic readout showed that phase wrapping will occur inside the temperature range that was evaluated, and preliminary results showed a high level of undesirable background noise in the generated holographic thermal images. Because the holographic readout is based on interferometry, it is also very sensitive to relative motion and vibration in the optical components of the system; small vibrations were observed to have significant deleterious effects on the quality of the live IR images that were produced. This would cause significant challenges in future work towards system portability and ruggedization. While the Nomarski DIC readout is also based on interferometry, the small separation between the optical paths makes the system less sensitive to vibration. However, the Nomarski system is relatively complicated and preliminary results showed low sensitivity compared to the holographic and reflectometry readouts. Also, the range of color formation in the Nomarski DIC readout is limited to the range of interference colors of the light source used. Finally, the reflectometry readout offered the most flexibility in arrangement and color range as any colors of light sources may be used. The reflectometry readout is not based on interferometry, and consequently was observed to be less sensitive to system vibration and relative component motion however, the precise alignment of the optical components and filtering system must be maintained for proper operation. The reflectometry readout offers consistent sensitivity across a given measuring range. Based on the analytical evaluation of the three readouts presented, along with the preliminary results presented

for each system, the reflectometry readout was chosen as the readout mechanism most suited for the development of a direct viewer. Table 5-1 includes a summary of the advantages and disadvantages, for each system, which were considered in the selection of the readout mechanism that was chosen for further development of an IR direct viewer.

Table 5-1. Summary of advantages and disadvantages of the optical readout systems that were considered for the development of a direct view IR imaging system.

Readout	Advantages	Disadvantages
Live holography	• Quantitative • Good sensitivity in dark regions • Only shows changes between reference and live state	• Subject to fringe wrapping • Inconsistent sensitivity • Sensitive to vibration • Difficult ruggedization • Requires coherent light
Nomarski DIC	• Wide range of possible colors from one source • Does not require coherent light • Consistent sensitivity	• Complicated physical system • Relatively low sensitivity • Limited color range • Difficult miniaturization
Reflectometry	• Does not required coherent light • Consistent sensitivity • Unlimited range of color maps • Potential for miniaturization • Relatively insensitive to vibration • Potential for ruggedization • Flexible/adaptable arrangement	• Qualitative output • Requires multiple light sources for false color map

According to Table 5-1, the reflectometry readout offers many advantages and significant potential for the current development of a direct view IR imaging system, and future work towards a portable, hand-held IR imager for applications where conventional IR imagers are not suitable.

6. Development of a Reflectometry Readout

There are a number of considerations that need to be accounted for in order for the successful development of a direct view IR imaging system. The output from the system should be directly observable with the HVS or a visible light camera, and changes in output corresponding to changes in scene temperature should be perceivable. The viewable area of the FPA should be sufficiently large that the resulting image will contain an adequate number of cantilever elements in order to display an IR image of a scene with sufficient spatial resolution. The range of output from the system will determine the temperature imaging range and the change in output for a given change in temperature will determine the temperature sensitivity of the IR imaging system. The output from the readout should be observed directly, either through projection into the eye or onto a screen, in practically achievable levels of ambient lighting. The incorporation of these considerations for the development of a direct viewer started by considering the optical setup that was developed for the preliminary investigation of the reflectometry readout, shown in Figure 5-24. The optical setup that was then developed for the evaluation of a reflectometry based IR direct viewer is shown in Figure 6-1.

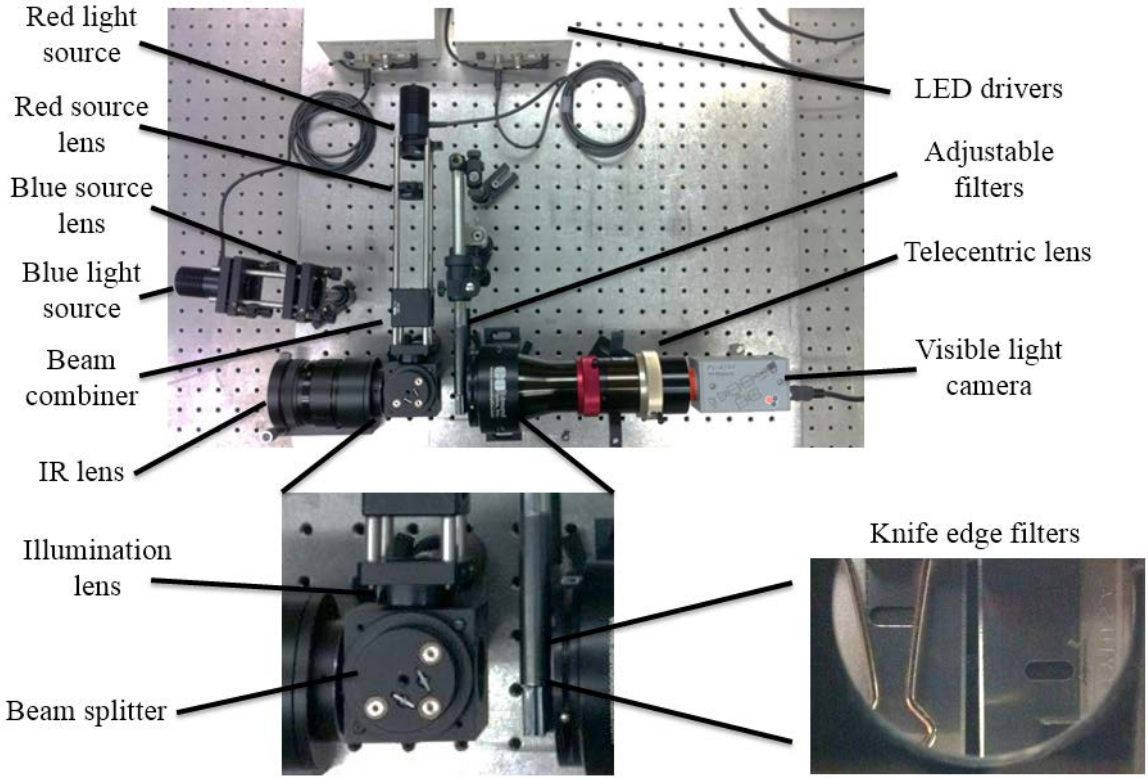

Figure 6-1. The constructed infrared imaging system based on a reflectometry readout, showing the configuration of the individual components. This setup is based on the schematic shown in Figure 5-24.

The setup shown in Figure 6-1 is based on a two color reflectometry readout, and utilized a second beam splitter as a beam combiner in order to combine the light from the two illumination sources. The light from the sources was directed towards the beam combining cube and images of the light sources were focused onto the plane of the adjustable knife edge filter elements using the illumination lens. The aperture of the IR lens was kept fully open in order to maximize the amount of IR radiation that was focused onto the FPA and the focus of the IR lens was manually adjusted based on the distance to the objects that were imaged. The IR lens and FPA were mounted on a two

axis tilt stage so that pitch and yaw could be adjusted in order to align the optical system. The knife edge filters were mounted to individual adjustable linear stages so that they could be easily adjusted and an aperture was placed in front of each light source in order to increase the system sensitivity by limiting the area from which light is emitted and reducing the corresponding size of the images of the light sources that were focused onto the filter plane. Finally, a visible light camera was used to capture the output from the system. Each of the specific components that were used in the system that was developed were considered based on particular parameters that were identified.

6.1. System Components

6.1.1. Visible Light Camera

In order to capture the output from the readout system, two different visible light cameras were used. The first camera was a monochrome AVT Pike F100B that was used to interface with previously developed custom software that was modified to work with the requirements of the current system. This camera has a resolution of 1000 × 1000 pixels with 7.4 μm square pixels and is sensitive from approximately 350 nm to beyond 800 nm, covering the entire visible range, with a sensitivity peak at 515 nm [**56**]. The camera communicates with a computer via a FireWire interface, and attaches to a lens via a standard C-mount. In order to observe the color output from the reflectometry readout that was developed, a color sensitive camera was required. The second camera used was

a PixeLINK PL-A782 which is a color sensitive camera that has a resolution of 2208 × 3000 with 3.5 μm square pixels for a total sensor size of 7.78 mm × 10.55 mm. This camera is sensitive from 400 nm to 1000 nm which covers the range of illumination that could be perceived by the HVS [**57**]. The camera communicates with a computer via a FireWire interface, and attaches to a lens via a standard C-mount. This camera was used as a stand-in for the human vision system (HVS) and allowed for the recording of the color output from the reflectometry based IR imaging system that was developed.

6.1.2. Camera Lens

A 1.0X telecentric lens was used to focus light reflected from the FPA onto the CCD of either of the visible light cameras that were used. The telecentric lens provides constant magnification and field of view, regardless of the position of the object or working distance. This lens is focusable and has a working distance of 98 mm to 123 mm which provides adequate space for other necessary readout optics to be placed between the lens and the FPA. The lens has an aperture range of f/6 to f/25 however the aperture was kept fully open to provide the most light to the cameras used. The lens's depth of field is 0.6 mm which is sufficient to image the current FPA and the lens features a broadband antireflective coating with a range of 425 nm to 675 nm, nearly the entire visible spectrum [**58**]. The lens features a C-mount that will interface with the camera used.

6.1.3. Beam splitters

Two beam splitters were used in the system that was constructed; one to combine the two illumination sources into a single beam, and the second to allow illuminating and reflecting light to travel parallel paths to and from the MEMS FPA. The beam splitters used are made of cemented optical wedges that allow 50% of incident light to pass while reflecting the other 50% of the light. If the illuminating light is incident normal to the outer surface of the beam splitter, the reflected light will exit at an angle of 90°. The beam splitters are made from the same N-BK7 material as the illumination lens and additionally have anti-reflective coatings on their outer surfaces in order to improve efficiency and reduce erroneous reflections [**59**].

6.1.4. Lenses

The lenses used for directing the illuminating light are ThorLabs 1 in mounted lenses, made from N-BK7 material, which mount using SM-compatible threads [**60**]. These lenses provide greater than 90% transmission for all wavelengths in the visible range and are suitable for focusing the illuminating light in order to create an image of the light source on the filtering plane of the system. Here three lenses are used: one in front of each light source to collect light and direct it towards the beam combiner, and a third to focus the image of the light sources onto the filter plane. The two light sources were placed inside the focal distance of the respective lens used to direct light towards the prism used to combine the beams; the lens for the first source had a focal distance of

50 mm and the source was placed at a distance of 45 mm while the lens for the second source had a focal distance of 75 mm and the source was placed at a distance of 70 mm. By placing the light sources inside the focal distance of the their respective lens, diverging light exits the source lenses, similarly to the light exiting the light source, but at a tighter angle than from the light source alone. This ensured that the image of the light source was not at the focal point of the illumination lens, where the Fourier spectra of the light sources exist, and that the filtering was performed on the image plane of the illumination lens as opposed to on the Fourier spectra. The illuminating lens had a focal length of 150 mm and was placed between the beam combiner and the beam splitter. The optical path distance from the illumination lens through the beam splitter and to the filtering plane was approximately 260 mm. Finally, the positions of the light sources and their respective lenses relative to the imaging lens were adjusted to focus the images of the light sources onto the filter plane.

6.1.5. Light Sources and Drivers

Current controlled, high power mounted LED light sources were used to provide illumination for the optical readout. ThorLabs DC2100 constant current drivers were used to provide consistent driving current with an accuracy of ±20 mA. These drivers can provide up to 2 A of driving current, and are sufficient to power the light sources used [**61**]. The two light sources used are the ThorLabs M455L2 and M617L2 which are high-power, mounted LED light sources that can each be driven by up to 1600 mA and include integrated and optimized heat management to provide stable output, as well as

internal threads for integration with other optical components. The M455L2 has a nominal wavelength of 455 nm and appears royal blue with a full-width, half-max of 20 nm. The M617L2 has a nominal wavelength of 617 nm, a full width half max of 16 nm, and appears red-orange [**62**]. These light sources are considered incoherent, and both provided sufficient power for use in a direct viewer. The colors were chosen to provide the desired blue-red color map for the false color IR imaging system.

6.1.6. Filters

The knife edge filter used are straight blade razors. These provide a sharp edge that can be used to effectively filter the light in the readout mechanism. The filters are placed on adjustable mounts so that they can be positioned accurately in the path of the light traveling from the MEMS array to the imaging lens and camera or observer. The filters are adjusted to match the approximate size of the image of the light sources, and positioned such that, when the MEMS array is in a relaxed state, the image of the first light source is just at the edge of the filter element while light from the second source is fully transmitted. The gap between the two filter elements is shown in Figure 6-1 and was approximately 1.5 mm.

6.2. Setup of Direct Viewer

In order to realize a direct viewer, light must be projected out of the readout system and either into the eye of an observer or onto a screen to create an image that could be

directly observed. The camera and associated lens were therefore removed from the reflectometry system and an imaging lens and screen were used in their place in order to project a thermal image onto a screen that could be directly observed with the naked eye. The experimental setup that was used to achieve a live projected image from a false color IR direct viewer based on a reflectometry readout is shown in Figure 6-2.

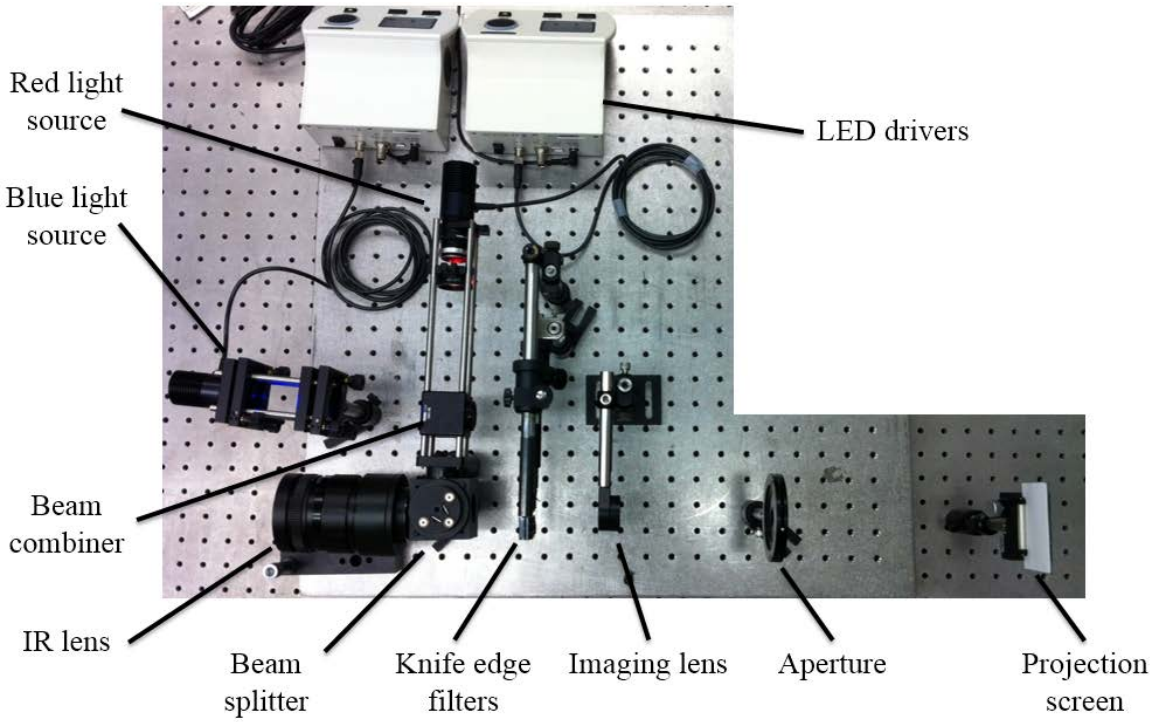

Figure 6-2. The constructed false color direct view infrared imaging system based on a reflectometry readout. This system uses and imaging lens, aperture, and screen in order to project directly observable IR images.

For the setup shown in Figure 6-2, light that passes through the knife edge filters is focused by the imaging lens in order to create an image on the projection screen. The imaging lens has a focal length of 125 mm and is placed approximately 187 mm from the

FPA. The projected image is focused at a distance of approximately 375 mm from the imaging lens, with a magnification of approximately 2x. This magnification produces an image of sufficient size to be viewed by the naked eye, while preserving sufficient brightness for the image to be observed in low to moderate ambient lighting conditions. The aperture between the imaging lens and screen serves to limit the projected image to only the active area of the FPA that is illuminated by both light sources. This area contains approximately 50 × 50 cantilever elements, for a total resolution of 2,500 MEMS structures. The field of view is approximately 8 inches in diameter at an object distance of 16 inches. For other magnifications and fields of view, the imaging optics, light sources, and arrangement could be modified accordingly.

6.3. Demonstration of Direct Viewer: Camera as Observer

When using two colored light sources and the PL-A782 color sensitive visible light camera, the system demonstrated false color infrared imaging without the use of any computer processing other than to directly display the output from the camera. The reflectometry system was used to image a scene with a spiral heating element at a temperature of approximately 300 °C along with a soldering iron at a temperature of approximately 400 °C. A sequence of live thermal images captured using the reflectometry based direct view system is shown in Figure 6-3. Next, a sequence of thermal images was captured, for a scene consisting of a coiled heating element at approximately 300 °C and human hand at approximately 30 °C, as shown in Figure 6-4.

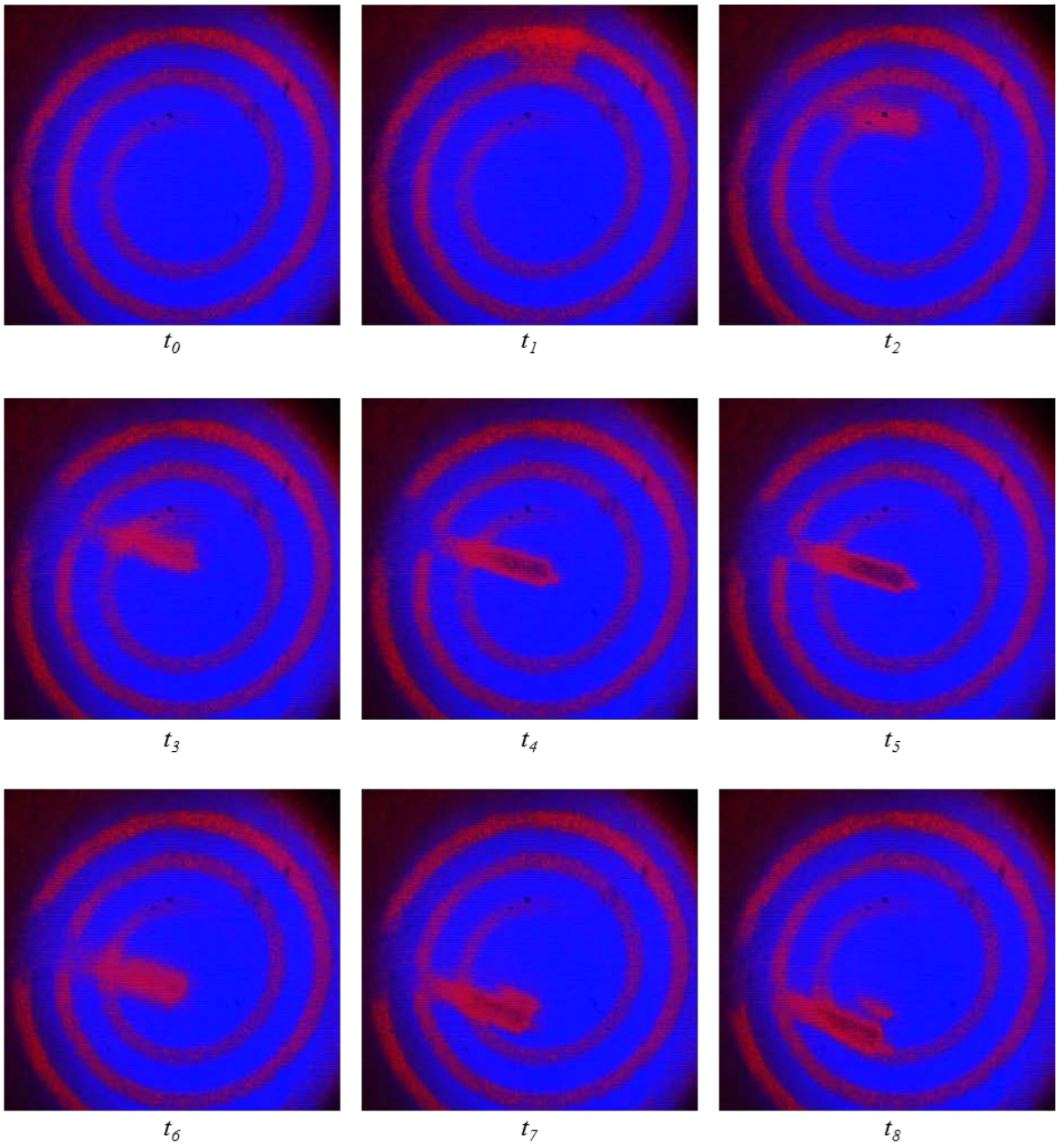

Figure 6-3. A sequence of thermal images captured, at times t_i, using the reflectometry based direct view system. A coil heating element at a temperature of approximately 300 °C is visible at t_0 and a soldering iron with a temperature of approximately 400 °C enters the scene from above at $t_1 - t_3$. The center of the soldering iron appears dark when it remains stationary at t_4 and t_5, this shows that the corresponding MEMS structures experience angular deformation greater than the measuring range of the system, $\theta_{\max}$, described in Section 5.1.3. The reflection of IR radiation from the soldering iron can be seen near the center of the scene at t_7 and t_8.

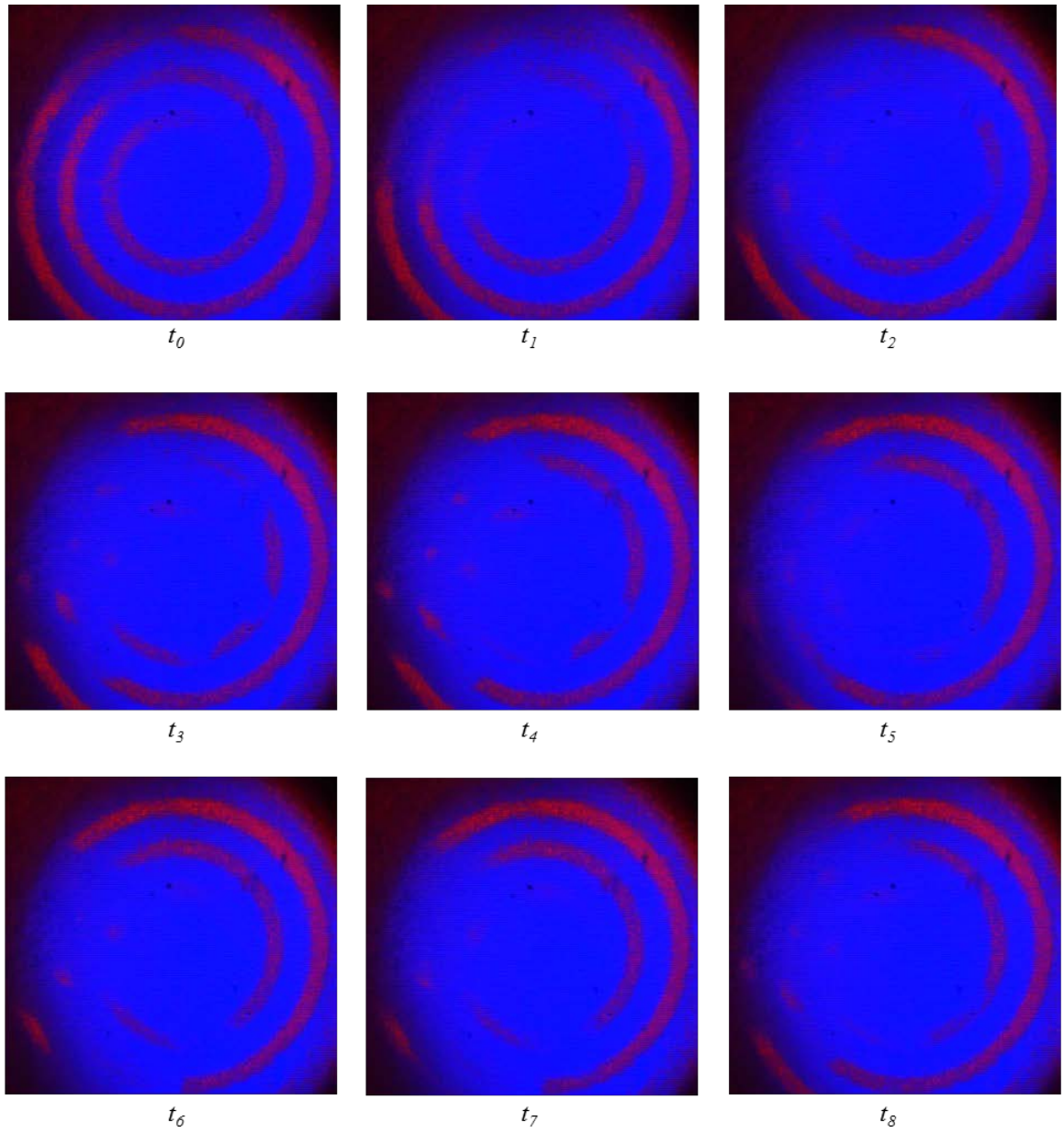

Figure 6-4. Sequence of thermal images captured, at times t_i, directly using the false color direct viewer based on the reflectometry readout. The heating coil at approximately 300 °C is visible at t_0 and a hand with a temperature of approximately 30 °C enters the scene from above at $t_1 - t_3$. The outline of the hand is visible against the coil in the background at t_4 however, the IR radiation from hand itself does not produce a significant change in color.

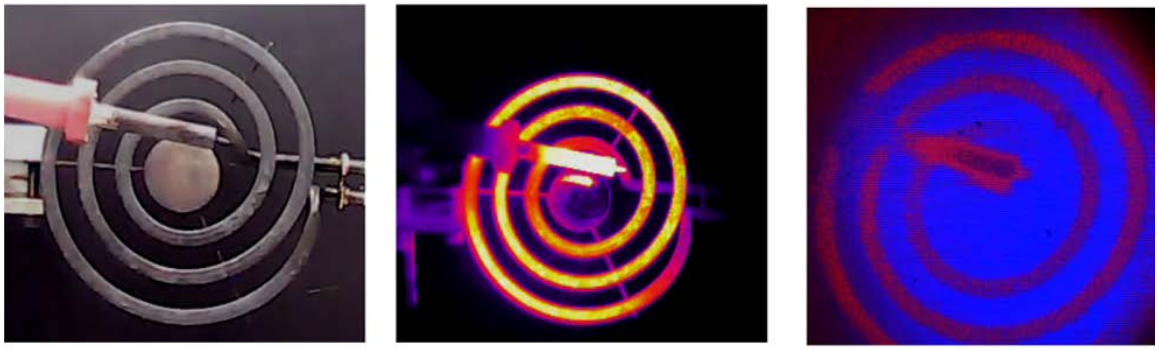

(a) (b) (c)

Figure 6-5. Comparison of: (a) visible light; (b) commercial thermal camera; and (c) false color MEMS IR imaging system. No computer processing was used with the MEMS IR imaging system.

The output from the MEMS based system was compared with a visible light camera and commercial thermal camera as shown in Figure 6-5. Here it can be observed that the MEMS system exhibits strong color formation due to infrared radiation from both the heating element and the soldering iron. However, the MEMS system was not as sensitive to lower temperature objects such as a human hand, as shown again in Figure 6-6, which is a comparison of the visible light, commercial thermal, and MEMS false color direct view thermal images of a hand and coiled heating element.

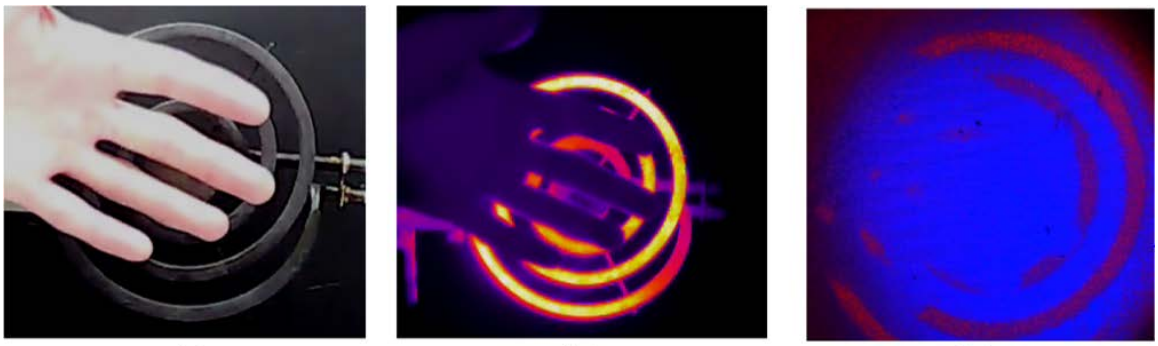

Figure 6-6. Comparison of (a) visible light, (b) commercial thermal camera, and (c) false color MEMS IR imaging system. A human hand was visible against the backdrop of a heating coil.

According to Figure 6-6, a hand was clearly visible against the backdrop of the heating element, but the infrared radiation from the hand itself is not sufficient to produce a significant color change relative to the background ambient temperature. The next step was the demonstration of the thermal image projection capabilities of the developed false color IR direct viewing system.

6.4. Demonstration of Direct Viewer

Another perspective of the constructed direct view IR imaging setup, shown from above in Figure 6-2, which shows the arrangement of the system, including the relative location of several imaged heat sources, is shown in Figure 6-7.

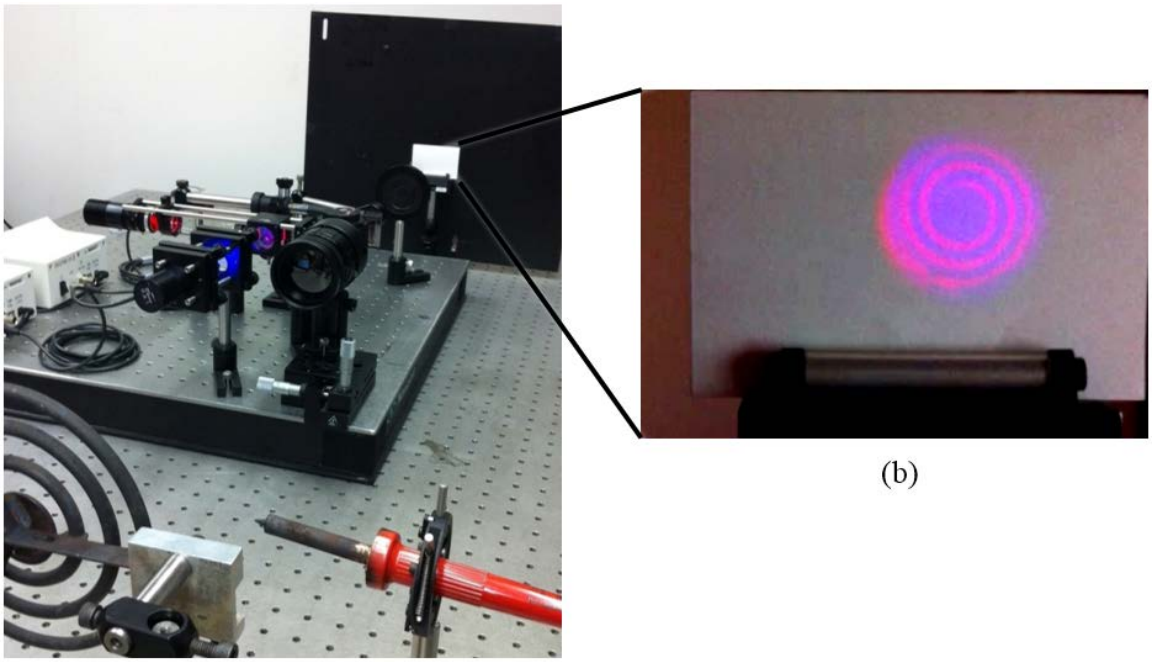

Figure 6-7. False color direct view IR imaging system based on MEMS array and reflectometry readout: (a) layout of system; and (b) detail showing projected IR image of heating coil at approximately 300 °C.

This system was used to project live IR images onto a screen which could then be directly observed with the naked eye. A sequence of projected thermal images is shown in Figure 6-8. The direct view IR image projection system was then used to image a scene consisting of a soldering iron and coiled heating element, and a sequence of images of the projection screen were captured as shown in Figure 6-9.

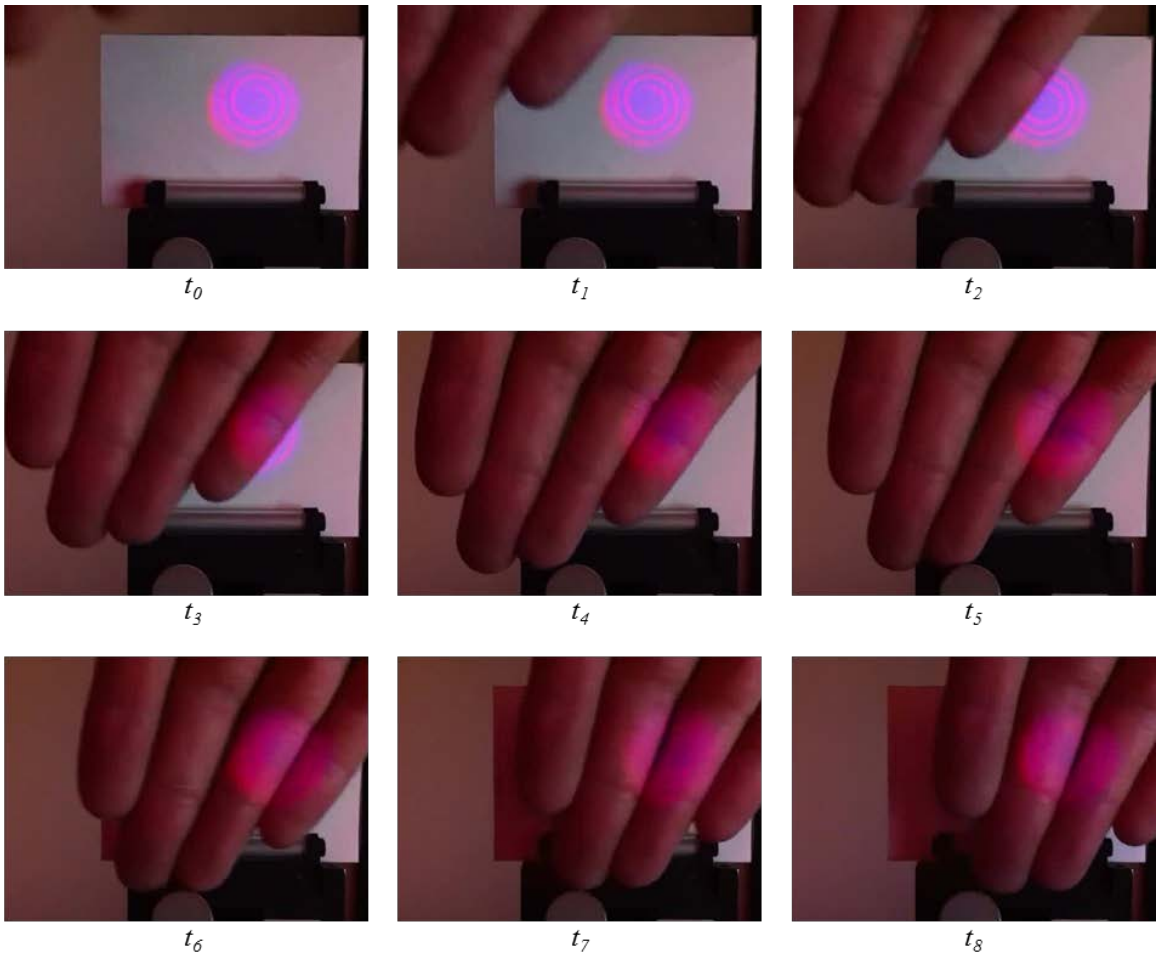

Figure 6-8. Sequence of images, at times t_i, of the projected thermal image from the developed IR direct viewing system. A projected thermal image of a heating coil is visible at t_0, and a hand enters the scene from above at t_1. The live thermal image is projected onto the hand as it is passed in front of the screen in $t_2 - t_8$. These images were captured with moderate ambient lighting conditions and the projected live thermal image could be observed directly with the naked eye.

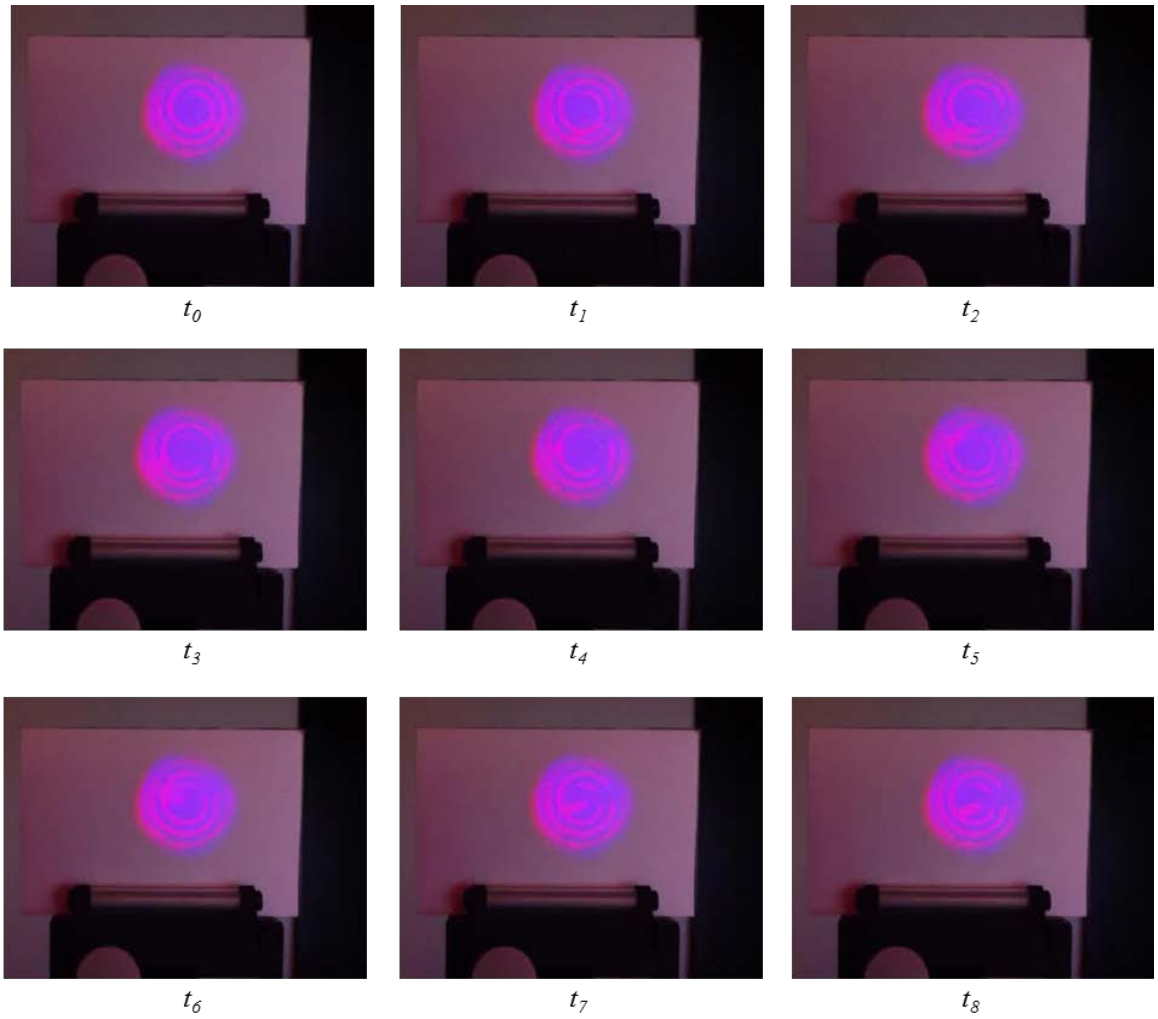

Figure 6-9. Sequence of images, at times t_i, of the projected thermal image from the developed IR direct viewing system. A projected thermal image of a heating coil is visible at t_0, and a soldering iron enters the thermal scene from the lower right at t_1. The soldering iron is moved across the field of view from $t_2 - t_5$ and then moved back to the center of the scene at $t_7 - t_8$.

The ambient light was then dimmed in order to increase the relative brightness of the projected image and increase the contrast of the captured images of the screen. A sequence of captured images is shown in Figure 6-10.

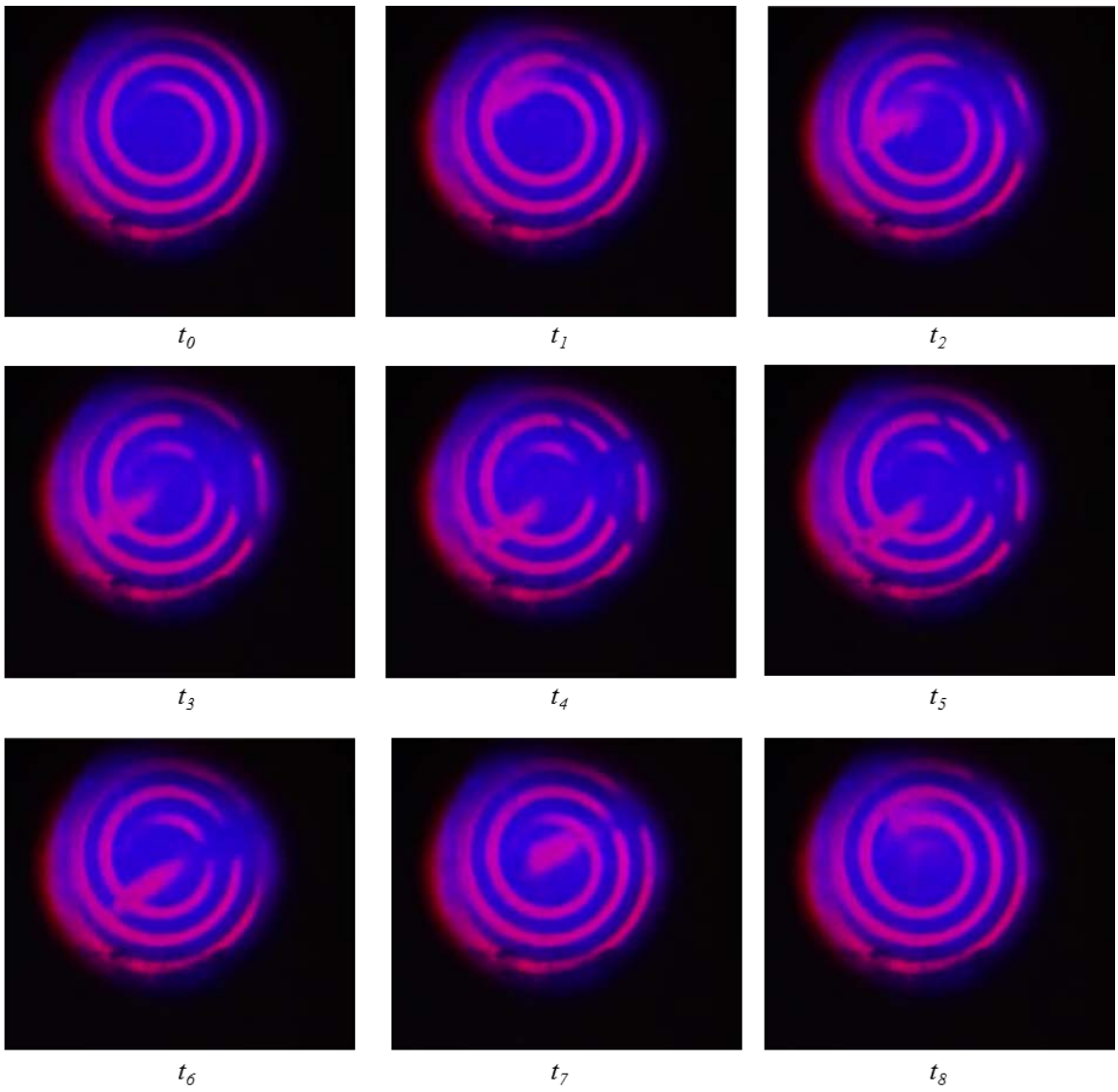

Figure 6-10. Sequence of images, at times t_i, of the projected thermal image from the developed IR direct viewing system. A projected thermal image of a heating coil at approximately 300 °C is visible at t_0, and a soldering iron with a temperature of approximate 400 °C enters the scene from above at t_1. The soldering iron is moved across the field of view from $t_2 - t_5$, and then moved back towards the top of the scene from $t_7 - t_8$. Blurring of the thermal image can be seen in t_8 due to the response time of the IR imaging system.

A sequence of images was then captured of the projected thermal image for a scene consisting of a heating coil at approximately 300 °C and a human hand at approximately 30 °C as shown in Figure 6-11.

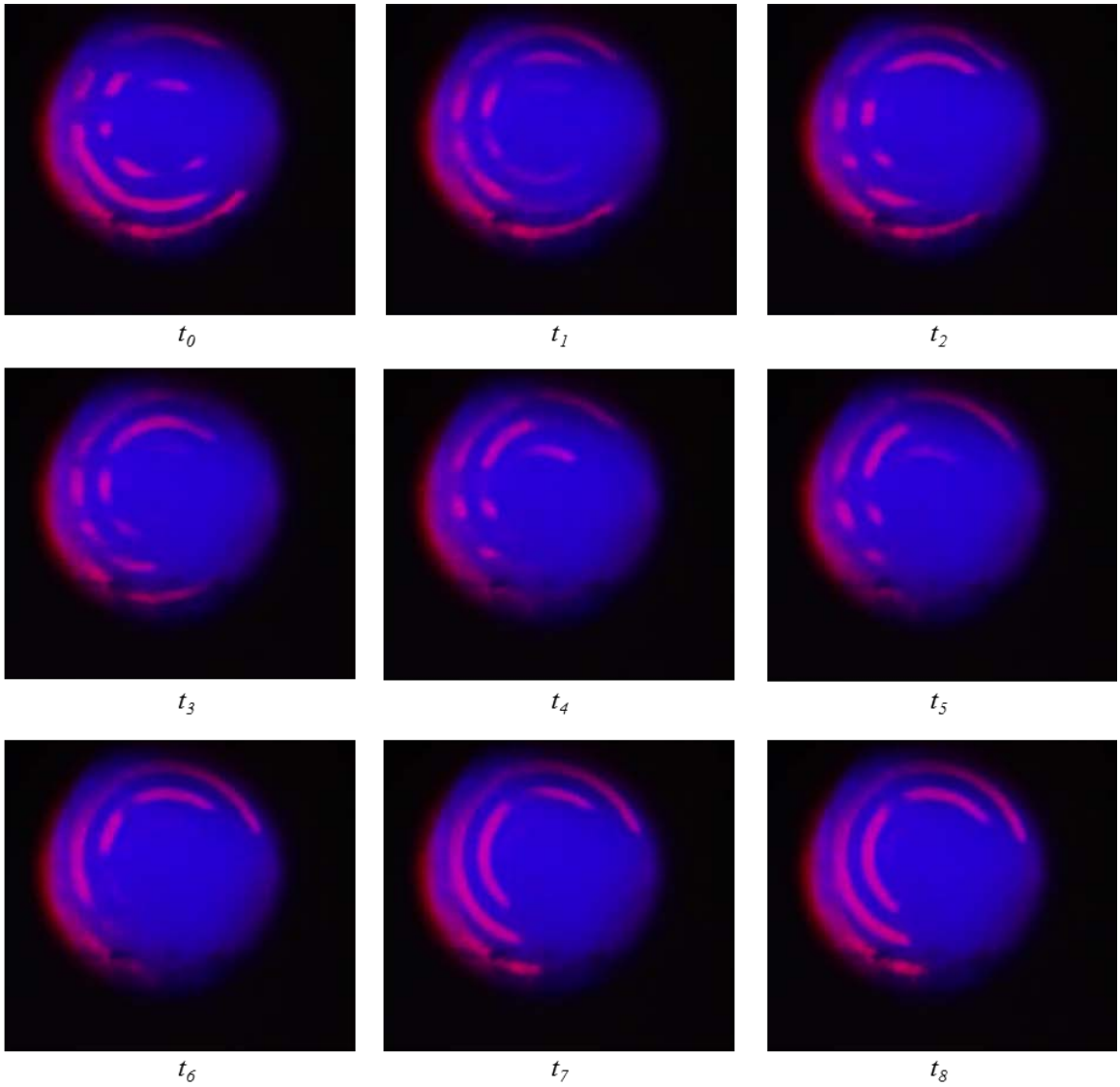

Figure 6-11. Sequence of images, at times t_i, of the projected thermal image from the developed IR direct viewing system. A projected thermal image of a hand with a temperature of approximate 30 °C in front of a heating coil at approximately 300 °C is visible at t_0. The hand forms a "thumbs up" sign from $t_6 - t_8$ however the IR radiation from the hand itself is not sufficient to achieve a significant color difference in the projected image.

Representative results of the color range of the developed false color IR direct view system are shown in Figure 6-12 and Figure 6-13, where each colored source is shown independently before being combined to create the false color image.

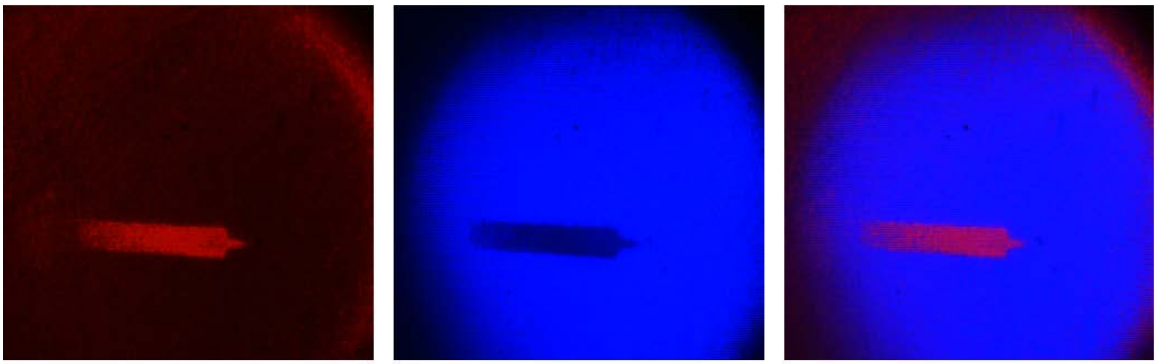

Figure 6-12. Representative direct view infrared images of a soldering iron using (a) only a red light source, (b) only a blue light source, and (c) both light sources for false color imaging.

According to Figure 6-12, a soldering iron with a temperature of approximately 400 °C can be distinguished on the projection screen. The output from each illumination source can be seen individually and the combined output provides a false color IR imaging system where the hot soldering iron appears red and the cooler background appears blue.

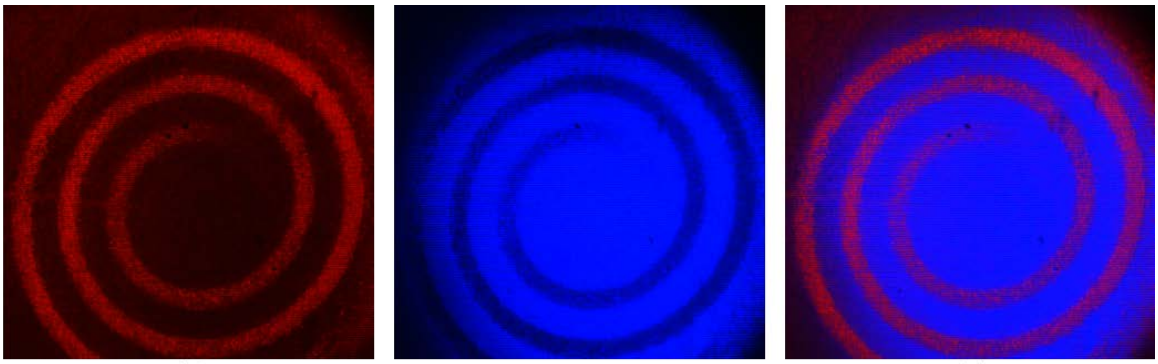

Figure 6-13. Representative direct view infrared images of a heating coil using (a) only a red light source, (b) only a blue light source, and (c) both light sources for false color imaging.

The heating element shown in Figure 6-13 has a temperature of approximately 300 °C and is easily distinguished on the projection screen. While these representative results qualitatively display the capability of the system, both video and live demonstrations achieve similar quality and offer a more complete perspective of the performance of the system. Next, characterization of the system was performed in order to quantify the previously observed performance of the direct view false color IR imaging system.

7. Characterization of Reflectometry Readout and Direct View System

7.1. Computer Subtraction to Verify Reflectometry Readout Sensitivity

In order to verify that the reflectometry based readout was sensitive to infrared radiation from a scene, computer processing was used to amplify changes in brightness of the output so that small changes in cantilever position could be more easily observed. Custom software was developed in order to record a baseline or reference image of the array and then display only subsequent changes in the intensity of the image [**63**]. This was accomplished by storing an initial reference image of the FPA in a relaxed state (at room temperature), and then subtracting this reference from subsequent camera frames to display only the changes in the camera view that occurred when radiation from a scene was introduced. Because this system amplified changes in brightness, a monochromatic camera could be used. A Pike F100B was suitable for this task and interfaced with the pre-existing custom software that was modified for the current work. A representative reference image that was stored using this software is shown in Figure 7-1.

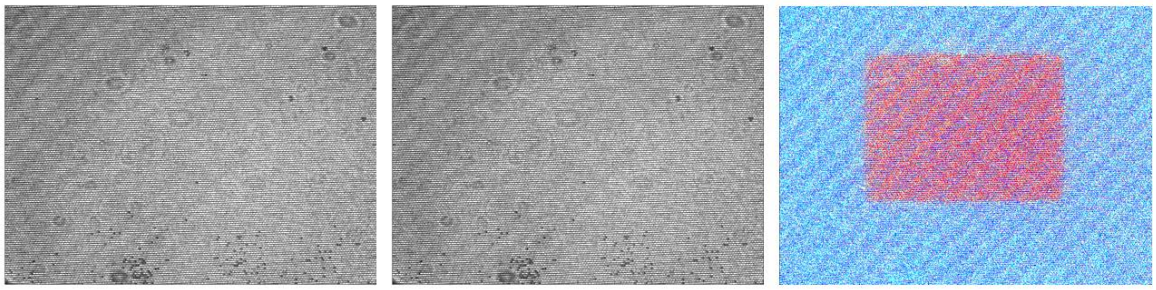

Figure 7-1. Representative images used in subtraction processing: (a) a reference image of the FPA, stored for an ambient temperature scene; (b) image of the FPA exposed to an object 15 °C above ambient temperature; and (c) the absolute result of subtracting the reference from the live image, and the addition of a false color map. Deviations from an ideal setup include non-responsive pixels of the FPA and non-uniformities in the image of the array.

The absolute difference between the reference image and subsequent frames can then be recorded or displayed as a live thermal image using an electronic display. This allows small changes in the measured brightness to be amplified into much larger changes which can be easily perceived. For example when observing the live, unprocessed image of the FPA, it is not possible to perceive the change in brightness caused by the thermomechanical deformation of the sensing elements exposed to infrared radiation from a scene with objects in the human body temperature range. However, when displaying the amplified result of computer subtraction, live images of a human face and hand are clearly visible, as shown in Figure 7-2.

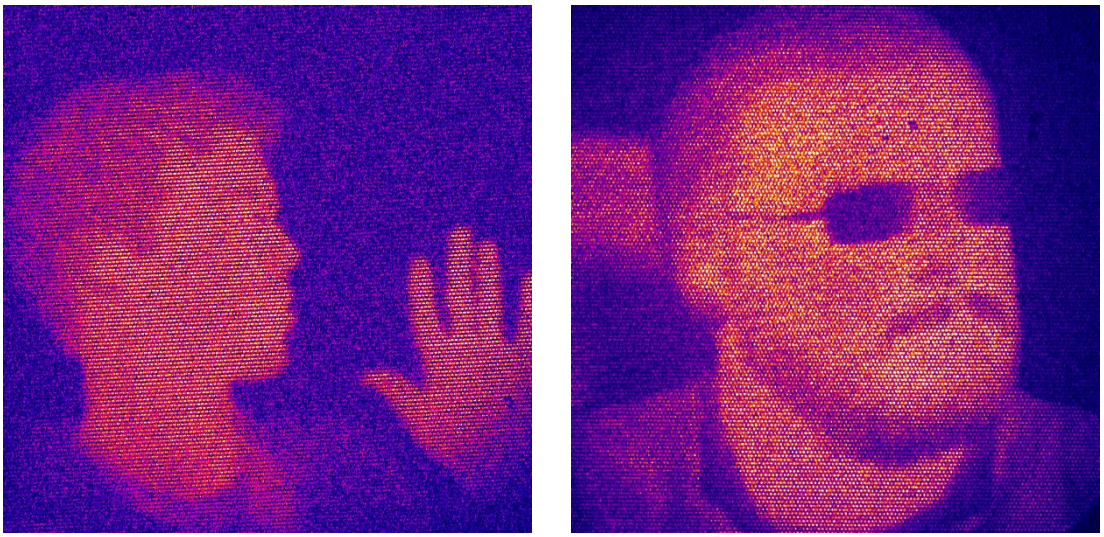

Figure 7-2. Thermal images of two persons captured using image subtraction by computer processing. The temperature of the human hand is approximately 31 °C and differences in temperature across the face and nose are on the order of 1-3 °C.

Figure 7-2 shows that the temperature of the human body can be imaged, with sufficient sensitivity to distinguish details of the face and hair. Spectacles exhibit especially high contrast because they block IR from the body and are themselves at nearly ambient temperature. Additional computer processing can be used to add a false color scale similar to that of commercial IR systems. A sequence of thermal images captured using computer subtraction with the developed reflectometry readout is shown in Figure 7-3 where human hand is clearly distinguishable in the live thermal images shown in In Figure 7-3, and can be seen opening and then closing to form the “thumbs up” sign. A sequence of thermal images was then recorded for a human face, as shown in Figure 7-4 which shows thermal images of a human face, including details such as the cooler edge of the ear and motion of the eyebrows. Finally, a sequence of thermal images showing

details of the temperature distribution across a shirtsleeve and cuff are shown in Figure 7-5.

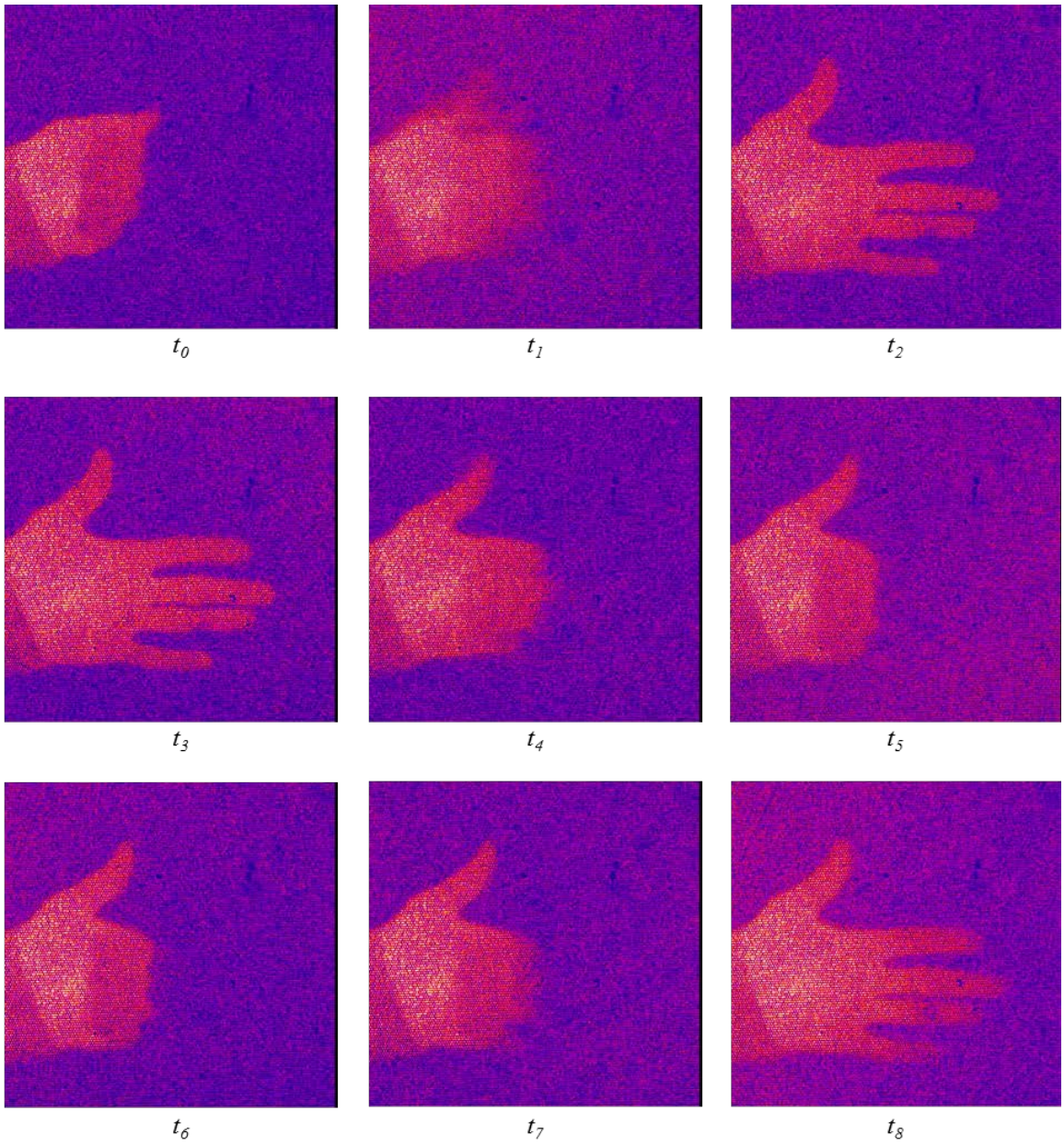

Figure 7-3. Sequence of thermal images, at times t_i, obtained with the developed reflectometry readout, using subtraction of a reference image and the addition of a false color scale. The closed hand at t_0 opens by t_2 and then closes again to form the "thumbs up" sign at t_6 before reopening by t_8.

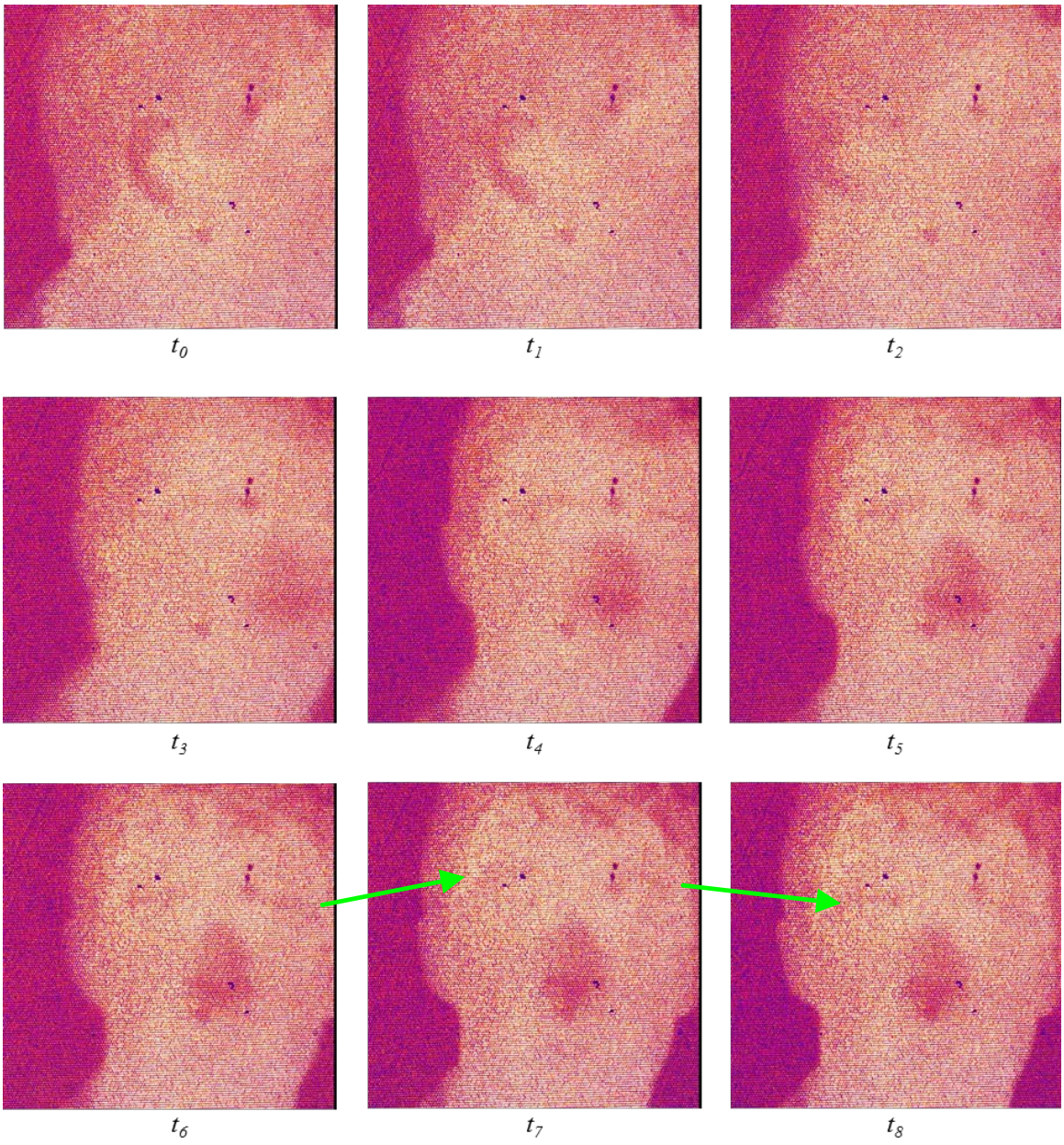

Figure 7-4. Sequence of thermal images, at times t_i, obtained with the developed reflectometry readout, using subtraction of a reference image and the addition of a false color scale. The cooler edge of the ear can be seen at t_0 and movement of the eyebrows, highlighted by the green arrows, is shown in $t_6 - t_8$. The movement of the eyebrows was much more noticeable in the live output as well as in videos that were recorded of this scene.

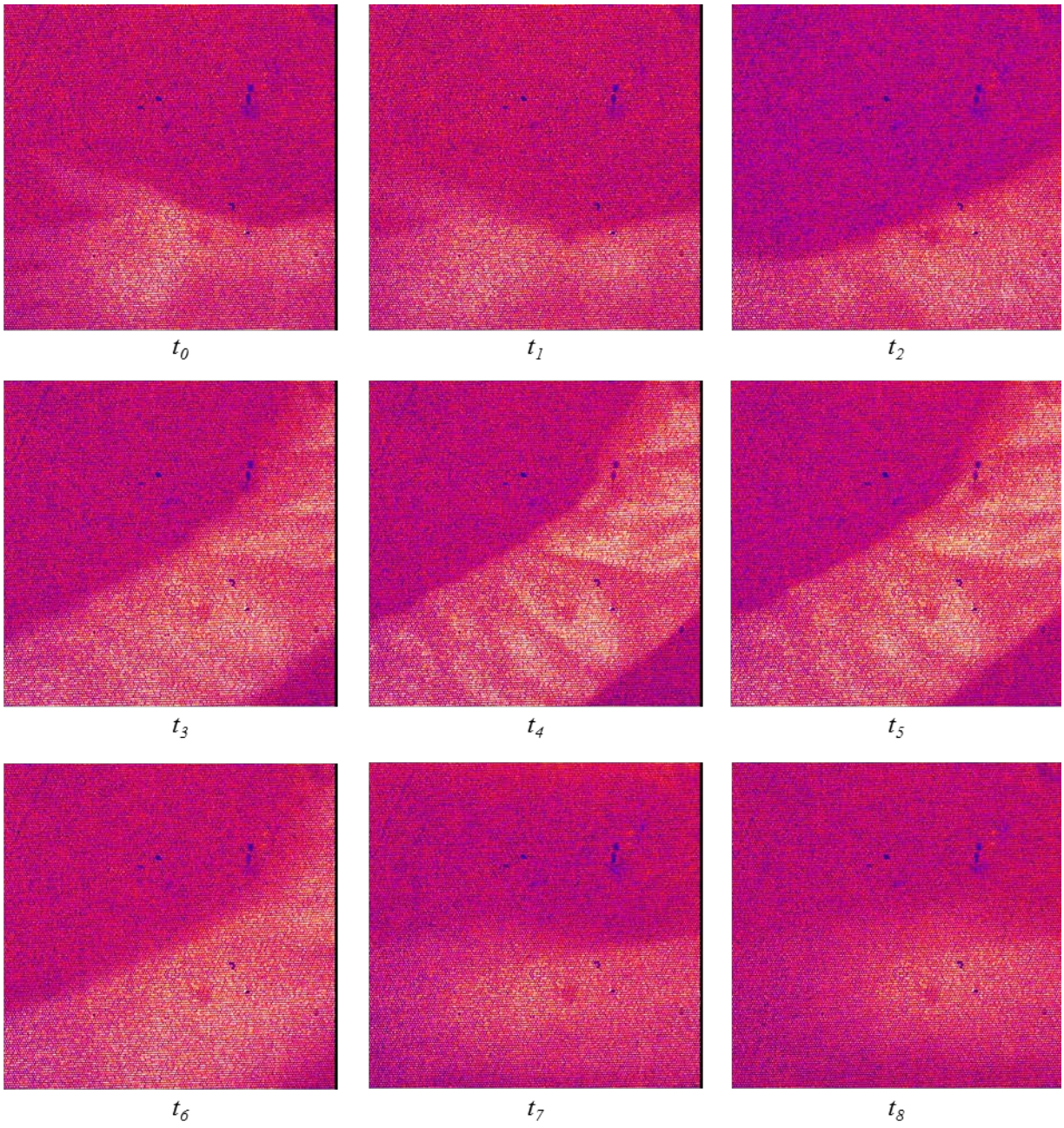

Figure 7-5. Sequence of thermal images, at times t_i, obtained with the developed reflectometry readout, using subtraction of a reference image and the addition of a false color scale. The hand visible at t_0 moves into the frame to show the arm and shirtsleeve at t_4 where temperature variations across the folds of fabric in the sleeve are visible. The arm is then withdrawn from the frame from $t_6 - t_8$.

A comparison of a visible light image, thermal image from a commercial thermal camera, and representative image from the reflectometry readout is shown in Figure 7-6.

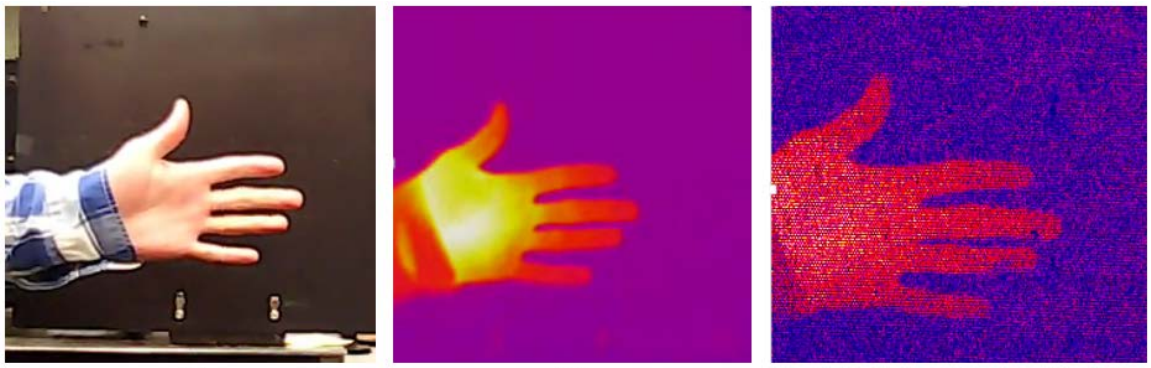

Figure 7-6. Comparison of (a) visible light, (b) commercial thermal camera, and (c) computer processed reflectometry output.

Figure 7-6 demonstrates that the infrared imaging system based on the reflectometry readout is sensitive to infrared radiation from low temperature sources. Next it is desirable to quantify the temperature sensitivity of the reflectometry readout as this affects the performance of the system as an IR direct viewer.

7.2. Noise Equivalent Temperature Differential (NEDT) Analysis

After observing that limited computer processing could be used with the reflectometry based system in order to image low temperature scenes such as a human hand or face, the performance limits of the reflectometry readout were quantified. Because this system operates on very small changes in illumination intensity, any fluctuation in the power of

the light used to image the FPA will have serious detrimental effects on the quality of the image produced. In order to achieve stable illumination conditions and more accurately measure the performance of the readout mechanism separately from variations in the illumination, a laser source with active temperature control was used in place of the passively-cooled LEDs used in the demonstration of the direct view system. Noise equivalent temperature differential (NEDT) is used as a metric for quantifying the performance of IR imaging systems and represents the change in temperature that is equivalent to noise in the imaging system; temperature fluctuations below this level will be indistinguishable from other noise [**64**]. In order to accurately determine the NEDT of the developed readout system, a precisely-controlled radiation source is required to eliminate temperature fluctuations.

7.2.1. Blackbody Target Projector

Differential blackbodies are used provide precisely controlled radiation sources in order to measure the performance of IR imaging and detection systems that are sensitive to small changes in scene temperature. The currently used Santa Barbara Infrared 14000Z is capable of controlling the temperature difference between an ambient target and a blackbody emitting surface [**65**]. The system uses a temperature probe to measure the temperature of an ambient surface, and precisely controls the temperature of a blackbody to achieve the desired differential. The system can also be operated in an absolute temperature mode, where the blackbody temperature is controlled independently from the ambient temperature. The temperature resolution of the 14000Z is 0.001 K, and the

output is collimated in order to eliminate the effects of distance between the blackbody system and the IR imaging apparatus. A schematic of the blackbody projector is shown in Figure 7-7.

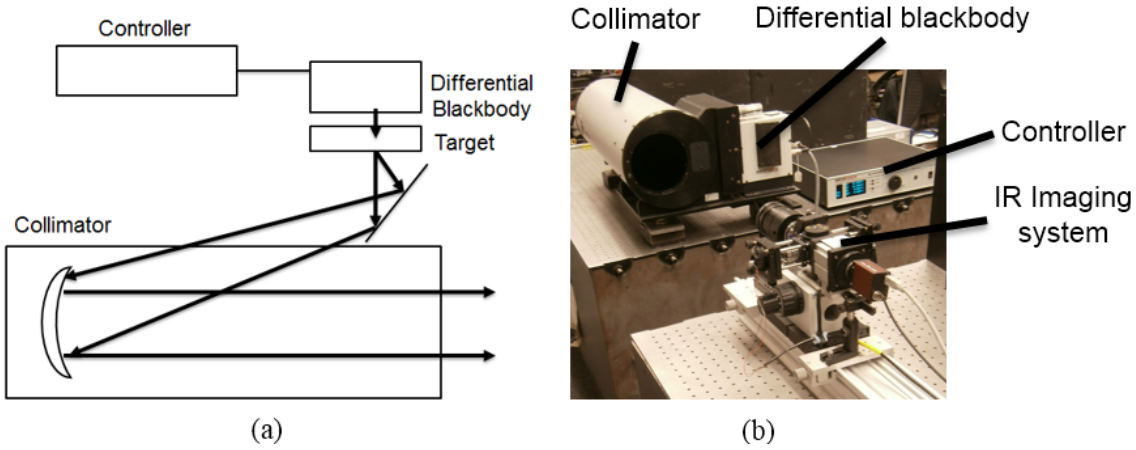

Figure 7-7. The collimated blackbody projector used in this work [**14**]: (a) schematic of collimated blackbody projector; and (b) projector used to calibrate the system.

The differential blackbody is a coated surface with an emissivity close 1.0 and is located behind the target, a solid copper disk which may contain a variety of cutout shapes that are used to project specific shapes or patterns of IR radiation. [**14**]. Here, no specialized pattern is required, and the chosen projected shape is square as shown in Figure 7-8, where the blackbody is operated in absolute mode and set to a temperature of 30 °C.

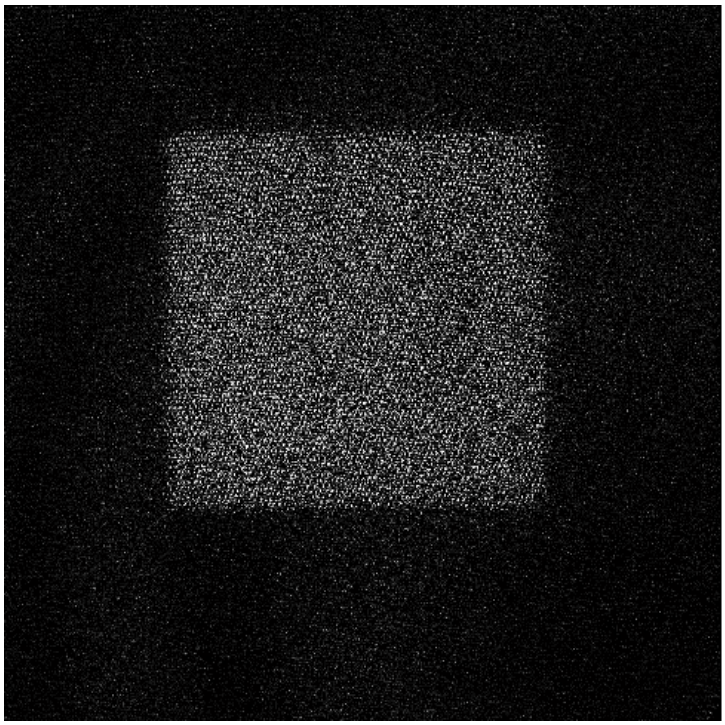

Figure 7-8. Image obtained using computer subtraction of blackbody source at 30 °C.

While Figure 7-8 provides qualitative check that the imaging system is sensitive to low temperature scenes, the blackbody is specified to maintain a temperature uniformity of better than 0.01 °C over a minimum of 90% of its emitting surface, with a temperature stability of better than 0.001 °C [**65**] and can be used to quantitatively measure the performance of the IR imaging system.

7.2.2. Procedure for Determining Reflectometry Sensitivity

The blackbody target projector provides a highly precise source of IR and allows for the calculation of the Noise Equivalent Temperature Differential (NEDT) of the imaging

system. This is the smallest temperature differential that would be distinguishable from the noise in the imaging system. The information required to determine system NEDT can be recorded in the form of several data cubes, each made up of sequentially captured image frames of the FPA. The data cube can be visualized as shown in Figure 7-9.

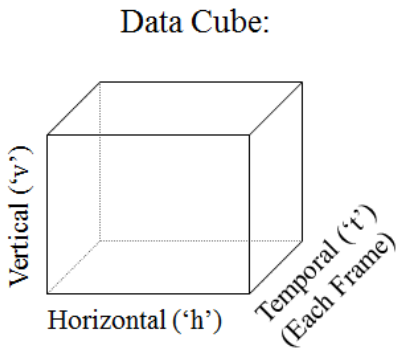

Figure 7-9. Visualization of data cube used for NEDT calculations. The vertical and horizontal axes represent the dimensions of an image and the temporal axis represents the successively captured frames [**14**].

The noise that is present in the system can be quantified using a procedure similar to that used for determining the NEDT of commercial thermal cameras [**64**]. Three cubes of data are required, using the blackbody set to three different temperatures, and the NEDT is calculated as follows. The first data cube is made up of 64 camera frames of the blackbody which is set to a temperature of 20 °C (T_1). This cube is flattened into a single array by calculating the average along the temporal direction for each pixel to create a response array at 20 °C. The second data cube contains 128 frames captured with the blackbody set to 25 °C (T_3). The temporal noise of the system is found by calculating the standard deviation, along the temporal direction, for each pixel in this array. The

third cube is similar to the first, except with the blackbody set to 30 °C (T_3). This produces the response array of the system for 30°C. The responsivity of the system can then be given by

$$Responsitivity = \frac{(Response\ T_3)\ -\ (Response\ T_1)}{(T_3 -\ T_1)}, \tag{7-1}$$

where the response arrays at T_1 and T_3 have units of digital count and the responsivity array has units of digital counts per Kelvin. The NEDT can then be determined by dividing the temporal noise array by the response array, as

$$NEDT = \frac{Temporal\ noise}{Responsivity}, \tag{7-2}$$

where the temporal noise has units of digital counts, and the NEDT array has units of Kelvin or degrees Celsius. The NEDT can then be expressed as a single value by calculating the mean of the NEDT array. This is commonly multiplied by 1000 to give NEDT with units of milli-Kelvin (mK).

7.2.3. Results of Reflectometry Readout Sensitivity Analysis

A Pike F100B camera with a 1.0x telecentric lens was used to image the FPA. The light source was a ThorLabs LPS-660-FC fiber coupled pigtail laser driven using a ThorLabs

TCLDM9 laser mount with integrated TEC element connected to a ThorLabs ITC502 laser diode and temperature controller. The temperature control was used to stabilize the power output of the laser. The Santa Barbara Infrared 14000Z blackbody was placed 18 inches from the infrared lens of the IR imaging system and the controller was set to operate in absolute temperature mode. The data cubes recorded consisted of 64 frames at 20.000 °C, 128 frames at 25.000 °C, and 64 frames at 30.000 °C. The infrared radiation from the blackbody was focused onto an area of the FPA that corresponded to an area of roughly 500 × 500 camera pixels. Of this active area, the central 400 × 400 area was selected. The NEDT was determined to be 137.82 mK. This indicates the sensitivity, with respect to changes in scene temperature, for the reflectometry readout when using a camera to measure the output. While the output variations corresponding to changes in scene temperature of a few degrees Celsius can be easily detected by a camera system, the optical readout requires substantially larger temperature variations in order to produce output variations that are easily detectable by the naked human eye. While the previously demonstrated direct view IR imaging system was able to produce significant changes in output when imaging objects with temperatures greater than approximately 300 °C, the system was not sensitive enough to produce noticeable changes in output for the temperature range in which the current blackbody operates.

7.3. Characterization of the Direct View IR Imaging System

In order to measure the performance, with respect to a human observer, of the direct view IR imaging system based on the reflectometry readout that was developed, the output must be quantified in relation to the HVS. This can be accomplished by measuring the color output across a range of scene temperatures in order to then determine the change in temperature that would result in a noticeable change in color. The first step in this process was to obtain a test object for which the temperature could be controlled across the temperature measuring range of the direct viewer. The output from the readout mechanism, across the temperature imaging range of the system, was then recorded using a color sensitive visible light camera that stored color images into the sRGB color space. The measured data were transformed into the CIEXYZ human vision color space based on the perception of a human observer and then transformed again into the CIELAB perceptual color space in order to allow for the determination of perceptual color differences which were calculated using the CIEDE2000 color difference formulas. This allowed for the determination of the relationship between the scene temperature and the perceived color output that could be observed by the HVS using a method similar to that described in Section 5.2. The minimum change in temperature required to achieve a theoretically noticeable change in color can be used as a metric for the temperature sensitivity, with respect to a human observer, of the direct view IR imaging system based on a reflectometry readout.

From preliminary testing, it was found that, without computer processing, the system is able to achieve strong color formation when imaging hot objects such as a soldering iron with a temperature of approximately 400 °C. However, imaging cooler objects such as a human hand or face did not produce obvious changes in output. A blackbody projector, which outputs precisely calibrated radiation equivalent to that from a blackbody at a specific temperature, would work well for providing a scene of known temperature in order to measure the IR imaging system response. However, the temperatures needed to characterize the direct view system are above the range of the previously used blackbody target projection system and an alternate, high temperature, source of IR radiation is required.

7.3.1. High Temperature Source

An alternate method of providing known temperature input was developed based on a variable voltage transformer and a coiled electrical heating element. A variable transformer can be used to vary the voltage, and therefore power, in a heating element. The temperature of the heating element will increase until the heat flow out to the surroundings is equal to the electrical power input from the transformer. Such an apparatus was constructed, and a commercial thermal camera was used to measure the steady state temperature across a range of voltage inputs. The use of a thermal camera allowed for temperature measurements across the entire surface of the heating element, as shown in Figure 7-10.

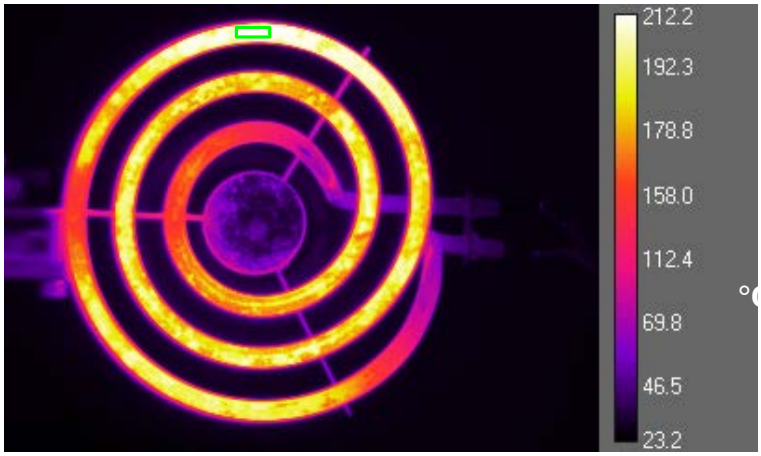

Figure 7-10. Thermal image of coil heating element. The temperature in the area of interest, shown by the green box near the top of the coil, is approximately 212°C for a variable transformer output of 66 Vrms (55% of 120 Vrms).

The relationship between voltage and temperature was then determined and found to be linear. The plot of data collected and the linear fit that was determined are shown in Figure 7-11.

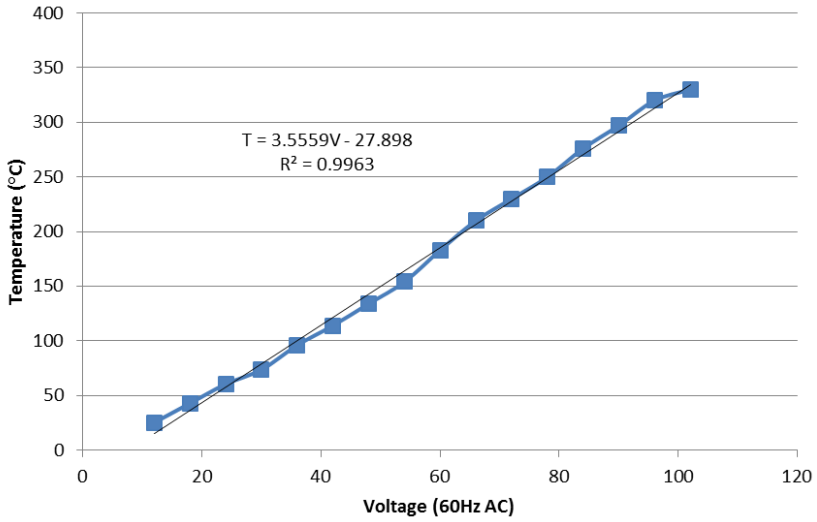

Figure 7-11. Temperature versus voltage for coil heating element including highly correlated linear fit.

The linear fit shows a coefficient of determination of 0.9963. This indicates that the linear fit will account for greater than 99.6% of the variance in the sample data and that the relationship between the voltage and temperature can be accurately modeled using a linear equation. The coil heating element apparatus can then be used as a known, variable, temperature input for measuring the sensitivity of the IR imaging system.

7.3.2. Color Measurement

The output from the IR imaging system was measured using a data cube technique. A PixeLINK PL-A782 visible light camera was used to capture the color output from the reflectometry readout mechanism and, while the camera did not exactly match the perception of a human observer, the measured color data were used to estimate the relative colors that a human observer would perceive. Images and video from the camera were captured using PixeLINK Capture OEM software [**66**]which allows for the control of many relevant parameters including gamma and color temperature, as shown in Figure 7-12.

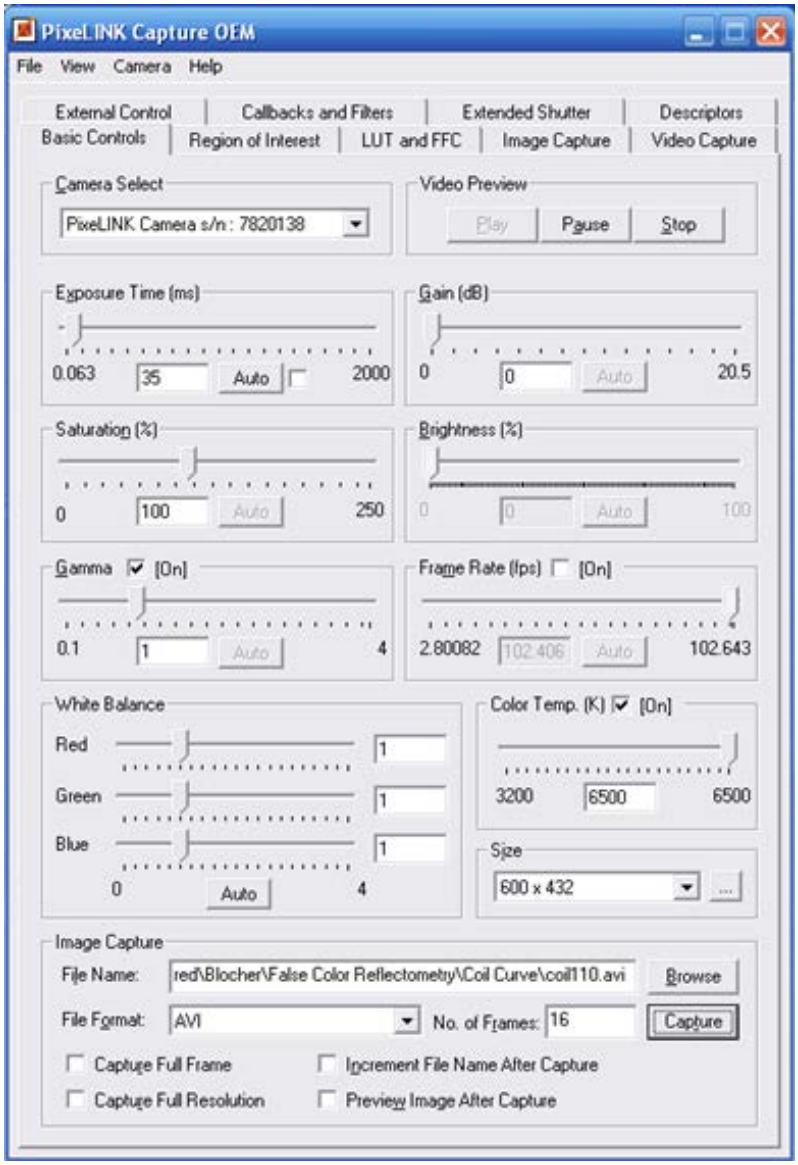

Figure 7-12. PixeLINK Capture OEM software used to record images from the visible light camera [**66**].

A gamma correction of 1.0 was used in order to achieve a linear encoding of the image information. This will produce linear sRGB values and will not require gamma

correction before transforming color spaces. A color temperature of 6500 K was also used to match the D65 standard illuminant that is used in the sRGB color standard.

The individual cantilever elements in each row become indistinguishable when the knife edge filters are arranged to provide maximum system sensitivity. However, each row of cantilevers is clearly visible, and a representative area 10 pixels wide by 3 pixels high was chosen from the captured image of the readout. This corresponds to an area on the FPA of roughly 35µm by 10.5µm, an area slightly smaller than one 45µm by 20 µm cantilever element.

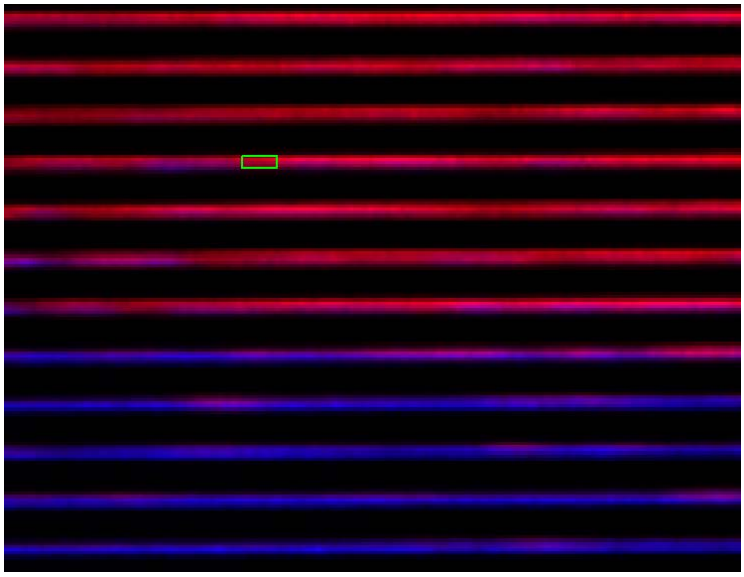

Figure 7-13. Subsection of image captured using visible light camera. The green box outlines the area that was used for color measurements. The cantilevers in the top section of the image are exposed to IR from a scene while those at the bottom remain in their relaxed state.

This area was repeatedly measured while the temperature of the heating element was varied. The range of images that were captured are shown in Figure 7-14 where the temperature ranges from 50 °C to 390 °C.

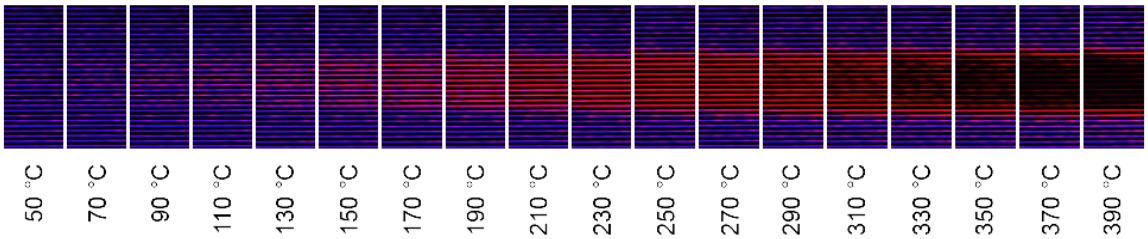

Figure 7-14. Captured images of a subsection of the FPA exposed to temperature ranging from 50 °C to 390 °C.

The rectangular shape of the heating element became identifiable when its temperature reached approximately 150 °C, and the middle of the array subsection, which is exposed to IR from the heating coil, produced a smooth transition from blue to red as the temperature was increased. Then, at a temperature of approximately 300 °C, the color began to fade and darken in the center section of image when the cantilever elements deflected enough that the red light was shifted completely past the filter opening and began to be blocked again. This matched the behavior of the reflectometry readout that was predicted by Eq. 5-38.

For each temperature measurement, 16 frames from the camera were stored. Median filtering was performed by flattening the 16 frames into a single frame that consisted of the median for each element. The average value of this flattened frame was then determined by averaging rows into a single column, and then averaging the column to

arrive at a single value. This was performed individually for each of the R, G, and B components of the captured images, to produce an sRGB triplet for each measured temperature. The measured relationship between temperature and linear sRGB values is shown in Figure 7-15.

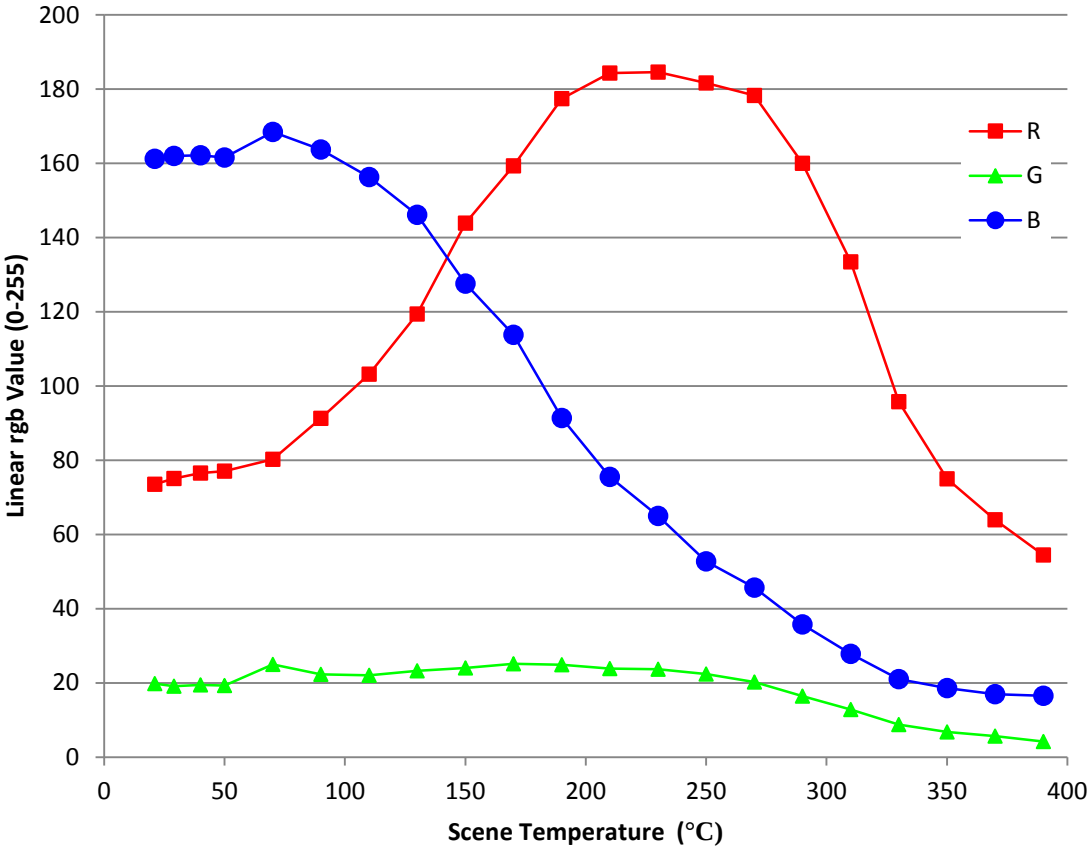

Figure 7-15. Measured linear RGB values versus scene temperature. Measurements used a gamma of 1.0 and a 6500 K color temperature.

According to Figure 7-15, the red channel of the RGB (dominated by the red light source) steadily increased with temperature, while the blue channel (dominated by the blue light

source) decreased with temperature, across the temperature range of approximately 50 °C to 250 °C. This is the desired behavior based on the arrangement and light sources that were used. System repeatability was investigated by performing three sets of measurements for each color channel across the temperature range of 110 °C to 170 °C. This range was chosen for the large local change in both the Red and Blue channels. The results of the repeatability measurements are shown in Table 2-1.

Table 7-1. Repeatability results for color output including mean, standard deviation (SD), and relative standard deviation (RSD) at four temperatures from 110 °C to 170 °C.

	Red			Green			Blue		
Temperature	Mean	SD	RSD (%)	Mean	SD	RSD (%)	Mean	SD	RSD (%)
110 °C	103.5	1.13	1.09	22.07	0.06	0.25	152.9	2.91	1.90
130 °C	119.6	2.61	2.18	22.68	0.51	2.24	144.1	2.41	1.67
150 °C	143.5	0.69	0.48	24.03	0.14	0.59	126.9	0.70	0.55
170 °C	158.3	1.04	0.66	24.87	0.24	0.97	112.4	1.92	1.71
Mean	131.2	1.37	1.04	23.41	0.24	1.01	134.1	1.98	1.48

According to Table 7-1, the average relative standard deviation is less than 1.5% of the mean for all cases. The complete series of measured data points were then expanded to a more continuous data set through the use of interpolation. In this case, cubic interpolation was performed using the *interp1* Matlab function in order to preserve the shape of the data curve between points through the use of piecewise cubic interpolation. The measured and interpolated linear sRGB values were then gamma corrected, using a gamma correction of 2.2 to approximate the sRGB gamma function, and the resulting range of colors is shown in Figure 7-16.

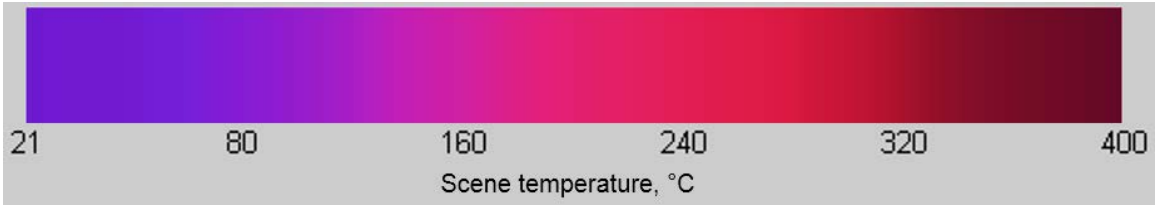

Figure 7-16. Representation of the gamma corrected color output from the reflectometry based direct viewer as calculated from measured linear RGB values.

As shown by Figure 7-16, the color range of the output from the reflectometry based direct view system extends from a bluish-purple at low temperatures to a deep red at high temperatures. This indicates that the readout successfully achieved false color thermal imaging using the desired blue-red color map. It is important to note that most color cameras do not exactly match the sensitivity of the human eye, and specially calibrated devices meant to exactly record the color that would be perceived are known as colorimeters. As a result, the color shown here is what would be observed if the output from the camera were displayed on an accurate electronic display, but may differ from what would be observed if the naked human eye was used in place of the visible light camera. While these measured RGB colors were likely not a precisely accurate measurement of the colors that would be perceived by a human observer, they can be used with color difference calculations to give an estimate of the relative sensitivity of the direct view IR imaging system that was developed.

7.3.3. Color Difference and Temperature Sensitivity

The first step in the process of calculating color differences from the measured RGB data was to transform the interpolated linear RGB values into the CIEXYZ color space. This was performed using a transformation matrix, M, for the particular color space and white point used. Because most color cameras encode into the sRGB color space [**67**], the current work used the transformation matrix for the sRGB color space and D65 white point given by [**36**]

$$M = \begin{bmatrix} 0.4124564 & 0.3575761 & 0.1804375 \\ 0.2126729 & 0.7151522 & 0.0721750 \\ 0.0193339 & 0.1191920 & 0.9503041 \end{bmatrix}, \tag{7-3}$$

where the values for the particular transformation have been calculated from the chromaticity coordinates of the sRGB color space and the white point of the illuminant [**36**]. The transformation from RGB to XYZ was accomplished by

$$\begin{bmatrix} X \\ Y \\ Z \end{bmatrix} = M \begin{bmatrix} R \\ G \\ B \end{bmatrix}, \tag{7-4}$$

where the RGB values must be linear with respect to intensity and must be normalized to the nominal range of 0.0 to 1.0. The resulting XYZ values were then in a perceptual color space, and could be converted to CIELAB using a procedure similar to that described in Section 5.2. The CIELAB values were then used in conjunction with the

CIEDE2000 color difference formulas to determine the change in temperature that is required to achieve a just noticeable change in color, or delta E equal to 2. The increase in temperature, across the temperature imaging range, required to achieve a CIEDE2000 delta E of 2.0 is shown in Figure 7-17.

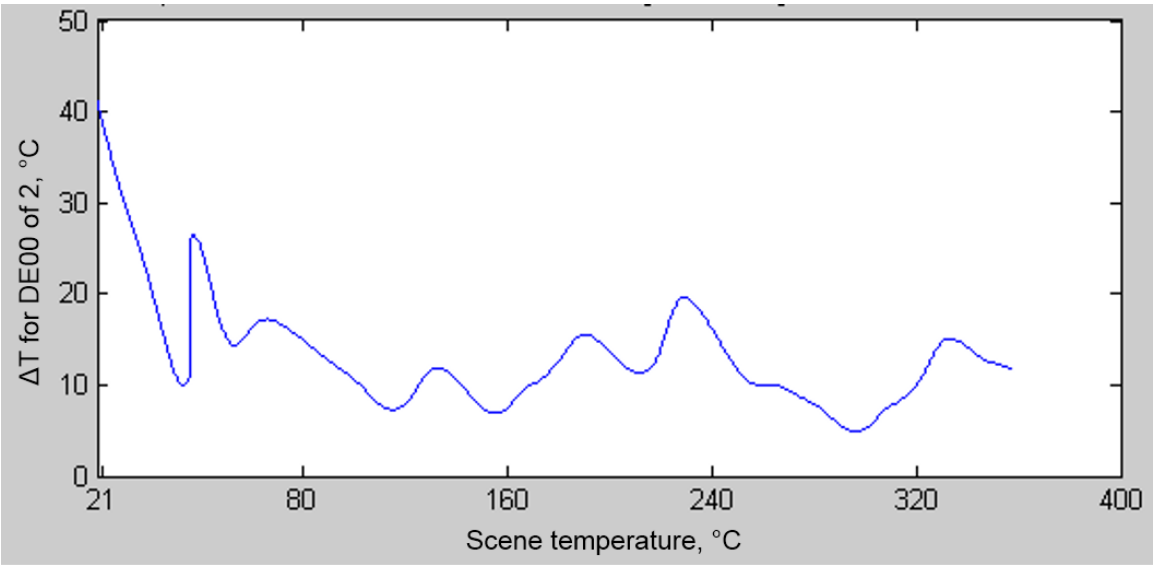

Figure 7-17. Calculated temperature increase required for just perceptible change in color based on CIEDE2000 color difference formulas, based on the sRGB approximation of the observable color at each specific temperature.

According to Figure 7-17, while the temperature sensitivity was not perfectly consistent across the measuring range, it did have a linear trend. At the most sensitive areas the noticeable color change was less than 10 °C and the IR imaging system was slightly more sensitive, based on the estimated perception of a human observer, in the red areas. This was similar to the results of the analytical evaluation of the reflectometry readout, discussed in Section 5.2.7.

8. Conclusions, Recommendations, and Future Work

A unique direct view infrared (IR) imaging system based on a MEMS array has been developed through the use of an innovative two color reflectometry readout. The system is based on an existing MEMS device which exhibits nano-scale deformations as a function of IR radiation from a scene. An optomechanical readout was used to transduce the nano-scale deformations of the MEMS array directly into an output that could be perceivable by the naked human eye in order to realize a direct view IR imaging system and eliminate the need for the readout integrated circuitry (ROIC), computer based signal processing, and electronic display used in conventional systems. Several readouts mechanisms were investigated, including two, one using live holography and one using Nomarski differential interference contrast (DIC), that were based on interferometry while a third, using reflectometry, was based on geometrical optics. IR imaging systems based on all three readouts were evaluated using an innovative analytical approach based on perceptual color differences, and preliminary experimental results were obtained using experimental setups for each method. The results of the analytical evaluations and preliminary experimental setups led to the selection of reflectometry as the most suitable readout for the further development of an IR direct viewing system. An innovative and unique IR imaging system based on a false color reflectometry readout was constructed, and live IR imaging results were demonstrated. The sensitivity of the readout was characterized and a system NEDT of approximately 137 mK was measured. The temperature sensitivity, based on the theoretical perception of a human observer, of the

false color direct view IR imaging system was determined to be on the order of 10 K based on perceptual color difference calculations performed using the measured output of the constructed direct view system. The direct view system was used to image objects with temperatures ranging from ambient to approximately 400 °C and demonstrated results showed that objects with temperatures as low as approximately 150 °C were clearly distinguishable in live thermal images.

Further development of the currently demonstrated system should include more complete characterization of the output, through the use of a colorimeter or spectrophotometer, as well as investigation of the uniformity of initial shape and responsivity across the array. Additional future work could also include the redesign and fabrication of new MEMS arrays for improved sensitivity. Arrays with higher responsivity would allow for a wider temperature range of IR imaging, particularly for low temperatures, and would extend the range of applications that the direct view system would be suitable for. Particularly, it may be desired to create a direct view IR imaging system that could be used to image low temperature scenes such as those of humans or animals. Also, the investigation and implementation of other and/or additional light sources would allow for a wide range of color maps and false color imaging options when using the reflectometry readout. The use of several colors and a system arranged to transmit individual colors at certain temperatures would allow for the development of a more quantitative direct view imaging system by mapping specific colors to particular temperature ranges in a scene. A new MEMS array could also be designed to include an area with known height gradients in order to provide an effective scale for the live deflection of active elements in the array.

An alternative to the addition of more differently color light sources might also be the use of a rainbow or similar colored filter, such as those used in color Schlieren imaging. This would involve the use of a single white light source in a reflectometry readout, but with the knife edge filters replaced with a color filter containing either a color gradient or any other color pattern. As focused illumination traverses the filter plane due to deformations of the MEMS structures in the FPA, the light could pass through differently colored sections of the filter before being transmitted to the observer or imaging lens. Such an arrangement would produce a color output dependent on the position of illuminating light on the filter plane. This could be used to achieve a false color system with many observable colors produced from a single white light source. Using a single light source could allow for the elimination of the beam combining optics required in a multiple-source system, and might lead to reduced system cost and complexity.

The redesign of the system for miniaturization and portability may also offer exciting possibilities for a portable, hand-held direct view infrared imaging system. Such a system could resemble standard binoculars and be used for thermal imaging in the wide range of applications that exist for current portable IR imaging systems. An additional possibility would be the inclusion of an ambient light capturing mechanism in order to eliminate the powered illumination source and produce a completely unpowered IR imaging system by illuminating the IR image with collected ambient light. Filters could be used to achieve several colors in order to maintain false color imaging capabilities. Other future work could include the investigation of the speed and transient response of a direct view system, along with the resistance to harsh environments and various uses.

The investigation of resistance to accelerations, mechanical shock, temperature variation, and vibration are all especially important for a rugged, portable direct view IR imaging system. Applications specific to the currently developed IR direct viewing technology would include harsh environments where electronics and computer system are not suitable and low power illumination sources would allow for reduced battery requirements in extended service applications.

References

[1] Miller, J., *Principles of Infrared Technology*, Van Nostrand Reinhold, 1994.

[2] Steffanson, M., Gorovoy, K., Ramkiattisak, V., Ivanov, T., Krol, J., Hartmann, H., and Rangelow, IW., "ARCH-type micro-cantilever FPA for uncooled IR detection," *Microelectron. Eng.*, 98:614-618, 2012.

[3] Lim, SH., Choi, J., and Horowitz, R., "Design and Fabrication of a Novel Bimorph Microoptomechanical Sensor," *JMEMS*, 14(4):683-690, 2005.

[4] Zhao, Y., Mao, M., Horowitz, R., Majumdar, A., Varesi, J., Norton, P., and Kitching, J., "Optomechanical Uncooled Infrared Imaging System: Design, Microfabrication, and Performance," *JMEMS*, 11(2):136-146, 2002.

[5] Perazzo, T., Mao, M., Kwon, O., Majumdar, A., Varesi, J. B., and Norton, P., "Infrared vision using uncooled micro-optomechanical camera," *Appl. Phys. Lett.*, 74(23):3567-3569, 1999.

[6] Liu, M., Zhao, Y., Dong, L., Yu, X., Liu, X., Hui, M., You, J., and Yi, Y., "Holographic Illumination in Optical Readout Focal Plane Array Infrared Imaging System," *Opt. Let.*, 34(22):3547-3549, 2009.

[7] Miao, Z., Zhang, Q., Chen, D., Guo, Z., Dong, F., Xiong, Z., Wu, X., Li, C., and Jiao, B., "Uncooled IR imaging using optomechanical detectors," *Ultramicroscopy*, 107:610-616, 2007.

[8] Guoa, Z., Zhang, Q., Dong, F., Chen, D., Xiong, Z., Miao, Z., Li, C., Jiao, B., and Wu, X., "Performance analysis of microcantilever arrays for optical readout uncooled infrared imaging," *Sens. Actuat. A-Phys.*, 137:13-19, 2007.

[9] Young, H. and Freedman, R., *University Physics*, 12th ed., Pearson Addison-Wesley, 2008.

[10] Barber, G., "When Nature Glows in the Dark," *Nature's Grapevine*, pp. 2-7, 2011.

[11] Fairchild, M. D., *Color Appearance Models*, 2nd ed., England John Wiley & Sons, Ltd., 2005.

[12] Dushkina, N., "Light Sources," in *Handbook of Optical Metrology*, CRC Press, pp. 3-85, 2009.

[13] Incropera, F., DeWitt, D., Bergman, T., and Lavine, A., *Fundamentals of Heat and Mass Transfer Sixth Edition*, John Wiley & Sons, 2007.

[14] Tripp, E., "Interferometric optical readout system for a MEMS infrared imaging detector," Masters Thesis, Mechanical Engineering Department, Worcester Polytechnic Institute, 2012.

[15] Hall, P., "Lenses, Prisms, and Mirrors," in *Handbook of Optical Metrology*, CRC Press, pp. 85-104, 2009.

[16] Newport Corporation. (2014) Transmittance of IR optical materials. Image. [Online]. https://www.newport.com/Optical-Materials/144943/1033/content.aspx

[17] Rogalski, A., "Progress in focal plane array technologies," *Prog. Quant. Electron.*, 36:342-473, 2012.

[18] Golay, M., "Theoretical Consideration in Heat and Infra-Red Detection, with Particular Reference to the Pneumatic Detector," *Rev. Sci. Instrum.*, 18(5):347-356, 1947.

[19] Timoshenko, S., "Analysis of Bi-metal Thermostats," *JOSA*, 11(3):233-255, 1925.

[20] Erdtmann, M., Radhakrishnan, S., Zhang, L., Liu, Y., Emelie, P., and Salerno, J., "Photomechanical Imager FPA Design for Manufacturability," in *Proc. SPIE 7660, Infrared Technology and Applications XXXVI, 766017*, vol. 7660, 2010.

[21] Salerno, J., "High Frame Rate Imaging Using Uncooled Optical Readout Photomechanical IR Sensor," in *Proc. SPIE, Infrared Technology and Applications XXXIII*, Orlando, 2007.

[22] Zhao, J., "High Sensitivity Photomechanical MW-LWIR Imaging using an Uncooled MEMS Microcantilever Array and Optical Readout," in *Proc. SPIE, Infrared Technology and Applications XXXI*, Bellingham, WA, 2005.

[23] Lavrikab, N., Archibalda, R., Rajica, D. GS., and Datskosa, P., "Uncooled MEMS IR Imagers with Optical Readout and Image Processing," in *Proc. SPIE, Infrared Technology and Applications XXXIII*, Orlando, FL, 2007.

[24] Vera-Diaz, F. A. and Doble, N., "The Human Eye and Adaptive Optics," in *Topics in Adaptive Optics*, Tyson, B., Ed., InTech, pp. 119-150, 2012.

[25] Cornsweet, T. N., *Visual Perception*, Academic Press, Inc., 1970.

[26] Open Stax College. (2013, June) Sensory Perception. [Online]. http://cnx.org/content/m46577/1.4/

[27] Schnapf, JL., Kraft, TW., and Baylor, DA., "Spectral Sensitiviy of Human Cone Receptors," *Nature*, 325:439-441, 1987.

[28] Stevens, JC. and Marks, LE., "Stevens power law in vision: exponents, intercepts, and thresholds," in *Proceedings of the Fifteenth Annual Meeting of the International Society for Psychophysics*, Tempe, AZ, pp. 87-92, 1999.

[29] Bartelson, C. J. and Breneman, E. J., "Brightness Perception In Complex Fields," *JOSA*, 57(7):953-956, 1967.

[30] Hoefflinger, B., Ed., "The Eye and High-Dynamic-Range Vision," in *High-Dynamic-Range (HDR) Vision: Microelectronics, Image Processing, Computer Graphics*, Springer, Ch. 1, pp. 1-12, 2007.

[31] Schubert, E. F., "Human eye sensitivity and photometric quantities," in *Light Emitting Diodes*, Cambride University Press, Ch. 16, pp. 275-291, 2006.

[32] Hendee, W. R. and Wells, P. NT., *The Perception of Visual Information*, Springer, 1993.

[33] Hughes, J. F., Van Dam, A., McGuire, M., Skylar, D. F., Foley, J. D., Feiner, SK., and Akeley, K., *Computer Graphics, Principles and Practice*, 3rd ed., Pearson Education, Inc., 2014.

[34] Schanda, J., Ed., *Colorimetry, Understanding the CIE system*, John Wiley & Sons, Inc., 2007.

[35] University College London, Institute of Opthalmology. (2014) Colour & Vision Research Laboratory. [Online]. http://www.cvrl.org/

[36] Lindbloom, B. (2003, April) Useful Color Equations. [Online]. http://www.brucelindbloom.com

[37] Shen, Z., "Color Differentiation in Digital Images," Master's Thesis, School of Computer Science and Mathematics, Victoria University of Technology, 2003.

[38] Luo, M. R., Minchew, C., Kenyon, P., and Cui, G., "Verification of CIEDE2000 using industrial data," in *AIC 2004 Color and Paints, Interim Meeting of the International Color Association*, Porto Alegre, Brazil, pp. 97-102, 2004.

[39] Page, D., "Interferometry," in *Handbook of Optical Metrology*, CRC Press, pp. 191-217, 2009.

[40] Cloud, G., *Optical Methods of Engineering Analysis*, Cambridge University Press, 1995.

[41] Pedrini, G., "Holography," in *Handbook of Optical Metrology*, CRC Press, pp. 219-240, 2009.

[42] Dobrev, I., Khaleghi, M., Cao, Z., Pantuso, F., and Furlong, C., "Realization of an uncooled MEMS sensor for real-time infrared imaging," in *SEM Annual Conference & Exposition on Experimental and Applied Mechanics*, Chicago, IL, 2013.

[43] Lang, W., "Nomarski differential interference-contrast microscopy," *Zeiss Information*, vol. 71, pp. 12-16, 1969.

[44] Fgalore. (2014) Wollaston Prism. Image. [Online]. http://en.wikipedia.org/wiki/Wollaston_prism#mediaviewer/File:Wollaston-prism.svg

[45] Pluta, M. and Szyjer, M., "Nomarski's DIC microscopy: a review," in *Proc. SPIE 1846, Phase Contrast and Differential Interference Contrast Imaging Techniques and Applications*, Warsaw, pp. 10-25, 1994.

[46] Nelson, S. A. (2013) Earth & Environmental Sciences 2110, Mineralogy. [Online]. http://www.tulane.edu/~sanelson/eens211/

[47] Sørensen, B. E., "A revised Michel-Levy interference colour chart based on first-principles," *Eur. J. Mineral.*, 25:5-10, 2013.

[48] Pascale, D. (2003) A Review of RGB Color Spaces. from xyY to R'G'B'. [Online]. http://www.babelcolor.com/download/A%20review%20of%20RGB%20color%20spaces.pdf

[49] Huynh, D. (2010) Function xyz2lab. Matlab Function. [Online]. http://www.csse.uwa.edu.au/~du/Software/graphics/xyz2lab.m

[50] Sharma, G., Wu, W., and Dalal, E. N., "The CIEDE2000 Color-Difference Formula: Implementation Notes, Supplementary Test Data, and Mathematical Observations," *Color Res. Appl.*, 30:21-30, 2005.

[51] Sharma, G. (2004) Function deltaE2000. Matlab Function. [Online]. http://www.ece.rochester.edu/~gsharma/ciede2000/dataNprograms/deltaE2000.m

[52] Ghinea, R., Perez, M. M., Herrera, L. J., Rivas, M. J., Yebra, A., and Paravina, R. D., "Color difference thresholds in dental ceramics," *J. Dent.*, 38:e57-e64, 2010.

[53] Toal, V., *Introduction to Holography*, CRC Press, 2012.

[54] Thorlabs Inc. (2014) Mounted High-Power LEDs. [Online]. http://www.thorlabs.com/images/tabimages/High-Power_LED_Spectra_MxxxLx-Scaled.xlsx

[55] Molecular Expressions, Florida State University, and Nikon Inc. (2014) de Sénarmont Bias Retardation in DIC Microscopy. [Online]. http://www.microscopyu.com/articles/dic/desenarmontdicintro.html

[56] Allied Vision Technologies. (2014) Pike F-100. [Online]. http://www.alliedvisiontec.com/us/products/cameras/firewire/pike/f-100bc.html

[57] Total Turnkey Solutions. (2014) PL-A780 Series (PL-A781, PL-A782). [Online]. http://www.turnkey-solutions.com.au/cam_pixelink_pla782_series.htm

[58] Edmund Optics Inc. (2014) 1.0X Gold Series Telecentric Lens (2/3" Series). [Online]. http://www.edmundoptics.com/imaging/imaging-lenses/techspec-lenses/gold-series-focusable-telecentric-lenses/55350

[59] Thorlabs, Inc. (2014) Non-Polarizing Beamsplitter Cubes in 30 mm Cage Cubes. [Online]. http://www.thorlabs.com/newgrouppage9.cfm?objectgroup_id=4129

[60] Thorlabs, Inc. (2014) N-BK7 Mounted Spherical Singlet Lens Kits. [Online]. http://www.thorlabs.com/newgrouppage9.cfm?objectgroup_id=688

[61] Thorlabs, Inc. (2014) High-Power LED Driver with Pulse Modulation. [Online]. http://www.thorlabs.com/newgrouppage9.cfm?objectgroup_id=4003

[62] Thorlabs, Inc. (2014) Mounted High-Power LEDs. [Online]. http://www.thorlabs.com/newgrouppage9.cfm?objectgroup_id=2692

[63] Harrington, E., Dobrev, I., Bapat, N., Flores, J. M., Furlong, C., Rosowski, J., Cheng, J. T., Scarpino, C., and Ravicz, M., "Development of an optoelectronic holographic platform for otolaryngology applications," in *Proc. SPIE 7791, Interferometry XV: Applications, 77910J*, San Diago, CA, 2010.

[64] FLIR Systems, Inc. (2009) How is NEDT measured? [Online]. http://flir.custhelp.com/app/answers/detail/a_id/128/~/how-is-nedt-measured%3F

[65] Santa Barbara Infrared, Inc. (2009) Infinity Differential Blackbody (DB Series). [Online]. http://www.sbir.com/blackbody_db.asp

[66] PixeLINK. (2014) PixeLINK Capture OEM. Image capture application. [Online]. http://www.pixelink.com/products/software-and-accessories/pixelink-capture-oem.aspx

[67] Fairchild, M. D., Wyble, D. R., and Johnson, G. M., "Matching image color from different cameras," in *SPIE 6808, Image Quality and System Performance V, 68080E*, San Jose, CA, 2008.

Appendix A: CIE XYZ 2-deg CMFs Transformed from the CIE (2006) 2-deg LMS Cone Fundamentals

A plot of the color matching functions (CMFs) used for this work can be seen below in Figure A-1.

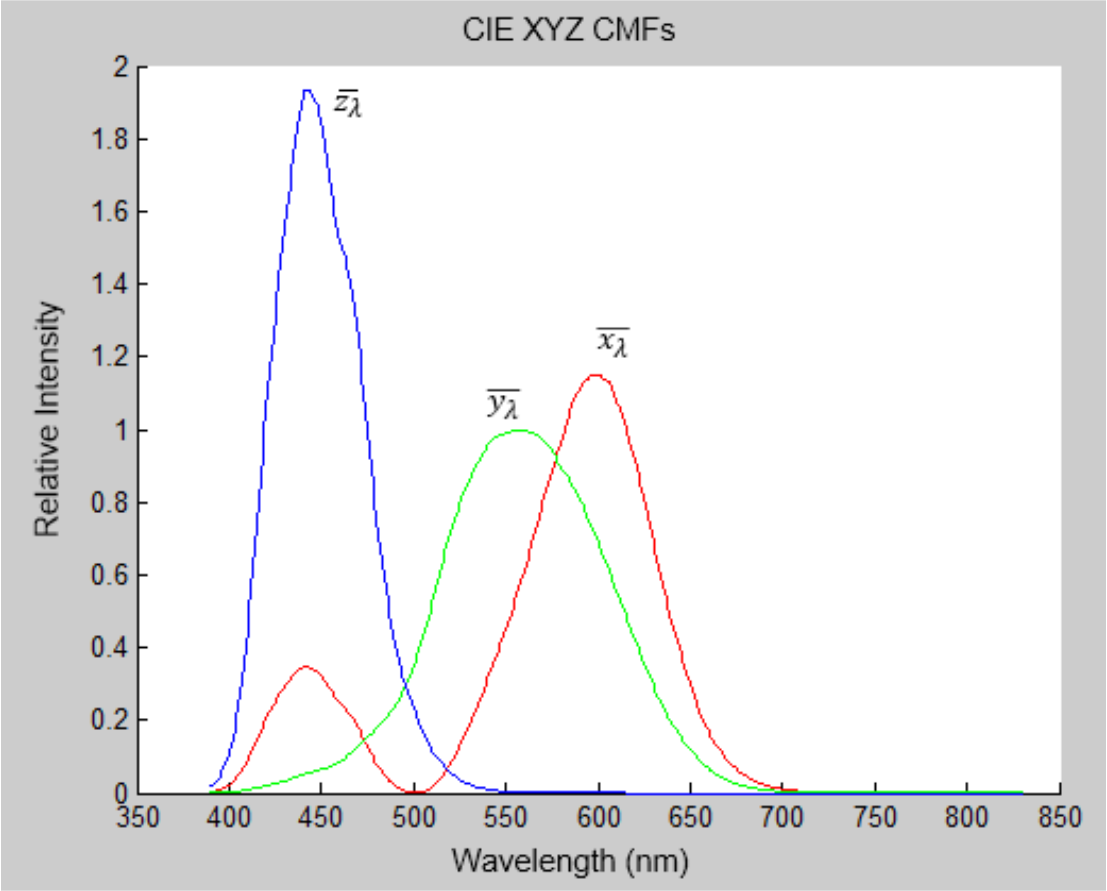

Figure A-1 Plot of 2-deg XYZ CMFs transformed from the CIE (2006) 2-deg LMS cone fundamentals

The CMFs consist of 441 lines of data, corresponding to the x, y, and z tristimulus values for wavelengths from 390 nm to 830 nm in 1 nm increments. These data were retrieved

online from the University College London, Institute of Opthalmology, Colour & Vision Research Laboratory website located at http://www.cvrl.org/, and are presented here in tabular form in order to aid in the reproduction of the results presented in this work.

Wavelength, λ (nm)	Color Matching Functions		
	X	Y	Z
390	3.77E-03	4.15E-04	1.85E-02
391	4.53E-03	5.03E-04	2.22E-02
392	5.45E-03	6.08E-04	2.67E-02
393	6.54E-03	7.34E-04	3.21E-02
394	7.84E-03	8.84E-04	3.85E-02
395	9.38E-03	1.06E-03	4.61E-02
396	1.12E-02	1.27E-03	5.51E-02
397	1.33E-02	1.50E-03	6.58E-02
398	1.59E-02	1.78E-03	7.82E-02
399	1.88E-02	2.10E-03	9.28E-02
400	2.21E-02	2.45E-03	1.10E-01
401	2.60E-02	2.85E-03	1.29E-01
402	3.04E-02	3.30E-03	1.51E-01
403	3.54E-02	3.80E-03	1.76E-01
404	4.11E-02	4.35E-03	2.05E-01
405	4.74E-02	4.97E-03	2.37E-01
406	5.45E-02	5.66E-03	2.73E-01
407	6.22E-02	6.42E-03	3.12E-01
408	7.07E-02	7.25E-03	3.55E-01
409	7.98E-02	8.14E-03	4.01E-01
410	8.95E-02	9.08E-03	4.51E-01
411	9.97E-02	1.01E-02	5.03E-01
412	1.10E-01	1.11E-02	5.59E-01
413	1.21E-01	1.21E-02	6.16E-01
414	1.33E-01	1.32E-02	6.76E-01
415	1.45E-01	1.43E-02	7.38E-01
416	1.57E-01	1.55E-02	8.01E-01
417	1.69E-01	1.66E-02	8.66E-01
418	1.81E-01	1.79E-02	9.30E-01
419	1.93E-01	1.91E-02	9.92E-01
420	2.04E-01	2.03E-02	1.05E+00
421	2.14E-01	2.14E-02	1.11E+00
422	2.23E-01	2.26E-02	1.16E+00
423	2.32E-01	2.37E-02	1.21E+00
424	2.40E-01	2.49E-02	1.26E+00
425	2.49E-01	2.61E-02	1.31E+00
426	2.58E-01	2.74E-02	1.35E+00
427	2.66E-01	2.87E-02	1.41E+00
428	2.75E-01	3.02E-02	1.46E+00
429	2.84E-01	3.17E-02	1.51E+00
430	2.92E-01	3.32E-02	1.55E+00
431	2.99E-01	3.48E-02	1.60E+00
432	3.05E-01	3.64E-02	1.64E+00
433	3.11E-01	3.81E-02	1.67E+00
434	3.17E-01	3.98E-02	1.71E+00
435	3.23E-01	4.16E-02	1.75E+00
436	3.29E-01	4.34E-02	1.79E+00
437	3.35E-01	4.52E-02	1.83E+00
438	3.41E-01	4.70E-02	1.86E+00
439	3.45E-01	4.87E-02	1.89E+00
440	3.48E-01	5.03E-02	1.92E+00
441	3.49E-01	5.19E-02	1.93E+00
442	3.49E-01	5.33E-02	1.93E+00
443	3.47E-01	5.47E-02	1.93E+00
444	3.45E-01	5.61E-02	1.93E+00
445	3.42E-01	5.74E-02	1.92E+00
446	3.39E-01	5.89E-02	1.91E+00
447	3.36E-01	6.03E-02	1.90E+00

448	3.32E-01	6.18E-02	1.89E+00	487	3.45E-02	2.18E-01	4.95E-01
449	3.28E-01	6.33E-02	1.87E+00	488	2.95E-02	2.24E-01	4.64E-01
450	3.22E-01	6.47E-02	1.85E+00	489	2.49E-02	2.31E-01	4.36E-01
451	3.16E-01	6.61E-02	1.82E+00	490	2.08E-02	2.38E-01	4.10E-01
452	3.08E-01	6.76E-02	1.78E+00	491	1.72E-02	2.46E-01	3.86E-01
453	2.99E-01	6.90E-02	1.74E+00	492	1.41E-02	2.55E-01	3.65E-01
454	2.91E-01	7.06E-02	1.70E+00	493	1.13E-02	2.64E-01	3.45E-01
455	2.83E-01	7.24E-02	1.66E+00	494	9.02E-03	2.74E-01	3.27E-01
456	2.75E-01	7.44E-02	1.63E+00	495	7.10E-03	2.85E-01	3.11E-01
457	2.67E-01	7.66E-02	1.60E+00	496	5.57E-03	2.96E-01	2.95E-01
458	2.61E-01	7.91E-02	1.57E+00	497	4.39E-03	3.09E-01	2.80E-01
459	2.54E-01	8.20E-02	1.54E+00	498	3.52E-03	3.21E-01	2.65E-01
460	2.49E-01	8.51E-02	1.52E+00	499	2.89E-03	3.34E-01	2.51E-01
461	2.43E-01	8.87E-02	1.50E+00	500	2.46E-03	3.48E-01	2.38E-01
462	2.38E-01	9.27E-02	1.49E+00	501	2.21E-03	3.63E-01	2.24E-01
463	2.33E-01	9.69E-02	1.47E+00	502	2.15E-03	3.78E-01	2.11E-01
464	2.28E-01	1.01E-01	1.45E+00	503	2.34E-03	3.94E-01	1.98E-01
465	2.22E-01	1.06E-01	1.43E+00	504	2.82E-03	4.11E-01	1.85E-01
466	2.15E-01	1.11E-01	1.40E+00	505	3.65E-03	4.28E-01	1.72E-01
467	2.08E-01	1.16E-01	1.37E+00	506	4.89E-03	4.45E-01	1.60E-01
468	1.99E-01	1.20E-01	1.33E+00	507	6.63E-03	4.64E-01	1.48E-01
469	1.90E-01	1.25E-01	1.29E+00	508	8.94E-03	4.82E-01	1.37E-01
470	1.81E-01	1.30E-01	1.25E+00	509	1.19E-02	5.01E-01	1.27E-01
471	1.71E-01	1.35E-01	1.20E+00	510	1.56E-02	5.20E-01	1.18E-01
472	1.60E-01	1.39E-01	1.15E+00	511	2.00E-02	5.40E-01	1.09E-01
473	1.50E-01	1.44E-01	1.10E+00	512	2.50E-02	5.60E-01	1.02E-01
474	1.40E-01	1.49E-01	1.05E+00	513	3.07E-02	5.80E-01	9.53E-02
475	1.29E-01	1.54E-01	9.99E-01	514	3.67E-02	6.00E-01	8.89E-02
476	1.19E-01	1.58E-01	9.47E-01	515	4.32E-02	6.21E-01	8.28E-02
477	1.09E-01	1.63E-01	8.97E-01	516	4.98E-02	6.41E-01	7.70E-02
478	9.95E-02	1.68E-01	8.47E-01	517	5.67E-02	6.61E-01	7.14E-02
479	9.04E-02	1.74E-01	8.00E-01	518	6.39E-02	6.81E-01	6.62E-02
480	8.18E-02	1.79E-01	7.55E-01	519	7.15E-02	7.00E-01	6.12E-02
481	7.38E-02	1.84E-01	7.13E-01	520	7.96E-02	7.18E-01	5.65E-02
482	6.62E-02	1.90E-01	6.73E-01	521	8.82E-02	7.35E-01	5.22E-02
483	5.91E-02	1.95E-01	6.34E-01	522	9.73E-02	7.51E-01	4.81E-02
484	5.23E-02	2.01E-01	5.97E-01	523	1.07E-01	7.66E-01	4.43E-02
485	4.60E-02	2.06E-01	5.62E-01	524	1.17E-01	7.81E-01	4.08E-02
486	4.01E-02	2.12E-01	5.27E-01	525	1.27E-01	7.95E-01	3.75E-02

526	1.37E-01	8.08E-01	3.45E-02	565	7.02E-01	9.90E-01	8.82E-04
527	1.48E-01	8.21E-01	3.16E-02	566	7.20E-01	9.88E-01	8.01E-04
528	1.59E-01	8.34E-01	2.90E-02	567	7.39E-01	9.85E-01	7.27E-04
529	1.71E-01	8.46E-01	2.66E-02	568	7.59E-01	9.82E-01	6.61E-04
530	1.82E-01	8.58E-01	2.44E-02	569	7.78E-01	9.78E-01	6.00E-04
531	1.93E-01	8.68E-01	2.23E-02	570	7.97E-01	9.73E-01	5.45E-04
532	2.05E-01	8.78E-01	2.05E-02	571	8.15E-01	9.68E-01	4.95E-04
533	2.16E-01	8.88E-01	1.87E-02	572	8.34E-01	9.63E-01	4.50E-04
534	2.28E-01	8.98E-01	1.71E-02	573	8.52E-01	9.57E-01	4.09E-04
535	2.41E-01	9.07E-01	1.57E-02	574	8.69E-01	9.50E-01	3.72E-04
536	2.54E-01	9.17E-01	1.43E-02	575	8.85E-01	9.42E-01	3.39E-04
537	2.67E-01	9.27E-01	1.30E-02	576	9.01E-01	9.34E-01	3.08E-04
538	2.81E-01	9.37E-01	1.19E-02	577	9.17E-01	9.24E-01	2.80E-04
539	2.95E-01	9.46E-01	1.08E-02	578	9.32E-01	9.15E-01	2.55E-04
540	3.10E-01	9.54E-01	9.85E-03	579	9.47E-01	9.05E-01	2.32E-04
541	3.24E-01	9.62E-01	8.96E-03	580	9.64E-01	8.96E-01	2.12E-04
542	3.38E-01	9.68E-01	8.15E-03	581	9.81E-01	8.88E-01	1.93E-04
543	3.53E-01	9.74E-01	7.42E-03	582	9.99E-01	8.81E-01	1.76E-04
544	3.67E-01	9.78E-01	6.74E-03	583	1.02E+00	8.74E-01	1.60E-04
545	3.80E-01	9.81E-01	6.13E-03	584	1.03E+00	8.66E-01	1.46E-04
546	3.94E-01	9.84E-01	5.57E-03	585	1.05E+00	8.59E-01	1.34E-04
547	4.08E-01	9.85E-01	5.06E-03	586	1.07E+00	8.50E-01	1.22E-04
548	4.21E-01	9.86E-01	4.60E-03	587	1.08E+00	8.42E-01	1.11E-04
549	4.35E-01	9.88E-01	4.18E-03	588	1.09E+00	8.32E-01	1.02E-04
550	4.49E-01	9.89E-01	3.79E-03	589	1.10E+00	8.22E-01	9.29E-05
551	4.64E-01	9.91E-01	3.44E-03	590	1.11E+00	8.12E-01	8.49E-05
552	4.79E-01	9.93E-01	3.12E-03	591	1.12E+00	8.01E-01	7.77E-05
553	4.95E-01	9.96E-01	2.83E-03	592	1.13E+00	7.90E-01	7.11E-05
554	5.11E-01	9.98E-01	2.57E-03	593	1.13E+00	7.78E-01	6.51E-05
555	5.28E-01	9.99E-01	2.33E-03	594	1.14E+00	7.66E-01	5.96E-05
556	5.45E-01	1.00E+00	2.11E-03	595	1.14E+00	7.54E-01	5.46E-05
557	5.62E-01	1.00E+00	1.92E-03	596	1.15E+00	7.42E-01	5.01E-05
558	5.79E-01	9.99E-01	1.74E-03	597	1.15E+00	7.30E-01	4.59E-05
559	5.96E-01	9.98E-01	1.58E-03	598	1.15E+00	7.17E-01	4.21E-05
560	6.13E-01	9.97E-01	1.43E-03	599	1.15E+00	7.05E-01	3.87E-05
561	6.31E-01	9.96E-01	1.30E-03	600	1.15E+00	6.92E-01	3.55E-05
562	6.48E-01	9.95E-01	1.18E-03	601	1.15E+00	6.79E-01	3.26E-05
563	6.65E-01	9.94E-01	1.07E-03	602	1.15E+00	6.66E-01	3.00E-05
564	6.83E-01	9.92E-01	9.72E-04	603	1.14E+00	6.53E-01	2.76E-05

604	1.14E+00	6.40E-01	2.54E-05	643	4.19E-01	1.70E-01	0.00E+00
605	1.13E+00	6.27E-01	2.33E-05	644	4.02E-01	1.62E-01	0.00E+00
606	1.13E+00	6.14E-01	2.15E-05	645	3.84E-01	1.55E-01	0.00E+00
607	1.12E+00	6.00E-01	1.98E-05	646	3.67E-01	1.47E-01	0.00E+00
608	1.11E+00	5.86E-01	1.83E-05	647	3.50E-01	1.40E-01	0.00E+00
609	1.10E+00	5.72E-01	1.68E-05	648	3.33E-01	1.33E-01	0.00E+00
610	1.08E+00	5.58E-01	1.55E-05	649	3.16E-01	1.26E-01	0.00E+00
611	1.07E+00	5.45E-01	1.44E-05	650	3.00E-01	1.19E-01	0.00E+00
612	1.06E+00	5.31E-01	1.33E-05	651	2.84E-01	1.13E-01	0.00E+00
613	1.04E+00	5.17E-01	1.23E-05	652	2.69E-01	1.07E-01	0.00E+00
614	1.02E+00	5.03E-01	1.13E-05	653	2.55E-01	1.01E-01	0.00E+00
615	1.01E+00	4.90E-01	1.05E-05	654	2.41E-01	9.52E-02	0.00E+00
616	9.90E-01	4.76E-01	0.00E+00	655	2.28E-01	8.98E-02	0.00E+00
617	9.71E-01	4.62E-01	0.00E+00	656	2.15E-01	8.47E-02	0.00E+00
618	9.52E-01	4.49E-01	0.00E+00	657	2.03E-01	7.98E-02	0.00E+00
619	9.33E-01	4.36E-01	0.00E+00	658	1.92E-01	7.52E-02	0.00E+00
620	9.14E-01	4.23E-01	0.00E+00	659	1.81E-01	7.09E-02	0.00E+00
621	8.95E-01	4.10E-01	0.00E+00	660	1.71E-01	6.67E-02	0.00E+00
622	8.76E-01	3.98E-01	0.00E+00	661	1.61E-01	6.28E-02	0.00E+00
623	8.56E-01	3.86E-01	0.00E+00	662	1.52E-01	5.90E-02	0.00E+00
624	8.35E-01	3.73E-01	0.00E+00	663	1.43E-01	5.55E-02	0.00E+00
625	8.14E-01	3.61E-01	0.00E+00	664	1.34E-01	5.22E-02	0.00E+00
626	7.90E-01	3.48E-01	0.00E+00	665	1.26E-01	4.90E-02	0.00E+00
627	7.66E-01	3.36E-01	0.00E+00	666	1.19E-01	4.60E-02	0.00E+00
628	7.42E-01	3.23E-01	0.00E+00	667	1.12E-01	4.32E-02	0.00E+00
629	7.17E-01	3.10E-01	0.00E+00	668	1.05E-01	4.05E-02	0.00E+00
630	6.92E-01	2.98E-01	0.00E+00	669	9.83E-02	3.80E-02	0.00E+00
631	6.68E-01	2.86E-01	0.00E+00	670	9.22E-02	3.56E-02	0.00E+00
632	6.44E-01	2.74E-01	0.00E+00	671	8.65E-02	3.33E-02	0.00E+00
633	6.21E-01	2.63E-01	0.00E+00	672	8.10E-02	3.12E-02	0.00E+00
634	5.98E-01	2.52E-01	0.00E+00	673	7.59E-02	2.92E-02	0.00E+00
635	5.76E-01	2.42E-01	0.00E+00	674	7.10E-02	2.73E-02	0.00E+00
636	5.54E-01	2.31E-01	0.00E+00	675	6.64E-02	2.55E-02	0.00E+00
637	5.33E-01	2.22E-01	0.00E+00	676	6.21E-02	2.39E-02	0.00E+00
638	5.12E-01	2.12E-01	0.00E+00	677	5.80E-02	2.23E-02	0.00E+00
639	4.92E-01	2.03E-01	0.00E+00	678	5.41E-02	2.08E-02	0.00E+00
640	4.73E-01	1.94E-01	0.00E+00	679	5.05E-02	1.94E-02	0.00E+00
641	4.55E-01	1.86E-01	0.00E+00	680	4.71E-02	1.81E-02	0.00E+00
642	4.37E-01	1.78E-01	0.00E+00	681	4.39E-02	1.68E-02	0.00E+00

682	4.09E-02	1.57E-02	0.00E+00	721	2.29E-03	8.78E-04	0.00E+00
683	3.81E-02	1.46E-02	0.00E+00	722	2.13E-03	8.15E-04	0.00E+00
684	3.54E-02	1.36E-02	0.00E+00	723	1.97E-03	7.57E-04	0.00E+00
685	3.29E-02	1.26E-02	0.00E+00	724	1.83E-03	7.03E-04	0.00E+00
686	3.06E-02	1.17E-02	0.00E+00	725	1.70E-03	6.54E-04	0.00E+00
687	2.83E-02	1.09E-02	0.00E+00	726	1.58E-03	6.08E-04	0.00E+00
688	2.63E-02	1.01E-02	0.00E+00	727	1.47E-03	5.65E-04	0.00E+00
689	2.44E-02	9.33E-03	0.00E+00	728	1.37E-03	5.26E-04	0.00E+00
690	2.26E-02	8.66E-03	0.00E+00	729	1.27E-03	4.90E-04	0.00E+00
691	2.10E-02	8.05E-03	0.00E+00	730	1.19E-03	4.56E-04	0.00E+00
692	1.95E-02	7.48E-03	0.00E+00	731	1.10E-03	4.24E-04	0.00E+00
693	1.82E-02	6.96E-03	0.00E+00	732	1.03E-03	3.95E-04	0.00E+00
694	1.69E-02	6.48E-03	0.00E+00	733	9.56E-04	3.67E-04	0.00E+00
695	1.58E-02	6.03E-03	0.00E+00	734	8.89E-04	3.42E-04	0.00E+00
696	1.47E-02	5.61E-03	0.00E+00	735	8.27E-04	3.18E-04	0.00E+00
697	1.36E-02	5.22E-03	0.00E+00	736	7.69E-04	2.96E-04	0.00E+00
698	1.27E-02	4.85E-03	0.00E+00	737	7.15E-04	2.75E-04	0.00E+00
699	1.18E-02	4.51E-03	0.00E+00	738	6.65E-04	2.56E-04	0.00E+00
700	1.10E-02	4.20E-03	0.00E+00	739	6.19E-04	2.38E-04	0.00E+00
701	1.02E-02	3.90E-03	0.00E+00	740	5.76E-04	2.22E-04	0.00E+00
702	9.48E-03	3.63E-03	0.00E+00	741	5.37E-04	2.07E-04	0.00E+00
703	8.82E-03	3.37E-03	0.00E+00	742	5.00E-04	1.93E-04	0.00E+00
704	8.19E-03	3.13E-03	0.00E+00	743	4.67E-04	1.80E-04	0.00E+00
705	7.61E-03	2.91E-03	0.00E+00	744	4.35E-04	1.68E-04	0.00E+00
706	7.06E-03	2.70E-03	0.00E+00	745	4.06E-04	1.57E-04	0.00E+00
707	6.55E-03	2.51E-03	0.00E+00	746	3.78E-04	1.46E-04	0.00E+00
708	6.07E-03	2.32E-03	0.00E+00	747	3.53E-04	1.36E-04	0.00E+00
709	5.63E-03	2.15E-03	0.00E+00	748	3.29E-04	1.27E-04	0.00E+00
710	5.21E-03	2.00E-03	0.00E+00	749	3.06E-04	1.18E-04	0.00E+00
711	4.83E-03	1.85E-03	0.00E+00	750	2.86E-04	1.10E-04	0.00E+00
712	4.48E-03	1.71E-03	0.00E+00	751	2.66E-04	1.03E-04	0.00E+00
713	4.15E-03	1.59E-03	0.00E+00	752	2.49E-04	9.61E-05	0.00E+00
714	3.85E-03	1.47E-03	0.00E+00	753	2.32E-04	8.97E-05	0.00E+00
715	3.57E-03	1.37E-03	0.00E+00	754	2.17E-04	8.38E-05	0.00E+00
716	3.31E-03	1.27E-03	0.00E+00	755	2.02E-04	7.83E-05	0.00E+00
717	3.08E-03	1.18E-03	0.00E+00	756	1.89E-04	7.31E-05	0.00E+00
718	2.86E-03	1.09E-03	0.00E+00	757	1.76E-04	6.83E-05	0.00E+00
719	2.65E-03	1.02E-03	0.00E+00	758	1.65E-04	6.39E-05	0.00E+00
720	2.46E-03	9.45E-04	0.00E+00	759	1.54E-04	5.97E-05	0.00E+00

760	1.44E-04	5.58E-05	0.00E+00
761	1.34E-04	5.21E-05	0.00E+00
762	1.26E-04	4.87E-05	0.00E+00
763	1.17E-04	4.55E-05	0.00E+00
764	1.10E-04	4.26E-05	0.00E+00
765	1.02E-04	3.98E-05	0.00E+00
766	9.58E-05	3.73E-05	0.00E+00
767	8.97E-05	3.49E-05	0.00E+00
768	8.39E-05	3.26E-05	0.00E+00
769	7.85E-05	3.06E-05	0.00E+00
770	7.35E-05	2.86E-05	0.00E+00
771	6.87E-05	2.68E-05	0.00E+00
772	6.43E-05	2.50E-05	0.00E+00
773	6.01E-05	2.34E-05	0.00E+00
774	5.62E-05	2.19E-05	0.00E+00
775	5.26E-05	2.05E-05	0.00E+00
776	4.93E-05	1.92E-05	0.00E+00
777	4.62E-05	1.80E-05	0.00E+00
778	4.33E-05	1.69E-05	0.00E+00
779	4.06E-05	1.59E-05	0.00E+00
780	3.81E-05	1.49E-05	0.00E+00
781	3.57E-05	1.40E-05	0.00E+00
782	3.35E-05	1.31E-05	0.00E+00
783	3.14E-05	1.23E-05	0.00E+00
784	2.94E-05	1.15E-05	0.00E+00
785	2.76E-05	1.08E-05	0.00E+00
786	2.59E-05	1.01E-05	0.00E+00
787	2.43E-05	9.51E-06	0.00E+00
788	2.28E-05	8.93E-06	0.00E+00
789	2.14E-05	8.38E-06	0.00E+00
790	2.00E-05	7.86E-06	0.00E+00
791	1.88E-05	7.38E-06	0.00E+00
792	1.76E-05	6.93E-06	0.00E+00
793	1.66E-05	6.51E-06	0.00E+00
794	1.55E-05	6.11E-06	0.00E+00
795	1.46E-05	5.74E-06	0.00E+00
796	1.37E-05	5.39E-06	0.00E+00
797	1.29E-05	5.07E-06	0.00E+00
798	1.21E-05	4.76E-06	0.00E+00
799	1.14E-05	4.48E-06	0.00E+00
800	1.07E-05	4.21E-06	0.00E+00
801	1.00E-05	3.96E-06	0.00E+00
802	9.45E-06	3.73E-06	0.00E+00
803	8.88E-06	3.51E-06	0.00E+00
804	8.36E-06	3.30E-06	0.00E+00
805	7.86E-06	3.11E-06	0.00E+00
806	7.39E-06	2.92E-06	0.00E+00
807	6.94E-06	2.75E-06	0.00E+00
808	6.53E-06	2.58E-06	0.00E+00
809	6.14E-06	2.43E-06	0.00E+00
810	5.77E-06	2.29E-06	0.00E+00
811	5.43E-06	2.15E-06	0.00E+00
812	5.10E-06	2.03E-06	0.00E+00
813	4.80E-06	1.91E-06	0.00E+00
814	4.52E-06	1.80E-06	0.00E+00
815	4.26E-06	1.69E-06	0.00E+00
816	4.01E-06	1.60E-06	0.00E+00
817	3.78E-06	1.50E-06	0.00E+00
818	3.56E-06	1.42E-06	0.00E+00
819	3.36E-06	1.34E-06	0.00E+00
820	3.17E-06	1.26E-06	0.00E+00
821	2.99E-06	1.19E-06	0.00E+00
822	2.81E-06	1.12E-06	0.00E+00
823	2.65E-06	1.06E-06	0.00E+00
824	2.50E-06	9.99E-07	0.00E+00
825	2.36E-06	9.42E-07	0.00E+00
826	2.22E-06	8.89E-07	0.00E+00
827	2.10E-06	8.39E-07	0.00E+00
828	1.98E-06	7.91E-07	0.00E+00
829	1.87E-06	7.47E-07	0.00E+00
830	1.76E-06	7.05E-07	0.00E+00

Appendix B: CIE XYZ to CIELAB Conversion Function

The implementation of the CIEXYZ to CIELAB transformation formulas that was used for this work was obtained online from the School of Computer Science and Software Engineering at The University of Southern Australia as shown below [**49**].

```
function LAB = xyz2lab(XYZ)

%XYZ2LAB converts an image from XYZ format to CIE-L*a*b*
%
%LAB = xyz2LAB(XYZ)
%
%Input parameter: XYZ must be an image having 3 channels, i.e.  a 3D
array.
%Output parameter: LAB would be an image of the same dimension.
%
%The XYZ format is often used as an intermediate format for conversion
from
%RGB to L*a*b* and vice versa.
%
%Example: To convert an image in RGB format to L*a*b* format, one can
%combine the calling to the rgb2xyz and xyz2lab functions:
%   rgbim = imread('yourImage.png');  % image in RGB format
%   labim = xyz2lab(rgb2xyz(rgbim));
%The output labim has the following ranges of values:
%  - first channel L*       0..100
%  - the second channel a*  -128..127
%  - the third channel b*   -128..127
%
%Other software packages, e.g.  OpenCV, often applies a normalisation
%process so that images in the L*a*b* format can be stored as 3-channel
%greyscale images.  The normalisation adopted by OpenCV is:
%  - the first channel L* is rescaled to the range 0..255.  This can be
done
%    easily by multiplying by 255 and dividing by 100.
%  - the second channel a* and third channel b* are added by 128 to
bring
%    the range from -128..127 to 0..255.
%
%When comparing the pixel values of an L*a*b* image produced by the
Matlab
```

```
%function here and those from OpenCV, ensure that the above
normalisation
%procedure is taken into account.
%
%Also noted that images that are read from disk into OpenCV have their
%channels specified in reverse order in the data structure.  So, to
compare
%the Matlab function here with those in OpenCV, use the following
OpenCV
%functions:
%   source_rgb_image = cvLoadImage('yourImage.png', 1);
%   // make sure that the 3rd parameter is CV_BGR2Lab and not
CV_RGB2Lab
%   cvCvtColor(source_rgb_image, destination_lab_image, CV_BGR2Lab);
%   // the resultant L*a*b* image is created within the program (i.e.
not
%   // read from disk), so the channels are in the right order:
%   cvCvtPixToPlane(destination_lab_image, l_channel, a_channel,
b_channel,
%                   0);
%
%References:
%* http://www.easyrgb.com/index.php?X=MATH
%* http://en.wikipedia.org/wiki/SRGB_color_space
%
%SEE ALSO
%  lab2xyz, xyz2rgb, rgb2xyz
%
%Feb 2010
%
%Copyright Du Huynh
%School of Computer Science and Software Engineering
%The University of Western Australia

%ref_X =  95.047   Observer= 2Â°, Illuminant= D65
%ref_Y = 100.000
%ref_Z = 108.883

ref_XYZ = [95.047; 100.000; 108.883];

for i=1:3
    XYZ(:,:,i) = XYZ(:,:,i) / ref_XYZ(i);
end

index1 = find(XYZ > 0.008856);
index2 = find(XYZ <= 0.008856);
```

```
XYZ(index1) = XYZ(index1).^(1/3);
XYZ(index2) = (7.787 * XYZ(index2) ) + ( 16 / 116 );

% CIE-L*a*b*
LAB = zeros(size(XYZ));
LAB(:,:,1) = ( 116 * XYZ(:,:,2) ) - 16;
LAB(:,:,2) = 500 * ( XYZ(:,:,1) - XYZ(:,:,2) );
LAB(:,:,3) = 200 * ( XYZ(:,:,2) - XYZ(:,:,3) );
end
```

Appendix C: CIEDE2000 from CIELAB Calculation Function

The specific Matlab implementation of the CIEDE2000 color difference formulas that was used for this work was obtained online from the School of Engineering & Applied Sciences, Electrical & Computer Engineering Department, University of Rochester, as shown below [**51**].

```
function de00 = deltaE2000(Labstd,Labsample, KLCH)
%function de00 = deltaE2000(Labstd,Labsample, KLCH)
% Compute the CIEDE2000 color-difference between the sample between a
reference
% with CIELab coordinates Labsample and a standard with CIELab
coordinates
% Labstd
% The function works on multiple standard and sample vectors too
% provided Labstd and Labsample are K x 3 matrices with samples and
% standard specification in corresponding rows of Labstd and Labsample
% The optional argument KLCH is a 1x3 vector containing the
% the value of the parametric weighting factors kL, kC, and kH
% these default to 1 if KLCH is not specified.

% Based on the article:
% "The CIEDE2000 Color-Difference Formula: Implementation Notes,
% Supplementary Test Data, and Mathematical Observations,", G.  Sharma,
% W.  Wu, E.  N.  Dalal, submitted to Color Research and Application,
% January 2004.
% available at http://www.ece.rochester.edu/~/gsharma/ciede2000/

de00 = [];

% Error checking to ensure that sample and Std vectors are of correct
sizes
v=size(Labstd); w = size(Labsample);
if ( v(1) ~= w(1) | v(2) ~= w(2) )
  disp('deltaE00: Standard and Sample sizes do not match');
  return
end % if ( v(1) ~= w(1) | v(2) ~= w(2) )
if ( v(2) ~= 3)
  disp('deltaE00: Standard and Sample Lab vectors should be Kx3
vectors');
```

```
  return
end

% Parametric factors
if (nargin <3 )
     % Values of Parametric factors not specified use defaults
     kl = 1; kc=1; kh =1;
else
     % Use specified Values of Parametric factors
     if ( (size(KLCH,1) ~=1) | (size(KLCH,2) ~=3))
       disp('deltaE00: KLCH must be a 1x3  vector');
       return;
    else
       kl =KLCH(1); kc=KLCH(2); kh =KLCH(3);
     end
end

Lstd = Labstd(:,1)';
astd = Labstd(:,2)';
bstd = Labstd(:,3)';
Cabstd = sqrt(astd.^2+bstd.^2);

Lsample = Labsample(:,1)';
asample = Labsample(:,2)';
bsample = Labsample(:,3)';
Cabsample = sqrt(asample.^2+bsample.^2);

Cabarithmean = (Cabstd + Cabsample)/2;

G = 0.5* ( 1 - sqrt( (Cabarithmean.^7)./(Cabarithmean.^7 + 25^7)));

apstd = (1+G).*astd; % aprime in paper
apsample = (1+G).*asample; % aprime in paper
Cpsample = sqrt(apsample.^2+bsample.^2);
Cpstd = sqrt(apstd.^2+bstd.^2);
% Compute product of chromas and locations at which it is zero for use
later
Cpprod = (Cpsample.*Cpstd);
zcidx = find(Cpprod == 0);


% Ensure hue is between 0 and 2pi
% NOTE: MATLAB already defines atan2(0,0) as zero but explicitly set it
% just in case future definitions change
hpstd = atan2(bstd,apstd);
hpstd = hpstd+2*pi*(hpstd < 0);  % rollover ones that come -ve
```

```
hpstd(find( (abs(apstd)+abs(bstd))== 0) ) = 0;
hpsample = atan2(bsample,apsample);
hpsample = hpsample+2*pi*(hpsample < 0);
hpsample(find( (abs(apsample)+abs(bsample))==0) ) = 0;

dL = (Lsample-Lstd);
dC = (Cpsample-Cpstd);
% Computation of hue difference
dhp = (hpsample-hpstd);
dhp = dhp - 2*pi* (dhp > pi );
dhp = dhp + 2*pi* (dhp < (-pi) );
% set chroma difference to zero if the product of chromas is zero
dhp(zcidx ) = 0;

% Note that the defining equations actually need
% signed Hue and chroma differences which is different
% from prior color difference formulae

dH = 2*sqrt(Cpprod).*sin(dhp/2);
%dH2 = 4*Cpprod.*(sin(dhp/2)).^2;

% weighting functions
Lp = (Lsample+Lstd)/2;
Cp = (Cpstd+Cpsample)/2;
% Average Hue Computation
% This is equivalent to that in the paper but simpler programmatically.
% Note average hue is computed in radians and converted to degrees only
% where needed
hp = (hpstd+hpsample)/2;
% Identify positions for which abs hue diff exceeds 180 degrees
hp = hp - ( abs(hpstd-hpsample)  > pi ) *pi;
% rollover ones that come -ve
hp = hp+ (hp < 0) *2*pi;
% Check if one of the chroma values is zero, in which case set
% mean hue to the sum which is equivalent to other value
hp(zcidx) = hpsample(zcidx)+hpstd(zcidx);

Lpm502 = (Lp-50).^2;
Sl = 1 + 0.015*Lpm502./sqrt(20+Lpm502);
Sc = 1+0.045*Cp;
T = 1 - 0.17*cos(hp - pi/6 ) + 0.24*cos(2*hp) + 0.32*cos(3*hp+pi/30)
...
    -0.20*cos(4*hp-63*pi/180);
Sh = 1 + 0.015*Cp.*T;
delthetarad = (30*pi/180)*exp(- ( (180/pi*hp-275)/25).^2);
Rc =  2*sqrt((Cp.^7)./(Cp.^7 + 25^7));
```

```
RT =  - sin(2*delthetarad).*Rc;

klSl = kl*Sl;
kcSc = kc*Sc;
khSh = kh*Sh;

% The CIE 00 color difference
de00 = sqrt( (dL./klSl).^2 + (dC./kcSc).^2 + (dH./khSh).^2 +
RT.*(dC./kcSc).*(dH./khSh) );
return
```

Appendix D: Matlab Algorithm for Analytical Evaluation of Readout Mechanisms

The Matlab algorithm that was developed can be broken into general sections as shown in the flowchart presented in Figure D-1.

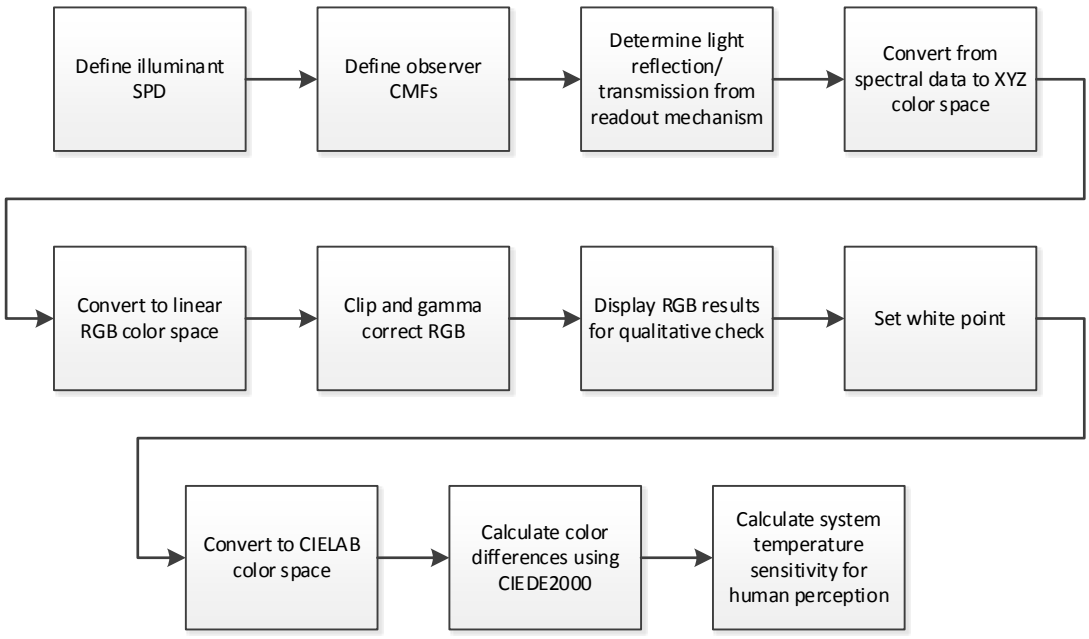

Figure D-1 Flow chart for Matlab algorithm that was developed to evaluate the readout mechanisms

In order to define the illuminant that will be used, the Matlab program is designed to read data from a text file. This first line of the illuminant file should contain the number of lines in the file, while subsequent lines should contain first the wavelength in nm and then the relative power at that wavelength, separated by a tab. An example of the illuminant file format is shown in Figure D-2.

```
441
390 54.6482
391 57.4589
392 60.2695
393 63.0802
394 65.8909
     :
     :
829 60.0253
830 60.3125
```

Figure D-2 Illuminant spectral power data format

Here the illuminant contains 441 lines of data, from 390 nm to 830 nm. The spectral power distribution for the ThorLabs LED light sources used in this work were linearly interpolated from measured spectral data for the light sources which can be found at:

http://www.ThorLabs.com/images/tabimages/High-Power_LED_Spectra_MxxxLx-Scaled.xlsx. Similarly, the spectral power distribution for the D65 daylight illuminant used for the calculation of a reference white and as the illumination in evaluation of the Nomarski DIC readout was linearly interpolated from tabular data which can be found at: http://files.cie.co.at/204.xls.

The observer CMFs are loaded similarly, where the first line is the number of lines of data in the file and subsequent lines contain first the wavelength, then the x, y, and z tristimulus values. An example of the observer file format is shown in Figure D-3.

```
441
390     3.77E-03        4.15E-04        1.85E-02
391     4.53E-03        5.03E-04        2.22E-02
392     5.45E-03        6.08E-04        2.67E-02
393     6.54E-03        7.34E-04        3.21E-02
394     7.84E-03        8.84E-04        3.85E-02
 :          :               :               :
 :          :               :               :
829     1.87E-06        7.47E-07        0.00E+00
830     1.76E-06        7.05E-07        0.00E+00
```

Figure D-3 Color matching function data format

This file contains 441 lines of data, the particular color matching function used for this work is shown in tabular form in Appendix A. The developed evaluation program is designed to evaluate three different readout mechanisms, and the mode of operation can be selected using the "readout_mode" variable. The "low_temp" and "high_temp" variables control the temperature range to be analyzed and the "temp_step" variable determines the step size and resolution of the analysis. The program is designed to be executed in cell mode, with each cell achieving a step in the evaluation sequence. Many intermediate plots are presented, for qualitative in-process checks. The final result of the computation is a relationship between the temperature of a scene and the corresponding change in temperature that will cause a noticeable change in color for the particular IR imaging system.

```
function curve = curve(t,m,n,a1,a2,T,To)
curve=(6*(a2-a1).*(T-
To)*(1+m)^2)/(t*(3*(1+m)^2+(1+m*n)*(m^2+(1/(m*n)))));
end

%% Initialize program, clear memory
clc; close all; clear all;

%% Select program mode
readout_mode=3;
```

```
switch readout_mode
    case 1
        readout_mechanism='Reflectometry'
    case 2
        readout_mechanism='Holography'
    case 3
        readout_mechanism='Nomarski'
    otherwise
        fprintf('\nUnrecognized readout mode\n\n');
        break
end

%% Read in illuminant file(s)
close all
switch readout_mechanism
    case 'Reflectometry'
        number_of_illuminants=2;
    otherwise
        number_of_illuminants=1;
end

for i=1:number_of_illuminants;

    [fname,pname]=uigetfile('*.txt',sprintf('Please Select File for
Illuminant Number %d',i));

    if (fname~=0)
        filename=sprintf('%s%s',pname,fname);
    else
        disp('No file selected.  Program has stopped.');
        return;
    end
    fprintf('File opened \n')
    fid=fopen(filename);

    illuminantlines=fscanf(fid,'%d',1); %Read number of lines

    if i==1;
        illuminant=zeros(illuminantlines,1,number_of_illuminants);
%Vector space for illuminant SPD
        illwavelengths=zeros(illuminantlines,1,number_of_illuminants);
%Vector space for wavelengths
    end

    for j=1:illuminantlines
```

```
        illwavelengths(j,1,i)=fscanf(fid,'%f',1);
        illuminant(j,1,i)=fscanf(fid,'%f',1);
    end

    fprintf('Illuminant completed \n')
    % figure
    % hold on
    %
plot(matchingwavelengths(:,1),illuminant(:,1),'Color','red','LineWidth'
,1);
end

%% Scale illuminants for different power levels in reflectometry
close all

if  strcmp(readout_mechanism,'Reflectometry');
    illuminant_scaled(:,1,1)=illuminant(:,1,1);%*.5;
    illuminant_scaled(:,1,2)=illuminant(:,1,2);%*1.5;

    figure;
    hold on
    plot(illwavelengths(1,1,1):illwavelengths(1,1,1)+illuminantlines-
1,illuminant_scaled(:,1,1),'Color','blue','LineWidth',1);
    plot(illwavelengths(1,1,2):illwavelengths(1,1,2)+illuminantlines-
1,illuminant_scaled(:,1,2),'Color','red','LineWidth',1);
    title('Illuminant SPD')

end
%% Read in matching file
close all
[fname,pname]=uigetfile('*.txt','Please Select Color Matching Function
File'); % Read input mesh; specify text file path name

if (fname~=0)
    filename=sprintf('%s%s',pname,fname);
else
    disp('No file selected.  Program has stopped.');
    return;
end
fprintf('File opened \n')
fid=fopen(filename);

matchingLines=fscanf(fid,'%d',1); %Read number of lines

matching=zeros(3,matchingLines); %Vector space for color matching
functions
```

```
matchingwavelengths=zeros(matchingLines,1); %Vector space for color
matching functions

for j=1:matchingLines
    matchingwavelengths(j,1)=fscanf(fid,'%f',1);
    matching(1,j)=fscanf(fid,'%f',1);
    matching(2,j)=fscanf(fid,'%f',1);
    matching(3,j)=fscanf(fid,'%f',1);
end

fprintf('Color Matching Functions Completed \n')

if (illuminantlines~=matchingLines)
    disp('Illuminant lines do not match color functions.  Program has
stopped.');
    return;
end

%%show color matching functions for xbar ybar zbar

% figure
% hold on
%
plot(matchingwavelengths(:,1),matching(1,:),'Color','red','LineWidth',1
);
%
plot(matchingwavelengths(:,1),matching(2,:),'Color','green','LineWidth'
,1);
%
plot(matchingwavelengths(:,1),matching(3,:),'Color','blue','LineWidth',
1);
% title('Color Matching Functions')

%%  Set material properties and cantilever performance
th=6e-6;
m=1/5;
a2=2.33e-6; %silicon
a1=14.2e-6; %gold
E2=1.9e11; %silicon
E1=7.95e10; %gold
n=E1/E2;
length=45e-6; %length of each cantilever in meters
To=0; %ambient temperature

known_responsivity=1.5e-9; %nm/K
beta=(-known_responsivity/((1/rho(th,m,n,a1,a2,1,0))*...
```

```
     (1-cos(length*rho(th,m,n,a1,a2,1,0))));
fprintf('Material properties set \n')

%% Build intensity Matrix
low_temp=0; %temperature range to analyze
high_temp=400;
temperature_step=.1;

temp_range=high_temp-low_temp;
temperature_steps=(high_temp-low_temp)/temperature_step;

transmissionmatrix=zeros(illuminantlines,temperature_steps);
path_difference=zeros(temperature_steps,1);
additional_arbpath_difference=0;

shear=1e-6; %Nomarski Shear

average_mag=zeros(1,temperature_steps);

fprintf('Building transmission matrix\n');
for i=1:temperature_steps
    if  strcmp(readout_mechanism,'Reflectometry');
        transmissionmatrix(:,i)=1/temperature_steps*i;
    else
        for j=1:illuminantlines

            T=(low_temp+temperature_step*(i-1))*beta;
            rho1=rho(th,m,n,a1,a2,T+To,To);
            theta=length*rho1;

            switch readout_mechanism
                case 'Nomarski'
                    %for Michel-Levy chart
                    % path_difference(i,1)=i*temperature_step;

                    %for Nomarski readout

path_difference(i,1)=530+2*shear*tan(theta)*10^09+additional_arbpath_di
fference;

transmissionmatrix(j,i)=(sin(pi*path_difference(i,1)/illwavelengths(j,1
)))^2;

                case 'Holography'
                    path_difference(i,1)=(1/rho1)*(1-cos(theta))*10^09;
```

```
                    if isnan(path_difference(i,1));
                        path_difference(i,1)=0;
                    end

transmissionmatrix(j,i)=0.5+.5*cos(4*pi/illwavelengths(j,1)*path_differ
ence(i,1)+pi);

                otherwise
                    break
            end
        end
    end
    if rem(i,temperature_steps/20)==0;
        fprintf('%.1f %% complete \n',i/temperature_steps*100);
    end
    average_mag(1,i)=mean(transmissionmatrix(:,i));
end
fprintf('Transmission matrix complete\n');

%% Plot transmission matrix, relative phase of the two components of
each wavelength of light
close all
figure;
hold on;
plot(1:1:temperature_steps,transmissionmatrix(:,:));
plot(1:1:temperature_steps,average_mag(1,:)./max(average_mag(1,:)),'Lin
eWidth',2);
set(gca,'XTick',low_temp:temperature_steps/5:temperature_steps)
set(gca,'XTickLabel',{low_temp,temp_range/5*1,temp_range/5*2,temp_range
/5*3,temp_range/5*4,temp_range/5*5})
title('Transmission Matrix')

%% Plot path difference vs temperature based on readout mechanism
close all
figure;
plot(1:1:temperature_steps,path_difference(:,:));
set(gca,'XTick',low_temp:temperature_steps/5:temperature_steps)
set(gca,'XTickLabel',{low_temp,temp_range/5*1,temp_range/5*2,temp_range
/5*3,temp_range/5*4,temp_range/5*5})
title('Path Differecene vs Temperature')

%% Build spectral color stimulus function (matrix) from transmission
matrix and illuminant
close all
light_matrix=zeros(illuminantlines,temperature_steps);
```

```
switch readout_mechanism
    case 'Reflectometry'

combined_illuminant=illuminant_scaled(:,:,1)+illuminant_scaled(:,:,2);
        for i=1:size(light_matrix,2)
            light_matrix(:,i)=illuminant_scaled(:,:,1).*(1-
transmissionmatrix(:,i))+...
                illuminant_scaled(:,:,2).*transmissionmatrix(:,i);

average_mag(1,i)=sum(light_matrix(:,i),1)./sum(light_matrix(:,i)~=0,1);
        end

    case 'Holography'
        combined_illuminant=illuminant(:,:,1);
        for i=1:size(light_matrix,2)

light_matrix(:,i)=illuminant(:,:,1).*transmissionmatrix(:,i);

average_mag(1,i)=sum(light_matrix(:,i),1)./sum(light_matrix(:,i)~=0,1);
        end

    case 'Nomarski'
        combined_illuminant=illuminant(:,:,1);
        for i=1:size(light_matrix,2)

light_matrix(:,i)=illuminant(:,:,1).*transmissionmatrix(:,i);

average_mag(1,i)=sum(light_matrix(:,i),1)./sum(light_matrix(:,i)~=0,1);
        end

    otherwise
        break
end

figure;
hold on;
plot(1:1:temperature_steps,light_matrix(:,:));
plot(1:1:temperature_steps,average_mag(1,:)./max(average_mag(1,:)),'Lin
eWidth',2);
set(gca,'XTick',low_temp:temperature_steps/5:temperature_steps)
set(gca,'XTickLabel',{low_temp,temp_range/5*1,temp_range/5*2,temp_range
/5*3,temp_range/5*4,temp_range/5*5})
title('Light Matrix')

%% Build and display XYZ
close all
```

```
XYZ=zeros(3,temperature_steps);
%XYZ=matching*light_matrix;
XYZ=(100/(matching(2,:)*combined_illuminant))*matching*light_matrix;

figure;
hold on
plot(1:1:size(XYZ,2),XYZ(1,:),'Color','red','LineWidth',1);
plot(1:1:size(XYZ,2),XYZ(2,:),'Color','green','LineWidth',1);
plot(1:1:size(XYZ,2),XYZ(3,:),'Color','blue','LineWidth',1);
set(gca,'XTick',low_temp:temperature_steps/5:temperature_steps)
set(gca,'XTickLabel',{low_temp,temp_range/5*1,temp_range/5*2,temp_range
/5*3,temp_range/5*4,temp_range/5*5})
title('X (red) Y (green) Z (blue)')

%% Set inverse M matrix for XYZ --> RGB conversion
close all
%XYZ=XYZ./scale;%max(XYZ(2,:));

% M=[2.0413690, -0.5649464, -0.3446944 %XYZ to RGB conversion for Adobe
RGB (1998)
%   -0.9692660,  1.8760108,  0.0415560
%    0.0134474, -0.1183897,  1.0154096];

M_inv=[3.2404542, -1.5371385, -0.4985314 %XYZ to sRGB conversion
  -0.9692660,  1.8760108,  0.0415560
   0.0556434, -0.2040259,  1.0572252];

%% Convert XYZ to RGB
close all
%scale here if needed
RGB=M_inv*(XYZ)/100;

figure;
hold on
plot(1:1:size(RGB,2),RGB(1,:),'Color','red','LineWidth',1);
plot(1:1:size(RGB,2),RGB(2,:),'Color','green','LineWidth',1);
plot(1:1:size(RGB,2),RGB(3,:),'Color','blue','LineWidth',1);
title('Linear RGB channels')
set(gca,'XTick',low_temp:temperature_steps/5:temperature_steps)
set(gca,'XTickLabel',{low_temp,temp_range/5*1,temp_range/5*2,temp_range
/5*3,temp_range/5*4,temp_range/5*5})

RGB_3=zeros(1,size(RGB,2),3);

RGB_3(1,:,1)=RGB(1,:);
RGB_3(1,:,2)=RGB(2,:);
```

```
RGB_3(1,:,3)=RGB(3,:);
gamma_correction=1/2.2;
RGB_3_gamma=imadjust(RGB_3, [], [], gamma_correction);

figure
hold on
plot(1:1:size(RGB_3_gamma,2),RGB_3_gamma(1,:,1),'Color','red','LineWidt
h',1);
plot(1:1:size(RGB_3_gamma,2),RGB_3_gamma(1,:,2),'Color','green','LineWi
dth',1);
plot(1:1:size(RGB_3_gamma,2),RGB_3_gamma(1,:,3),'Color','blue','LineWid
th',1);
title('Gamma corrected RGB channels')
set(gca,'XTick',low_temp:temperature_steps/5:temperature_steps)
set(gca,'XTickLabel',{low_temp,temp_range/5*1,temp_range/5*2,temp_range
/5*3,temp_range/5*4,temp_range/5*5})

%%Manually clip RGB to 0-1, imadjust does this automatically
% for j=1:size(RGB,1)
%     for i=1:size(RGB,2)
%         if RGB(j,i)>1
%             RGB(j,i)=1;
%         elseif RGB(j,i)<0
%             RGB(j,i)=0;
%         end
%     end
% end

%% Build RGB image and gamma correct
close all
image_height=150;%round((maxpathdifference/path_difference_step)/6);
image_width=800;

if size(RGB,2)>image_width;
    image_scale=size(RGB,2)/image_width;
else
    image_scale=1;
end
real_image_scale=round(image_scale);
image=zeros(image_height,floor(size(RGB,2)/real_image_scale),3);

k=1;
for j=1:size(RGB,2);
    if rem(j,real_image_scale)==0;
        image(1,k,1)=RGB(1,j);
        image(1,k,2)=RGB(2,j);
```

```
        image(1,k,3)=RGB(3,j);
        k=k+1;
    end
end

for i=1:image_height;
    image(i,:,1)=image(1,:,1);
    image(i,:,2)=image(1,:,2);
    image(i,:,3)=image(1,:,3);
end

figure; imshow(image);
title('Linear RGB interference colors')

gamma_image=imadjust(image, [], [], gamma_correction);
figure;
imshow(gamma_image)
title('Gamma corrected and clipped RGB interference colors')

%% Calculate white point for given illuminant and observer functions
whiteXYZ=matching*combined_illuminant;
whiteXYZ=whiteXYZ./whiteXYZ(2)*100;

% show illuminant SPD
% figure; plot(illwavelengths(1):illwavelengths(1)+illuminantlines-
1,illuminant)
% title('Illuminant')
% set(gca,'XTick',low_temp:temperature_steps/5:temperature_steps)
%
set(gca,'XTickLabel',{low_temp,temp_range/5*1,temp_range/5*2,temp_range
/5*3,temp_range/5*4,temp_range/5*5})

%% XYZ to Lab Conversion
close all
epsilon=216/24389;
kappa=24389/27;

XYZ3=zeros(1,size(XYZ,2),3);
XYZ3(1,:,1)=XYZ(1,:);
XYZ3(1,:,2)=XYZ(2,:);
XYZ3(1,:,3)=XYZ(3,:);

%ref_XYZ = [whiteXYZ(1); whiteXYZ(2); whiteXYZ(3)];
ref_XYZ = [95.047; 100.000; 108.883]; %D65 white point
%ref_XYZ = [100; 100.000; 100];
```

```
for i=1:3
    XYZ3(:,:,i) = XYZ3(:,:,i) / ref_XYZ(i);
end

index1 = find(XYZ3 > epsilon);
index2 = find(XYZ3 <= epsilon);
XYZ3(index1) = XYZ3(index1).^(1/3);
XYZ3(index2) = (0*kappa+ 7.787 * XYZ3(index2) ) + ( 16 / 116 );

% CIE-L*a*b*
LAB = zeros(size(XYZ3));
LAB(:,:,1) = ( 116 * XYZ3(:,:,2) ) - 16;
LAB(:,:,2) = 500 * ( XYZ3(:,:,1) - XYZ3(:,:,2) );
LAB(:,:,3) = 200 * ( XYZ3(:,:,2) - XYZ3(:,:,3) );

figure;
hold on
plot(1:1:size(LAB,2),LAB(1,:,1),'Color','red','LineWidth',1);
plot(1:1:size(LAB,2),LAB(1,:,2),'Color','green','LineWidth',1);
plot(1:1:size(LAB,2),LAB(1,:,3),'Color','blue','LineWidth',1);
title('Plot of CIELAB components. L* (red), a* (green), and b* (blue)')
set(gca,'XTick',low_temp:temperature_steps/5:temperature_steps)
set(gca,'XTickLabel',{low_temp,temp_range/5*1,temp_range/5*2,temp_range
/5*3,temp_range/5*4,temp_range/5*5})

%% Calculate Delta E 2000 for every data triplet in LAB array
close all
de00_limit=2; % predetermined difference threshold
de00_pathdiff_array=zeros(1,temperature_steps);
% change in temperature, at each temperature, that will result in
% a noticable change in color (the delta T that will result in
% de00=de00_limit)

for k=1:temperature_steps;
    for i=1:3
        Labstd(1,i)=LAB(1,k,i);
    end

    for l=k:temperature_steps;
        for i=1:3
            Labsample(1,i)=LAB(1,l,i);
        end

        if deltaE2000(Labstd,Labsample)>= de00_limit;% || l-k>50;
            break
```

```
        end
    end

    if l==temperature_steps;
       de00_pathdiff_array(1,k)=NaN;
        % NaN; (if the additional path difference is greater than the
        % remaining distance to the end of the calculated path
differences)
    else
        de00_pathdiff_array(1,k)=(l-k)*temperature_step;
    end

    if rem(k,temperature_steps/200)==0;
        fprintf('%.1f %% complete \n',k/temperature_steps*100);
    end
end

figure;
plot(1:1:size(de00_pathdiff_array,2),de00_pathdiff_array(1,:),'Color','
blue','LineWidth',1);
title('Temperature increase that will cause a change in color greater
than de00 threshold')
set(gca,'XTick',low_temp:temperature_steps/5:temperature_steps)
set(gca,'XTickLabel',{low_temp,temp_range/5*1,temp_range/5*2,temp_range
/5*3,temp_range/5*4,temp_range/5*5})

%% Experimental charts
close all
temperature_axis=low_temp:temperature_step:high_temp-temperature_step;
bar_chart_bars=temperature_axis+de00_pathdiff_array(1,:);

figure;
hold on
barh( bar_chart_bars/temperature_step,1, 'b','EdgeColor', 'b')
barh( temperature_axis/temperature_step,1, 'w','EdgeColor', 'w')
title('Temperature increase that will cause a change in color greater
than de00 threshold')
set(gca,'XTick',low_temp:temperature_steps/5:temperature_steps)
set(gca,'XTickLabel',{low_temp,temp_range/5*1,temp_range/5*2,temp_range
/5*3,temp_range/5*4,temp_range/5*5})
set(gca,'YTick',low_temp:temperature_steps/5:temperature_steps)
set(gca,'YTickLabel',{low_temp,temp_range/5*1,temp_range/5*2,temp_range
/5*3,temp_range/5*4,temp_range/5*5})
axis([0,temperature_steps,0,temperature_steps])
%plot(1:1:size(de00_pathdiff_array,2),10*de00_pathdiff_array(1,:)/tempe
rature_step,'Color','blue','LineWidth',1);
```